EVOLUTION OF NANOCATALYST STRUCTURE AND COMPOSITION DURING CHEMICAL VAPOR DEPOSITION SYNTHESIS OF SINGLE-WALLED CARBON NANOTUBES

A Dissertation

by

JOSE LEONARDO GOMEZ BALLESTEROS

Submitted to the Office of Graduate and Professional Studies of
Texas A&M University
in partial fulfillment of the requirements for the degree of

DOCTOR OF PHILOSOPHY

Chair of Committee,	Perla B. Balbuena
Committee Members,	James Holste
	Jodie Lutkenhaus
	Choongho Yu
Head of Department,	Nazmul M. Karim

May 2017

Major Subject: Chemical Engineering

ABSTRACT

Various aspects of the catalytic synthesis of single-walled carbon nanotubes (SWCNTs) on transition metal nanoparticles were studied by combining atomistic simulations: reactive molecular dynamics (RMD), density functional theory (DFT), and *ab initio* molecular dynamics (AIMD), with *in situ* high-resolution environmental transmission electron microscope (ETEM) imaging. SWCNTs are carbon allotropes with applications in many technological fields owing to their exceptional properties that depend on their structural features. Understanding the nucleation and growth of SWCNTs can provide the tools to devise strategies to control their structure from the synthesis, thus allowing further development and implementation of nanotube-based technologies.

The interactions of supported and unsupported carbon-philic and noble transition metal catalytic nanoparticles with adsorbed or dissolved carbon and nanotube seeds were investigated using DFT and AIMD simulations. These studies revealed differences in solubility and nucleation mechanisms on the different particles due to interactions with added C and the support. A cooperative nucleation mechanism was demonstrated using ETEM measurements and DFT, in which different facets of the catalyst with stronger/weaker adhesion facilitate nucleation/lift-off of the seed to form the nanotube. ETEM and RMD of supported Co catalyst during nanotube growth revealed structural changes in the nanoparticle and the coexistence of metal and carbide regions of fluctuating size directly affecting the growth rate and catalyst structure.

ACKNOWLEDGEMENTS

First and foremost I would like to thank my advisor, Dr. Perla Balbuena, for the opportunity to work as a part of her research group. Her constant guidance, support, mentorship, and encouragement have led me to become the scientist and researcher that I am today. I am thankful for the opportunity to gain experience from conferences, collaboration with experimental research labs, and teaching. I have gained invaluable experience as a result of her confidence in my abilities and my growth as a researcher. I also thank my committee members for taking the time to meet and discuss my research. I would like to thank my research collaborators for their contributions to the work presented in this dissertation.

I would like to thank the members of the Balbuena Research Group, both past and present, for their encouragement and support. Many of them have now become close friends and trusted colleagues. Finally, I would like to thank my friends and family for their never ending support, encouragement, and love. None of this would have been possible without them.

CONTRIBUTORS AND FUNDING SOURCES

Contributors

This work was supervised by a dissertation committee consisting of Prof. Perla Balbuena, Prof. Jodie Lutkenhaus, and Prof. James Holste of the Chemical Engineering Department, and Prof. Choongho Yu of the Mechanical Engineering Department.

ETEM atomic resolution images of SWCNT growth and analyses presented in Chapters V (2014), VI (2015), and VII (2017) were provided by our collaborators, Dr. Renu Sharma and her team, Matthieu Picher, Pin Ann Lin, and Bharath Natarajan from the Center for Nanoscale Science and Technology at the National Institute of Standards and Technology (NIST). From the Balbuena Research Group, Dr. Juan Carlos Burgos provided preliminary results of RMD simulations for Chapter VI and Chapter V, and Kie Hankins and Ivan Gomez processed data for Chapter IV. All other work conducted for this dissertation was completed by the student independently.

Funding Sources

The computational work was supported by the US Department of Energy, Basic Energy Sciences, under grant DE-FG02-06ER15836. Computational resources from TAMU Supercomputer Facility, Brazos Cluster at Texas A&M University, Texas Advanced Computing Center (TACC), and from the National Energy Research Scientific Computing Center, which is supported by the Office of Science of the U.S. Department of Energy under Contract No. DE-AC03-76SF00098, are gratefully acknowledged.

TABLE OF CONTENTS

Page

LIST OF FIGURES

Page

LIST OF TABLES

Page

CHAPTER I

INTRODUCTION AND LITERATURE REVIEW

Carbon nanotubes are among the first materials that attracted a significant active interest in the nascent field of nanotechnology. Their discovery is attributed to Iijima in 1991,[1] and since then they have been the focus of intensive research due to their remarkable properties and the potential to be used in technological applications. Carbon nanotubes are being implemented in a vast number of fields[2] including renewable energy[3] and energy storage,[4] high-performance electronics technology,[5] flexible electronics,[6] nanocomposite materials,[7] environmental science,[8] biotechnology,[9] and nanomedicine.[10] New and ingenious applications continue to be explored in order to exploit their outstanding properties: mechanical strength, great surface area, high thermal conductivity, and tunable optical and electrical properties.[11] Suitability of carbon nanotubes for particular applications sometimes requires specific structural features of the nanotubes such as diameter and chirality to be uniform as well as low concentration of defects and alignment of nanotube arrays.[2] Based on their structure, carbon nanotubes can be classified according to the number of concentric tubes into single- and multi-walled and according to their helicity into zig-zag, armchair and chiral.

The structure of a single-walled carbon nanotube (SWCNT) is typically described as that of a graphene sheet rolled up into a seamless tube. Graphene, having a 2-D honeycomb crystal lattice structure of sp^2 carbon, is a semimetal with its valence and conduction bands touching each other at the Dirac points. Additional quantum confinement is created when the graphene structure is rolled up into a nanotube, and therefore a SWCNT can exhibit metallic or semiconducting behavior depending on its helicity and diameter.[12] The chirality or helicity of a SWCNT can be uniquely defined by a chiral vector $\mathbf{C}_{n,m}$ = n**a** + m**b**, where **a** and **b** are the unit vectors of the honeycomb lattice, and n and m are the chiral indices. Depending on the chiral indices (n,m) or chiral angle θ_c (eq 1.1) formed between the unit vectors, different types of nanotubes such as zig-zag with (n,0) indices and θ_c= 0°, arm-chair with (n,n) indices and θ_c= 30°, and chiral with chiral angles between 0° and 30° can be obtained with diameter given by eq 1.2, where a_{cc} is the nearest-neighbor carbon distance.

$$\theta = \tan^{-1}\left(\frac{\sqrt{3}m}{m+2n}\right) \tag{1.1}$$

$$d = \left(\frac{\sqrt{3}a_{acc}}{\pi}\right)\left(n^2 + nm + m^2\right)^{\frac{1}{2}} \tag{1.2}$$

The electronic and optical properties of a SWCNT are dependent on its structure, as diameter and chiral indices affect the electronic structure and combinations of these parameters produce tubes with band gaps ranging from zero to a few eV.[13] In terms of electrical conductivity, nanotubes with indices that follow the rule n – m = 3·x (where x is a nonnegative integer) exhibit metallic behavior, or semiconducting behavior otherwise, based on the analysis of the electronic structure.[14] Accordingly, as-synthesized SWCNTs are expected to be typically a mixture of ~66% semiconducting and ~33% metallic tubes,[5] thus posing a challenge for their use in some applications that require nanotubes with uniform properties and structure. Other structural factors such as density of defects, vertical or horizontal alignment, and overall quality of nanotubes affect how effectively their properties can be exploited and their use in specific applications.[15]

Further development of technologies, which can be enabled and benefited by incorporating nanotubes, requires the formulation and implementation of strategies that allow producing SWCNTs with properties and characteristics as desired. One promising approach to achieve this goal is *via* templated synthesis, which in the context of catalytic synthesis of SWCNTs, seeks to use the structure of the catalyst as a template to guide the structure of the resulting nanotube.[16] Current research efforts aim to attain a better understanding of the nucleation and growth mechanisms, which in turn can provide fundamental knowledge to devise strategies leading to a controlled SWCNT synthesis.

The present work seeks to contribute to the understanding of the nucleation and growth mechanisms of SWCNTs *via* catalyzed synthesis and the nature of the interactions between the nascent nanotube structure and the catalyst. The challenges associated with this endeavor are manifold, with a considerably wide parameter space of process variables, and the resolution required to investigate phenomena occurring at short-time and small-size scales intrinsic of the nanotube growth process. Therefore, the approach presented here is focused on specific stages and conditions of the synthesis process using molecular modeling at different levels of theory. Density functional theory (DFT) and reactive molecular dynamics simulations (RMD) are combined with *in-situ* experimental observation from high-resolution environmental transmission electron microscopy

(HRTEM) in a collaborative effort with the National Institute of Standards and Technology (NIST) to better understand SWCNT growth from its early stages.

1.1 Selective Synthesis of SWCNTs

One of the first techniques used to produce carbon nanotubes was arc discharge evaporation, where a direct current (DC) arc voltage is established across two graphite electrodes with carbon vaporizing from the positive electrode in an inert atmosphere to produce multi-walled carbon nanotubes deposited on the negative electrode.[1] Single-walled carbon nanotubes can also be obtained when the anode contains metals such as Ni, Co or Y.[17] Carbon nanotubes were also initially synthesized by laser ablation, a method in which carbon and metal atoms are vaporized using a laser source to produce self-assembled carbon nanotubes deposited on metal nanoparticles.[18] Variations of these strategies generally included a source of carbon evaporated from a source through heating by laser pulses, electric arcs or radiative fluxes, which made them high energy-consuming processes.

Among the most successful methods, due to its scalability, higher degree of control and lower energy requirements than methods previously used is catalytic chemical vapor deposition (CVD). The process consists of the catalytic conversion of a carbon precursor gas into carbon nanotubes on the surface of catalyst nanoparticles. The most common metals used as catalysts in the CVD process are Ni, Fe, and Co, however nanotube growth on noble metals (Cu, Ag, and Au), late transition metals (Pd, Pt, and Ru) and early transition metals (Mn, Cr, and Mo) has also been reported.[15] Typical CVD processes for the growth of carbon nanotubes require temperatures ranging from 600°C to 1000°C and low to moderate pressures (1-10 bar).[19-20] Catalyst nanoparticles used in CVD can be either floating or supported, both of which offer different possibilities to influence the structure of the synthesized nanotube, for example, by changing the synthesis conditions[21] or the interactions between the nanotube and the support.[22]

Synthesis strategies such as the CoMoCAT process proposed by Resasco *et al*.[23-24] initially achieved a narrow distribution of nanotubes with 57% semiconducting SWCNTs from a product containing a mostly (6, 5) and (7, 5) nanotubes[23] and 55% of pure (6, 5) nanotubes after modifying the gaseous feed composition and support morphology.[24] This degree of control of the SWCNT structure is attributed to two key aspects of the CoMoCAT process: the presence of a second metal in the catalytic particle (Mo + Co), and the effect of the support, both of which exert influence on the particle morphology and stability.

The selective growth of (6, 5) nanotubes was also achieved by Fouquet *et al*. from monometallic Co supported on an oxidized Si wafer. *In-situ* x-ray photoelectron spectroscopy of this system revealed that the interfacial Co-Si interactions play a role in both stabilizing the nanoparticle/nanotube diameter and producing a narrow diameter distribution.[25] Preferential growth of semiconducting SWCNT (~90%) was later reported on supported monometallic Co nanoparticles, which possessed a well-defined crystal structure. High-resolution transmission electron microscope imaging analysis of the supported nanoparticles indicated an epitaxial relationship between the nanoparticle and the MgO support, which conferred structural uniformity to the Co nanoparticles and the ability to selectively grow nanotubes with (6, 5) chirality (~53%). Interestingly, decreasing the growth temperature shifted the selectivity toward nanotubes with (7, 6) and (9, 4) chiral indices with slightly larger diameters.[26] In addition, a number of experimental strategies to achieve high selectivity toward other chiralities has been explored and reported, where connections can be established between a crystalline particle and narrow distributions of nanotube chirality, for example, high content of (9, 8) SWCNTs grown on Co nanoparticles supported on mesoporous silica, and bimetallic WCo catalysts to selectively produce (12, 6),[27] (16, 0)[28] or (14, 4).[29]

Significant progress has been made to obtain carbon nanotubes with desired structures, high yield, purity, and alignment using CVD.[15-16] Many experimental efforts to achieve these goals have been focused on seeking combinations of synthesis parameters such as choice of catalyst and support, type of carbon precursor gas and additives, temperature, and pressure.[15] In retrospect, the state of the catalyst, its structure and composition, and the changes that it undergoes during the catalytic process under the synthesis conditions seem to have a deterministic role on accomplishing control of the SWCNT structure. Therefore, significant efforts have been devoted to elucidate and understand the transformations of the catalyst particle during the nucleation and growth stages of SWCNTs. A summary of the current knowledge on these mechanisms and an overview of the present work are discussed next.

1.2 Nucleation and Growth Mechanisms of SWCNTs

The synthesis of carbon nanotubes according to the CVD process begins with the decomposition of the carbon precursor gas on the surface of the catalyst, which consists of a transition metal particle previously synthesized and typically deposited on a metal oxide support[30] or formed *in situ* during the nanotube synthesis process as a floating catalyst.[31] The importance of the structural features of the catalyst particle stems from its role as nucleation site and regulator of the tube diameter.[25] Early TEM studies of postsynthezised SWCNTs attached to Mo and Ni/Co catalysts provided information leading to the formulation of the yarmulke hypothesis, which proposes that the carbon atoms, resulting from the decomposition of the precursor gas, assemble into a graphene cap on the catalyst surface while lowering the surface energy of the metal nanoparticle.[30] In more general terms, this stage is known as nucleation and it is followed by partial detachment of the nanotube cap from the catalyst, while carbon atoms at the rim remain attached to it, and elongation or growth of the nanotube.

Two of the main factors affecting the structure of the nanotube cap as it forms are: 1) the relative stability of the cap on the catalyst surface, and 2) the mechanism for the continued addition of carbon atoms diffusing on the surface and from the carbon interior to form hexagonal rings at the reactive edges of the existing cap.[32-35] It has been suggested that such factors and the nanotube cap topology can be influenced during nucleation by controlling epitaxial relationships between the growing nanotube cap and the catalyst surface, and therefore control of the overall nanotube structure can be achieved as long as the base structure of the nanotube cap does not change during elongation.[36-38] Changes on the nanotube structure occurring after the cap is formed have been reported from molecular simulations and seem to be influenced by the state of the catalyst particle and its stability.[39]

The vapor-liquid-solid (VLS) model is one of the most generally accepted mechanisms to describe the growth of SWCNTs by CVD. It was first proposed by Wagner and Ellis for the growth of Si whiskers[40] and in the context of carbon nanostructures Baker *et al*. used it to describe the growth of carbon filaments.[41-42] According to the original model, atoms or molecules in the vapor phase deposit on the catalytic particle, which behaves as a liquid droplet, and later precipitate after supersaturation of the particle to form a solid filament. The main ideas proposed by this model are a) that the particle is liquid and b) that atomic diffusion of the reacting species occurs inside the particle. Baker *et al*. estimated activation energies that correspond to diffusion barriers of carbon through the metals studied, thus demonstrating the second hypothesis of VLS and indicating that diffusion inside the particle is the rate determining step of carbon filament growth.[42] Nevertheless, agreement was found for diffusion of carbon in a solid nanoparticle, which contradicts the first hypothesis of VLS. TEM observations of a variety of nickel nanoparticle morphologies after nanotube growth initially supported the idea of a liquid particle,[43] however it was later demonstrated *via in-situ* TEM observations that despite deformation, Ni and Fe nanoparticles maintained a crystalline structure during growth.[44] Further evidence supporting hypotheses about the catalyst being a liquid particle,[45-47] a solid particle,[26-27, 48-49] and a fluctuating-solid particle, which exhibits changes in shape based on a creep mechanism induced by capillary forces exerted by the nanotube,[50-51] has been presented. This seems to indicate that under favorable conditions, which may vary from one catalytic system to another, either type of particle can sustain SWCNT growth. Transitions between a solid and liquid state of the catalyst are affected by particle size, carbon content, and interactions with the support.

For small transition metal nanoparticles with diameters under 10 nm, a depression of the melting point is observed due to higher surface-to-volume ratio and the larger contribution of the surface atoms to the total energy of the system.[52] SEM analyses of Fe and Co nanoparticles showed differences in the reduction of the melting point of particles exposed to different atmospheres from 1535°C and 1495°C in the bulk phase to 900°C and 650°C in Ar atmosphere and 650°C and 600°C in CH_4 atmosphere, for Fe and Co respectively. This observation indicates the formation of a eutectic compound in a methane atmosphere, which occurs at a lower temperature than the eutectic point of the bulk material.[53] In addition to affecting the solid-liquid transition, the dissolution of carbon into the particle structure can further affect the nanoparticle structure and interaction with the nanotube.[54-55]

Solubility in nanoparticles is different than solubility in bulk systems, with many nanosized systems showing a significant increase in solubility as size decreases.[56-57] Theoretical studies of carbon solubility in metals, which are known to dissolve carbon in the bulk phase, such as Fe and Ni have predicted a significant increase in solubility compared to that of the bulk phase at the melting temperature.[19] Even metals with a lack of carbon solubility in the bulk phase, such as Au, have shown the ability to dissolve carbon for particles at the nanometric scale.[58-59] The dissolution of carbon in transition metal nanoparticles may result in the formation of stable and metastable carbides. However, the existence, stability and role of a carbide phase on the growth of SWCNTs remain a subject of debate. Formation of carbides in nanoparticles at SWCNT growth conditions has been found to be favorable[46, 50] and unfavorable[44, 60-61]. In addition, distinguishing between metal and carbide structures can be challenging in some cases due to similarities of lattice constant and distortion of the structures due to size effects.[62] Evidence and arguments have been presented to demonstrate the inactivity of transition metal carbide nanoparticles for SWCNT growth, based on their stability,[63] higher bulk diffusion barriers[15, 64] and weaker interaction with carbon on the surface[65-66]. Conversely, successful nanotube growth on carbide nanoparticles has been reported,[50, 67-68] thus indicating that nanotube growth may occur on both metal and metal-carbide nanoparticles, possibly at different rates and mechanisms.[69]

Overall, the nanoparticle structural features and catalytic activity are susceptible to change during nucleation and growth due to an interplay of both internal and external factors. Interactions of transition metal catalytic surfaces with the nucleating carbon nanostructures seem to have a determining role in the type and quality of structure formed and the continuity of the growth process. For example, transition metal catalysts that bind the nanotube more strongly such as Fe, Co and Ni exhibit a better nanotube growth performance than Pd, Cu and Au.[70] Investigations of the interactions of chiral nanotube caps in contact with Ni(111) flat surfaces revealed small differences depending on lattice match.[37] Structures other than nanotubes such as C flakes and flat nanotubes caps are expected to form when the interactions with the catalyst are weak, while stronger interactions promote the formation of pentagons and the curvature needed to form a nanotube.[71] Furthermore, the morphology and activity of supported nanoparticles in a variety of catalytic systems have been found to be influenced by the nature metal/support interactions.[72] Despite the lack of understanding of the role that such interactions can play in SWCNTs synthesis, experimental and theoretical evidence seems to indicate the possibility of using the catalyst-support interactions to influence the structure of the nanotube.[24, 38, 55]

Efforts to understand the complex dynamic interactions between the growing nanotube structure, the catalyst, and the support during nanotube nucleation and growth have greatly benefited from imaging and spectroscopy as well as molecular simulation techniques.[62, 73-74] The purpose of this work is to advance the understanding of SWCNTs nucleation and growth mechanisms using DFT and RMD simulations combined with HRTEM analyses, while providing clues about key factors where further research should be focused. The outcome of this investigation will contribute to building a clearer picture of the molecular phenomena occurring during the CVD synthesis of SWCNTs and provide sufficient knowledge to aid in devising selective growth strategies.

1.3 Outline and Summary of Research

Understanding and defining the role of the catalyst structural and electronic features in the CVD synthesis of single-walled carbon nanotubes is a critical step to achieve controlled growth. The approach taken in this work to investigate the nucleation and growth of SWCNTs consists of DFT and AIMD simulations to study interactions between carbon, the catalytic nanoparticle, and the support, and a combination of RMD simulations and ETEM measurements to determine the evolution of the interactions and structure of the nanoparticle and the nanotube.

In Chapter III and Chapter IV, carbon adsorption and dissolution in the catalyst and the adhesion of model nanotube seeds on metal clusters were investigated. The early stages of the synthesis process were studied using two types of catalyst nanoparticles: a carbon-philic transition metal, namely Ni in Chapter III and Rh, a noble metal in Chapter IV. In Chapter III, the energy of interaction between dissolved carbon and Ni indicates an energetically favorable dissolution process. The interactions of the nanoparticle with model nanotube caps were characterized by an electron density transfer between the particle and the tube, and revealed differences in the interactions between metal and carburized nanoparticles in contact with the nanotube. In Chapter IV, the dissolution of carbon on Rh was found to be limited and affected by particle size and the presence of an MgO support. The effects of two different surface facet terminations of the support, namely the (100) Mg- and O-terminated surface and the (111) OH-terminated surface, as well as a graphene seed representing the nascent nanotube on the catalyst particle and their interactions are discussed.

Chapter V describes the nucleation of a SWCNT on a Co nanoparticle supported on MgO. ETEM images indicated the presence of stable surface facets in the catalyst particle. The nucleating nanotube was observed to adhere more closely to the Co-terminated (020) facet and detach from the Co- and C- terminated (210) facet. DFT calculations confirmed differences in the energy of adhesion of the nascent nanotube on the two different facets. It was concluded that the presence of surfaces with different terminations and local composition aids in the process of nucleation of the carbon structure and lift-off that allows elongation of the nanotube.

In Chapter VI and VII, the nucleation and growth of SWCNTs on Co were investigated by combining RMD simulations and ETEM measurements. Chapter VI discusses the evolution of the catalyst structure and composition during carbon dissolution and nucleation. These early stages are characterized by fluctuations of the catalytic nanoparticle shape and the establishment of a carbon gradient observed in both simulations and experiments. Chapter VII focuses on the growth stage, when the nanotube cap is fully formed, followed by lift-off and nanotube elongation. ETEM images revealed the presence of coexisting metal and carbide regions in the nanoparticle that fluctuate during SWCNT growth. Similar fluctuations in the C concentration profile of the nanoparticle were identified from RMD simulations and a correlation between them and the nanotube growth rate was determined. The contribution to the overall growth rate from surface diffusion was found to be constant, while the rate due to C bulk diffusion from the nanoparticle interior exhibited an oscillatory behavior that was attributed to fluctuations in the size of metal and carbide regions in the nanoparticle. Finally, Chapter VIII summarizes the findings presented and discussed in previous chapters, while providing recommendations and research directions for the continuation of this work.

CHAPTER II

METHODOLOGY

A brief overview of the computational methods used in this work, DFT, RMD and AIMD, is presented in the following subsections.

2.1 Density Functional Theory

DFT is a computational quantum mechanical method that serves as an approximation to solve the Schrödinger equation[75] and determine the energy levels of quantum mechanical systems.

$$i\hbar \frac{\partial}{\partial t} \psi = \hat{H} \psi \tag{2.1}$$

$$\hat{H} \psi = E \psi \tag{2.2}$$

Eq 2.1 corresponds to the time-dependent form of the Schrödinger equation and eq 2.2 corresponds to the time-independent form. The Hamiltonian operator Ĥ is an energy operator and the wave function Ψ is a function that contains information about the quantum state of system. When the Hamiltonian operator is applied to the wave function, it yields the energy of the system multiplied by the wave function. Therefore, the time independent Schrödinger Equation (eq 2.1) is an example of an eigenvalue equation. The Hamiltonian operator for a system with K nuclei and N atoms is described as:

$$\begin{aligned} H = & \sum_{i=1}^{N} \frac{p_i^2}{2m} + \sum_{n=1}^{K} \frac{P_n^2}{2M_n} \\ & + \frac{1}{4\pi\varepsilon_o} \frac{1}{2} \sum_{i,j=1,i\neq j}^{N} \frac{e^2}{\left|r_i - R_n\right|} - \frac{1}{4\pi\varepsilon_o} \sum_{n=1}^{K} \sum_{i=1}^{N} \frac{Z_n e^2}{\left|r_i - R_n\right|} + \frac{1}{4\pi\varepsilon_o} \frac{1}{2} \sum_{n,n'=1,n\neq n'}^{N} \frac{Z_n Z_{n'} e^2}{\left|r_i - R_n\right|} \end{aligned} \tag{2.3}$$

The kinetic energy of electrons and nuclei are described by the first and second terms, respectively in eq 2.3. The electron-electron, electron-nuclei, and nuclei-nuclei coulombic interactions are represented by the third, fourth, and fifth terms, respectively. According to the Born-Oppenheimer approximation,[76] the Schrödinger equation can be simplified by neglecting the kinetics of the nuclei, considering that the nuclei are considerably heavier and slower than the electrons. After applying this approximation, the Schrödinger equation becomes:

$$H = \sum_{i=1}^{N} \frac{p_i^2}{2m} + \sum_{i,j=1,i\neq j}^{N} \frac{e^2}{\left|r_i - R_n\right|} - \frac{1}{4\pi\varepsilon_o} \sum_{n=1}^{K} \sum_{i=1}^{N} \frac{Z_n e^2}{\left|r_i - R_n\right|} \tag{2.4}$$

The many-body problem represented by eq 2.4 still requires a significant numerical computational effort. Further simplification is provided by density functional theory, which focuses on calculation of the electron density. The basis of DFT was proposed by Hohenberg, Kohn, and Sham,[77] and was built around the idea that the ground-state energy of the system is a unique functional of the electron density. Although the exact form of the functional is unknown (more specifically, the V_{xc} term in eq 2.5), it must fulfill the condition that the electron density minimizes the energy of the overall functional. According to the DFT approach Schrödinger equation can be expressed as:

$$\left[-\frac{\hbar}{2m} \nabla^2 + V(r) + V_H(r) + V_{XC}(r) \right] \psi_i(r) = \varepsilon_i \psi_i(r) \tag{2.5}$$

The kinetic energy of the electron and its interaction with the nuclei are represented by the first and second term, respectively in eq 2.5. The third term is the Hartree potential,[78] which corresponds to the electron-electron coulombic repulsion, and it is given by eq 2.6.

$$V_H = e^2 \int_0^R \frac{n(r')}{|r - r'|} d^3 r' \tag{2.6}$$

The fourth term in eq 2.5 representing the correction due to self-contribution interactions and the exchange and correlation effects is defined in eq 2.7.

$$V_{XC} = \frac{\delta E_{XC}(r)}{\delta n(r)} \tag{2.7}$$

The Perdew-Burke-Ernzerhof functional (PBE)[79] based on the generalized gradient approximation (GGA)[80] as implemented in the VASP software was used in all the systems simulated in this work. The use of a “frozen core” approximation and the projected augmented wave method (PAW)[81] are appropriate to describe the systems due to their periodicity. A detailed description of the parameters used for each simulation is presented in the computational methods section of each chapter. The real wave function of the system can be approximated as using a linear combination. For periodic systems, such as those considered in this work, wave functions that can account for the periodicity of the simulation cell are required. Bloch plane waves[82] were used to describe those systems as shown in eq 2.8.

$$\phi_k(r) = e^{ik.r} u_k(r) \tag{2.8}$$

2.2 Reactive Molecular Dynamics Simulations

The evolution of the atomic positions of the models studied, including the effect of time and reaction conditions, is described using reactive molecular dynamics simulations (RMD). In general, classical molecular dynamics simulations describe the time evolution of a system in terms of classical Newtonian mechanics. The energy expression for according to MD is given by:

$$\sum_{i=1,i\neq j}^{N}\sum\nolimits_{j=1}^{1}E_{ijVDW}+\sum_{i=1,i\neq j}^{N}\sum\nolimits_{j=1}^{1}\frac{q_iq_j}{r_{ij}^{2}}\sum E_{ij}+\sum E_{ijk}+\sum E_{ijkl}+\sum_{i=1}^{N}\frac{M_iV_i}{2} \tag{2.9}$$

Each term of eq 2.9, in order of appearance, represents: Van der Waals interactions, Coulombic interactions, energy of interaction due to bonds between two atoms, energy due to angular interactions between three atoms, energy due to torsion interactions between four atoms, and finally the kinetic energy, which reflects the temperature of the system. The set of functions used to describe each type of interaction is known as a force field. Force fields can be constructed based on experimental information or quantum mechanics calculations. A force field that allows formation and breaking of bonds is known as a "reactive force field" and is the basis of RMD simulations. Force fields dictate how each particle (atom or molecule) represented in the model interacts with one another *via* the calculation of the force between them at each step of the simulation. The force on particle (i) due to interactions with each particle (j) is described by eq 2.10:

$$F_i=\sum_{j=1,\,j\neq i}^{N}\frac{\partial E_{ij}}{dr_{ij}} \tag{2.10}$$

The algorithm used to model the dynamics in our simulations was the predictor-corrector algorithm (PC).[83] According to this methodology, the positions r_i, velocities v_i and accelerations ($a_i = F_i/M_i$) at a given time t are used to predict the same variables at a time t + Δt using a series expansion. At each step, a new force and acceleration between atoms are calculated, and the difference between the previous and current step is used as a proportionality factor to correct the new variables describing the system.

The simulations in this work were conducted at constant temperature. Scaling of the velocities is necessary after each step to maintain constant temperature[84]. The temperature at each step is calculated according to eq 2.11 and the scaling is shown in eq 2.12.

$$T_{ins} = \frac{\sum_{i=1}^{N} M_i V_i}{3Nk_B} \tag{2.11}$$

$$V_{i-corrected} = V_i \sqrt{\frac{T}{T_{ins}}} \tag{2.12}$$

The simulation temperature is controlled using a thermostat algorithm. Typical thermostats used in MD simulations include Berendsen,[85] Nosé-Hoover,[86] and Langevin[87]. In this work, Langevin dynamics was used to control the simulation temperature by introducing corrections to the force that are random and temperature-dependent, and corrections that consider frictional forces. Eq 2.13 shows the expression for corrected forces according to the Langevin thermostat.

$$F_{i-corrected} = F_i + \gamma M_i V + \sqrt{2\gamma \kappa_B T M_i} n_{random} \tag{2.13}$$

The nucleation and growth of single-walled carbon nanotubes in a CVD process is simulated using RMD simulations as implemented in the SIMCAT code developed at Prof. Balbuena's research group at Texas A&M University.[32] This code allows the simulation of SWCNT growth on Ni, Co or Cu particles deposited on a model support. A typical RMD simulation to model SWCNT growth consists of a periodic orthorhombic simulation cell of appropriate size containing a metallic nanoparticle deposited on a model support represented by a fixed graphene layer. Periodicity in the Z direction is eliminated by placing a hard wall that prevents the interactions of the growing nanotube with the support in the contiguous cell. The carbon precursor gas corresponds to monoatomic carbon atoms (representing gases such as CO or CH_4) randomly added to the box to maintain a constant gas density, as specified at the beginning of the simulation. Once a gas particle comes in contact with the catalyst nanoparticle, it is said that the particle has been "catalyzed". The addition of carbon to the nanoparticle for a period of time and the C-C interactions dictated by a reactive force field allow the formation of carbon chains and hexagons that create the nanotube cap and its elongation to form the nanotube.

The force field used to describe atomic interactions in SIMCAT consists of a combination of equations to describe each type of atomic interactions. The metal-metal interactions in the catalyst particle are described by the Sutton-Chen potential,[88] according to eqs 2.14 and 2.15.

$$E_i = \left[\frac{1}{2} \sum_{j \neq i} \left(\frac{a}{r_{ij}} \right)^n - c\sqrt{\rho_i} \right] \tag{2.14}$$

$$\rho_i = \sum_{j \neq i} \left(\frac{a}{r_{ij}} \right)^m \tag{2.15}$$

The parameter ρ calculated according to eq 2.15 describes the local density around each metal atom and determines how it interacts with other metal atoms, according to eq 2.14. The metal-carbon and metal-support interactions are dictated by the force field developed by Balbuena *et al*[89] based on the Tersoff-Brenner potential[90]. The energy of interaction in these cases is described according to eq 2.16 with contributions due to repulsion from eq 2.17 and attraction from eq 2.18.

$$E_{ij} = \alpha_{ij} V^R(r_{ij}) - \alpha_{ij}^{1.1} V^A(r_{ij}) \tag{2.16}$$

$$V_{ij}^R = f(r_{ij}) \frac{D_e}{S-1} e^{\left\{-\beta\sqrt{2S}(r_{ij}-R_e\right\}} \tag{2.17}$$

$$V_{ij}^A = f(r_{ij}) \frac{D_e}{S-1} e^{\left\{-\beta\sqrt{2/S}(r_{ij}-R_e)\right\}} \tag{2.18}$$

The pre-exponential factor in eqs 2.17 and 2.18 is a weighting factor that describes the distance dependence of the attractive and repulsive interactions. The α_{ij} parameter in eq 2.16 determines the interactions between the metal atoms in the particle and the support. The carbon-carbon and carbon –support interactions are described by eq 2.16 as well with contributions from repulsion between atoms given by eq 2.19 and attraction by eq 2.20.

$$V_{ij}^R = f(r_{ij}) \left(1 + \frac{Q}{r_{ij}} \right) A e^{\{-ar\}} \tag{2.19}$$

$$V_{ij}^A = b_{ij} \left(f(r_{ij}) \sum_{n=1}^{3} B_n e^{-\beta_n r_{ij}} \right) \tag{2.20}$$

Repulsion and attraction for carbon-carbon interactions are modeled using equations that differ from those presented for the metal-carbon interactions to account for the weakened C-C bond strength due to interactions of carbon with metal atoms. Some of the advantages of using RMD are that it allows the consideration of time evolution of the system, and incorporation of the reactions conditions for relatively large numbers of atoms at the expense of not considering the electronic interactions explicitly. For a DFT level description of the dynamic behavior of the system, smaller systems were simulated using *ab initio* molecular dynamics simulations (AIMD).

2.3 *Ab Initio* Molecular Dynamics Simulations

AIMD simulations combine the rigorous treatment to determine the energy states of the system using DFT with classical equations to allow predictions of dynamic trajectory of the particles. Among the various approaches to implement this combination, the Born-Oppenheimer molecular dynamics[91-92] approach is utilized here. According to this methodology, the potential energy of the system calculated at each time step corresponds to the Born-Oppenheimer potential energy, which described the quantum state of atoms whose positions are updated using a classical molecular dynamics scheme.

CHAPTER III

STRUCTURE AND DYNAMICS OF METALLIC AND CARBURIZED CATALYTIC NI NANOPARTICLES: EFFECTS ON GROWTH OF SINGLE-WALLED CARBON NANOTUBES[*]

3.1 Summary

Understanding the evolution of the catalyst structure and interactions with the nascent nanotube at typical chemical vapor deposition (CVD) conditions for the synthesis of single-walled carbon nanotubes is an essential step to discover a way to guide growth toward desired chiralities. We use density functional theory (DFT) and *ab initio* molecular dynamics (AIMD) simulations on model metallic and carburized Ni clusters to explore changes in the fundamental features of the nanocatalyst: geometric and electronic structure, dynamics and stability of the carburized nanocatalyst, and interactions with nascent nanotube caps at two different temperatures (750 and 1000 K) and different carbon composition ratios. This allows us to gain insight about the evolution of these aspects during the pre-growth and growth stages of CVD synthesis of single-walled carbon nanotubes and their implications for reactivity and control of the nanotube structure.

---

[*] Reprinted with permission from "Structure and Dynamics of Metallic and Carburized Catalytic Ni Nanoparticles: Effects on Growth of Single-Walled Carbon Nanotubes" by J. L. Gomez-Ballesteros, and P. B. Balbuena, 2015. *Phys. Chem. Chem. Phys.* 17, 15056-15064, Copyright 2015 by The Royal Society of Chemistry.

3.2 Introduction

A significant and sustained interest in finding ways to synthesize nanomaterials has emerged a couple of decades ago. Motivation for this was nourished by predictions of materials with extraordinary properties conferred by their nanometric dimensions. Among the ample variety of nano-sized novel materials that continue to cause fascination, carbon nanotubes maintain interest as new exciting applications emerge, and efforts to produce them in a selective and efficient manner continue to increase[15]. Potential uses of single-walled carbon nanotubes (SWCNTs) range from nanoelectronic devices such as electron field transistors[93], to biomedical[94], separations[95], electrochemistry[96] and other innovative energy-related applications[2]. The attractiveness of SWCNTs for these and other emerging applications is derived from their outstanding properties including excellent thermal conductivity[97], electron mobility[98], electron transfer in electrodes[99], optical properties[100] and mechanical stability[101].

A number of synthesis techniques have been developed to fabricate SWCNTs at low cost and large-scale[102]. However, the lack of control of the nanotube structure (and associated chirality) remains to be one of the main obstacles for the selective synthesis of SWCNTs. Structural features such as diameter, length, defect density, and chiral angle are fundamental to determine the suitability of SWCNTs for each particular application due to the strong structural dependence of their properties[103]. Despite the existence of complex separation techniques that can achieve a high degree of purity of SWCNT with specific features[104-106], developing methodologies to selectively produce

SWCNT stays in the spotlight of researchers as a more efficient and economically viable option.

Catalytic chemical vapor deposition (CVD) is currently one of the most commonly used methods for the synthesis of SWCNTs. Some of its main advantages are a relatively low cost and high degree of control and scalability[15]. A typical CVD scheme operates at temperatures ranging from 600 to 1300 K, and pressure between 1 and 5 atmospheres. Supported or floating transition metal nanoparticles in a gas phase reactor are used as catalysts and hydrocarbons, ethanol, methanol, CO_2 or CO are usually the carbon sources[107-108]. Experimental[109-110] and theoretical studies[38, 111-113] aiming to reveal the growth mechanisms at the atomic scale have allowed the elucidation of important features of the catalyst and the nanotube during the nucleation and growth stages and continue to bring questions that motivate further research into each aspect. One example in particular is the observation of SWCNT growth on pure transition metal catalysts[114] and on carbide nanocatalysts[51, 115], raising questions such as what is the role of C atoms dissolved in the nanoparticle? How can they affect the structure and activity of the catalyst? And how does the structure of the catalyst influence the type of carbon nanostructure grown on its surface?

A fundamental aspect that may be crucial to determine the final nanotube structure during CVD is the correlation between the nascent nanotube and the structure of the nanocatalyst. Among proposed growth mechanisms, a *template effect* in which the nucleation process of the nascent cap structure is guided by the structure of the supported nanocatalyst has been predicted and observed[36, 113, 116]. The opposite case where the nanocatalyst accommodates its shape to the growing carbon nanostructure has also been observed and is known as *inverse template effect*[117]. The second case is more likely to be observed during synthesis using a floating catalyst[118-120]. Current experimental techniques such as electron scanning microscopy have allowed *in situ* atomic scale observations, providing evidence of the influence that the nanoparticle structure can have on the nascent nanotube[116, 121]. Such observations can be further examined and interpreted with the use of quantum mechanical calculations. Computational tools such as density functional theory (DFT) and *ab initio* molecular dynamics (AIMD) are helpful providing relevant information to elucidate the key aspects of the catalyst that may be determinant of the nanotube structure. Consequently, exploring and understanding the structure and chemical nature of the nanocatalyst becomes a required step toward elucidating growth mechanisms and using them as tools to devise control strategies over the structure of SWCNTs.

Ni, Co, and Fe are the most common catalysts in SWCNT synthesis. DFT calculations of Ni nanoparticles in contact with model nanotubes have been previously studied and reported in the literature. Borjesson *et al*. investigated the effect of the $Ni_{55}C_x$ carbide composition on SWCNTs growth by estimating the binding energies between SWCNTs with specific chiralities (namely (3,3), (5,5), (9,1) and (10,0)) and both Ni and Ni carbide particles. They concluded that nanotubes interact more strongly with the pure metal than with the carbide; however the difference was reported as small compared with the total adhesion energies[122]. Wang *et al*. also studied adhesion energies, chemical potential and charge distribution between Ni_{55} clusters and selected nanotube caps with chiralities

(5,5), (6,5) and (9,0). The energetics of the different carbon structures in contact with the nanoparticle showed small differences and were characterized by electron transfers between the nanoparticle and the nanotube[123].

The dynamics and stability of a carburized nanocatalyst at the synthesis temperature, its local composition, shape, electronic structure, and interactions with nascent nanotube caps are the focus of the present work. Although the dynamic evolution of the catalyst and the nanotube has been studied in the past using reactive classical molecular dynamics providing a step-by-step picture of the catalytic process, diffusion in the nanoparticle, and incorporation into the growing nanotube of the precursor carbon,[55,54] it is important to gain further insights of the effects of electronic distribution without the bias imposed by effective force fields. Here we use AIMD to study the dynamics of a carburized Ni nanoparticle at typical CVD synthesis conditions and the same nanoparticle in contact with model nanotube caps resembling the early stages of nanotube growth. Because the extension of the simulated time frame is limited and phenomena such as the incorporation of C atoms to the nanotube rim are not included, this study resembles growth in the limit of low pressure of precursor gas. Comparisons between the pure metallic particle and the carburized particle help to elucidate the interactions of these catalysts with the growing carbon nanotube.

3.3 Computational Methodology

We use spin-polarized DFT calculations with the Perdew-Burke-Ernzerhof exchange-correlation functional[79] implemented in the Vienna *ab initio* simulation package

(VASP)[124-128]. The electron-ion core interactions are treated with the projector augmented wave (PAW) pseudo-potentials[81, 129] and the valence charge density with a plane wave basis set with a cutoff energy of 400 eV. The geometry relaxations were performed using the conjugate gradient algorithm with an energy stopping criterion of 10^{-3} eV, and for the electronic self-consistent loop 10^{-4} eV was employed. A Gaussian smearing with a 0.05 eV width was used. AIMD simulations were performed using the NVT ensemble at 750 and 1000 K with the Nosé thermostat and a time step of 1 fs. A Γ-point Brillouin zone sampling for integration in the reciprocal space was used for energy relaxations and in AIMD simulations. Estimation of atomic charges was performed using the Bader charge analysis scheme, in which the electronic charge density enclosed within an atom defined by zero flux surfaces corresponds to the total electronic charge of said atom[130-131]. The base model in our simulations is a 55-atom Ni nanoparticle in a cubic box with side length of 3 nm, allowing sufficient space to avoid interactions with periodic images in any direction. Modifications to our model include the successive addition of C atoms into octahedral sites to resemble carbon dissolution and carbide formation, followed by attachment of chiral nanotube caps over the nanocatalyst structure.

Our initial model consists of a 55-atom unsupported Ni nanoparticle constructed using Materials Studio®[132]. The nanostructure was built taking a Ni face-centered cubic (fcc) crystal as a base. After relaxation of the initial structure, a progressive addition of C atoms into octahedral sites within the nanoparticle structure was performed. For each C addition the nanoparticle structure was allowed to relax. C atoms were added until saturation of the octahedral sites inside the nanoparticle was reached while maintaining a stable structure (Figure 3.1). The energy of interaction of the individual carbon atoms was estimated by subtracting the sum of energies of the nanoparticle without carbon (E_{Ni55}) and number of C atoms (n) times the energy of an isolated carbon (E_C) atom from the energy of the system (E_{Ni55Cn}). The result was normalized dividing by the number of carbon atoms added.

$$E_{\text{int}} = \frac{E_{Ni_{55}C_n} - \left(E_{Ni_{55}} + nE_C\right)}{n} \qquad (3.1)$$

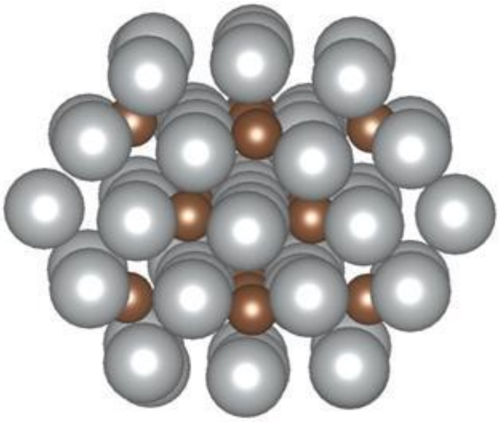

Figure 3.1 Side view of the structure of Ni55C14 after locating C atoms in the inner octahedral interstitial sites of a Ni55 unsupported cluster. Gray and brown spheres represent Ni and C atoms, respectively.

In order to study the interactions of the nickel nanoparticle and the carbon atoms dissolved within its structure with the nascent nanotube, model nanotube caps were constructed using the software CaGE[133]. Nanotube caps were built taking into account the isolated pentagon rule, according to which the stability of the cap is favored when the six pentagons needed in the structure are isolated from one another[134]. Figure 3.2 illustrates the model carburized nanoparticle in contact with the nanotube caps. Four model nanotube caps were considered for nanotubes with chiral indexes (8,7), (9,6), (11,5), and (13,0) in representation of chiral nanotubes with semiconducting (Figure 3.2a) and metallic character (Figures 3.2b and 3.2c) and zigzag nanotubes with semiconducting character (Figure 3.2d). The cap indexes were selected to obtain nanotubes with a diameter slightly larger than the nanoparticle diameter. The caps were placed in contact with relaxed structures of $Ni_{55}C_{14}$ nanoparticles.

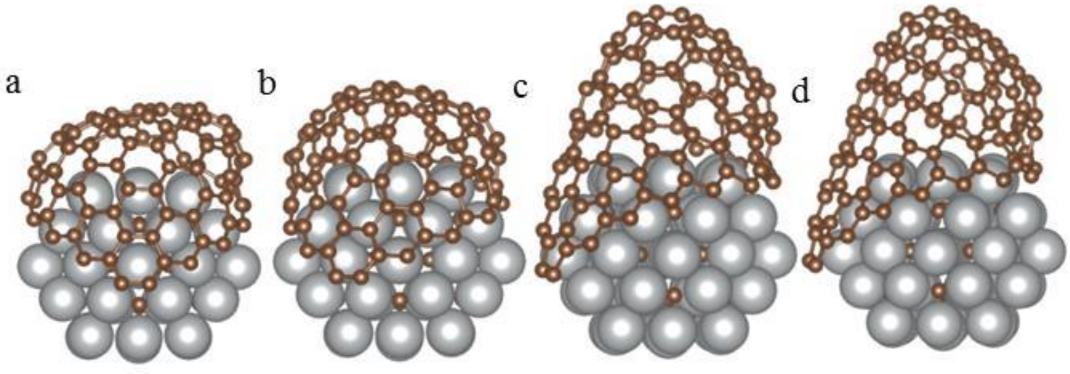

Figure 3.2 Side view of the structure of the carburized $Ni_{55}C_{14}$ in contact with four different nanotube cap models with chiral indexes (n,m): a. (8,7), b. (9,6), c. (11,5) and d.(13,0). Gray and brown spheres represent Ni and C atoms, respectively.

The dynamics of the carbon atoms inside the unsupported Ni nanoparticle at two different temperatures, 750 K and 1000 K, was studied during 8 ps for two different compositions $Ni_{55}C_{10}$ and $Ni_{55}C_{14}$ using AIMD simulations. Further AIMD for the $Ni_{55}C_{14}$ nanoparticles in contact with four different model nanotube caps was carried out for a simulation time of 3 ps. The individual trajectories of carbon were followed to obtain useful information about the dynamic evolution of the nanocatalyst structure, the influence of the nascent nanotube and the occurrence of carbon association.

3.4 Results and Discussion

3.4.1 Energetics of Carbon Dissolution and Evolution of Atomic Interactions

Table 3.1 shows that for each successive addition of C atoms to the Ni nanoparticle, the energy of the carburized particle is lower than the sum of the energies of the Ni nanoparticle and C atoms separately. Thus, the incorporation of C atoms into the nanoparticle structure is thermodynamically favorable, as expected for transition metals capable of dissolving carbon. Across additions the energy of interaction is consistent (mean=-6.49, standard deviation=0.12).

Table 3.1 Energy of the system and energy of interaction for each successive addition of carbon into the Ni nanoparticle as defined in eq 3.1.

#C atoms	0	1	2	4	6	8	10	14
E_int. (eV)	0.0	-6.48	-6.40	-6.57	-6.59	-6.57	-6.55	-6.27

The composition of the particle once the octahedral sites were occupied without deformation of the particle shape and structure was $Ni_{3.92}C$. This C concentration is lower than those of stable or metastable carbides such as Ni_3C and Ni_2C. The ability of a Ni nanoparticle to dissolve C is dependent on its size and the conditions it is exposed to (temperature and C chemical potential). Systematic analyses of the stability of carburized Ni nanoparticles have been performed using computational tools such as tight binding and Monte Carlo simulations[135-136] reporting that carbon solubility tends to increase with: a) decreasing particle size, b) increasing temperature, c) increasing chemical potential (pressure of precursor gas). Similar behavior has also been observed for other transition metals[137]. Generally, a nanoparticle has a much higher limit of C dissolution than a bulk metal has, which in turn affects the melting temperature by decreasing it at growth conditions[137]. Thus, it is expected for the particle morphology to change dramatically from that shown in Figure 3.1. This has been clearly observed using classical molecular dynamics simulations at the CVD temperatures (~ 1000 K)[54-55] and *in situ* experimental techniques such as environmental transmission electron microscopy (ETEM) imaging of SWCNT growth on Ni and transition metals, in which structural fluctuations and reshaping effects are present with[50] and without[138] (negligible) carbon dissolution Though carbide phases have been identified in nanoparticles at growth conditions[121, 138], there is still a debate regarding the formation and stability of carbide or surface carbide during the SWCNT process. Here minimum distances between C-C, Ni-C and Ni-Ni atoms were monitored throughout the AIMD simulations to observe variations in the nanoparticle structure and evaluate whether association among C atoms dissolved in the nanoparticle would be possible.

Figure 3.3a illustrates the minimum distances between Ni and C atoms in the carburized Ni nanoparticle of composition $Ni_{55}C_{14}$ at 1000 K. Ni-Ni distances were observed to be maintained about an average value of 2.27 Å, which is in fair agreement with typical Ni interlayer distances in Ni carbides[139-140]. Ni-C minimum distances show little variation around an average value of 1.76, in agreement also with distances found in Ni carbides[139-140]. C-C minimum distances were found to be kept out of range for C-C bond formation, with a lowest minimum distance of 2.29 Å. Therefore C-C association inside the nanoparticle is not found. The average minimum C-C distance is 3.11 Å with a standard deviation of 0.22 Å, showing greater variability with respect to Ni-C and C-C.

Higher variation of the C-C minimum distance accompanied by a gradual increase in its value is a reflection of the dynamics of C atoms migrating from their original octahedral positions towards the subsurface of the nanoparticle. Such migration process is further illustrated in the analyses of individual atom-pair distances followed throughout the simulation time. The effect of varying nanoparticle composition and temperature was found to be practically insignificant for Ni-Ni and Ni-C minimum distances. Variations in C-C minimum distances for different compositions and temperature can be attributed to statistical variability within each set of conditions.

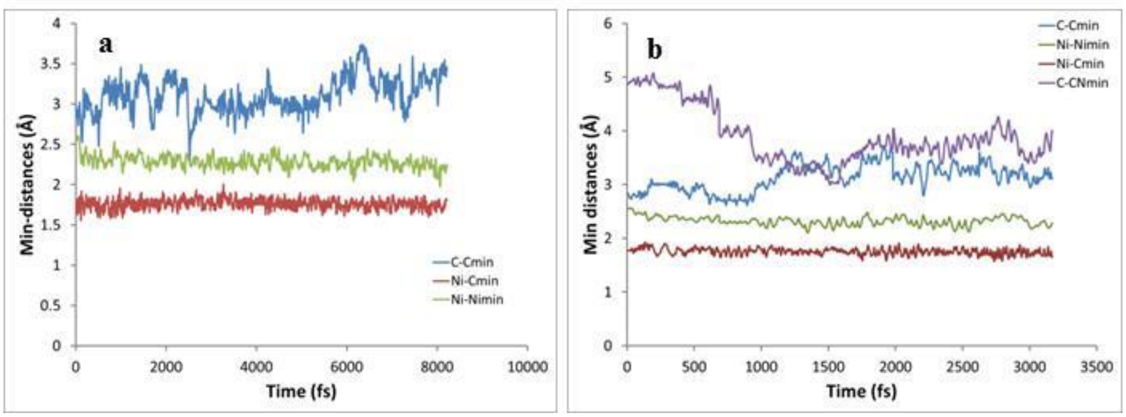

Figure 3.3 Monitoring of minimum distances found during the simulated time between Ni-Ni, Ni-C, C-C and C-CN, where C-C refers to distances between C atoms inside the nanoparticle and C-CN are distances between C in the nanotube cap rim and C atoms dissolved in the nanoparticle. a) $Ni_{55}C_{14}$ at 1000 K and b) $Ni_{55}C_{14}$ in contact with the nanotube cap of indexes (8,7) at 750 K.

3.4.2 Interactions Between a Carbon Cap and the Carbide Nanoparticle

Figure 3.3b shows the dynamic evolution of the minimum distances between Ni and C atoms for the carburized nanoparticle having a (8, 7) nanotube cap attached to its surface (shown in Figure 3.2a). Ni-Ni and Ni-C minimum distances showed little variation with respect to the type of cap in contact with the nanoparticle, with average distances of 2.33 Å and 1.79 Å respectively. These values remained almost constant throughout the simulation time. The C-C minimum distances increased as the simulation progressed as a result of the bulk diffusion of the C atoms inside the nanoparticle and migration toward the subsurface. In Figure 3.3b we analyze the minimum distances between C atoms in the rim of the nanotube cap and the C atoms inside the nanoparticle (named C-CN). In all four cases of caps studied, minimum C-CN distances were out of range for bonding interactions between C atoms during the extension of the simulation.

Thus, chemical association between the C atoms dissolved in the nanoparticle and the C atoms in the cap rim was not observed. Nevertheless, the occurrence of such association has been reported for nanoparticles with higher C content, where the incorporation of diffusing C atoms from the bulk of the nanoparticle into the nanotube rim has been observed for longer simulation times in classical molecular dynamics[141]. Although the migration of C atoms from the inner octahedral positions to the subsurface of the nanoparticle was evident, segregation to the exterior of the nanoparticle was never observed. This lack of carbon nanostructure growing pattern is attributed to a C concentration below that corresponding to saturation of the nanoparticle; *i.e.*, even though all the octahedral sites were occupied (as it would be in the case of carbide formation), the nanoparticle may still dissolve more C atoms adopting a non-carbide structure, as observed in classical MD simulations of the SWCNT growth[46, 54-55] before it becomes saturated and C atoms are segregated to the surface. This suggests that a particle with the pure carbide structure wouldn't facilitate the precipitation of C atoms to the surface, because their Ni-C interaction energies are too strong (Table 3.1). However, during SWCNT growth, the particle is under additional carbon pressure (not included in our simulations) that would facilitate saturation of the catalytic nanoparticle and subsequent carbon segregation to the surface and formation of carbon nanostructures.

3.4.3 Dynamics of the Atomic Pair Interactions

Further insights can be obtained from the analysis of individual pairs of adjacent C atoms, Ni atoms, and Ni and C atoms that were randomly selected to be monitored throughout the simulation. The analysis reveals structural and chemical changes in the nanostructure of the carburized nanoparticles. A minimum of ten pairs of atoms for each pair type was considered in each simulation. The bars depicted in Figures 3.4a, 3.4b, and 3.4c represent the number of distances between pairs that fall within a specific range of distances (Δd = 0.2 Å). Figure 3.4a illustrates the behavior of the selected atom pairs in the carburized $Ni_{55}C_{14}$ nanoparticle at the beginning of the simulation, with C atoms located in octahedral sites at 1000 K. Distances between pairs of Ni atoms and Ni-C in the inner and outer layers of the nanoparticle show a narrow distribution, reflecting the initial state of order of the C atoms with respect to Ni and Ni within the original structure. The wider distribution of C-C distances arises from the fact that C atoms were initially located spread across the extension of the nanoparticle in octahedral positions. As the simulation progresses, the most significant changes observed in Figure 3.4b are the inner and outer distances of Ni-Ni pairs, which become wider as the Ni atoms in the nanoparticle fluctuate their position as a result of the high temperature dynamics. The distribution of C-C distances becomes even wider as some C atoms begin migrating towards the subsurface. Evidence of this C migration process is also observed from the inner Ni-C distribution becoming considerably flatter and wider than other distributions, thus indicating changes in the nanoparticle internal structure and the relative position of C atoms inside the Ni cluster. In contrast, the overall dynamic effects on the outer Ni and C atoms are balanced in such a way that the outer Ni-C distances maintain a narrow distribution approximately in the same range.

Figure 3.4c shows the distribution of pair distances after 8 ps of simulation. At this point the nanoparticle structure is closer to an equilibrium state evidenced by narrower distributions of Ni-Ni and Ni-C with defined peaks located at 2.5- and 1.9-Å, respectively. Although the C-C distribution is wider here than at an intermediate stage, the presence of a peak at 3.6 Å indicates a relative ordering of the C atoms to some extent after migrating from their initial octahedral location to the subsurface. These results are in conformity with the pair radial distribution function (RDF) of all pairs of atoms in the nanoparticle with peaks located at 2.45-, 1.85-, and 3.45-Å for Ni-Ni, Ni-C and C-C respectively and comparable relative width (Figure A.1 in Appendix A).

An increment in the width of the distribution of C-C peaks is observed for the nanoparticles with higher C content due to an increased driving force for the migration of the C atoms dissolved in the nanoparticle toward the subsurface. At low temperature the distribution of Ni-Ni and Ni-C distances tends to be narrower for the nanoparticles with higher C content as the arrangement of atoms is more structured, whereas the opposite occurs at higher temperature where the dynamics plays a more important role in the relative motion of the atoms in the nanoparticle. Estimation of the C diffusion coefficients supports these ideas, as the motion is increased with increasing temperature and increasing carbon content (Table A.1 in the Appendix A information). In turn, a reduction in the sharpness of the C-C peaks is observed for the nanoparticles with lower C content. In all cases, the differences between inner and outer Ni-C and Ni-Ni distances are insignificant.

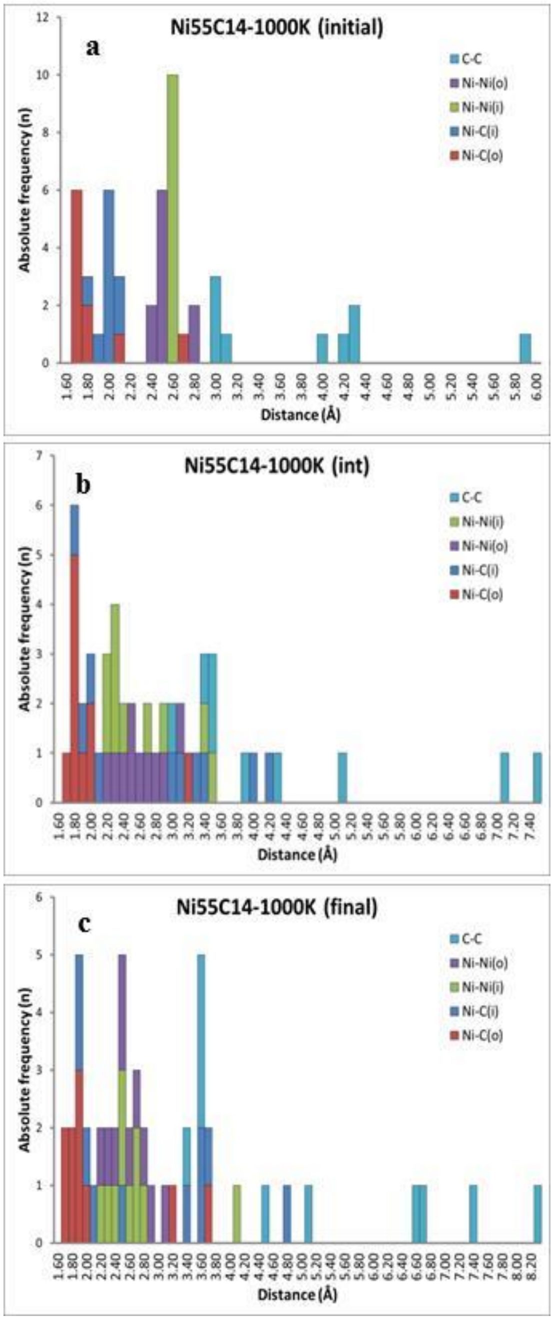

Figure 3.4 Histograms indicating the absolute frequency of atom pairs separated by a specific distance in the Ni55C14 carburized nanoparticle at 1000 K at a given simulation time: a) initial ~ 0 ps b) intermediate ~ 4 ps and c) final ~ 8 ps. Bar color code: C-C (blue), Ni-Ni(o) (purple), Ni-Ni(i) (green), Ni-C(i) (blue) and Ni-C(o) (red). The legend in parenthesis indicates whether the atoms were initially located at the nanoparticle surface (o) or the interior of the nanoparticle (i).

3.4.4 Nanoparticle Morphology

Small changes in the overall shape of the nanoparticle are observed throughout the simulation. The unsupported carburized nanoparticles maintained a spherical shape characterized by the absence of stable, well-defined facets as the positions of the surface atoms presented small fluctuations due to the temperature-induced dynamics. Typical catalysts used in the synthesis of single walled carbon nanotubes that may exhibit well-defined facets have been reported[121]. Such structural features of the catalyst are believed to play an important role in the adsorption and lift off of the nascent nanotube cap. A significant factor that influences shape in real catalysts is the presence of a substrate, which depending on the strength of the metal-support interaction, may exhibit a more defined structure and thus may have a significant influence on the nanotube structure (template effect)[55, 116-117, 142]. In our model systems, the absence of a substrate leads to a moldable structure of the nanoparticle that can accommodate to the growing nanotube shape. This effect is known as inverse template effect[117] and can be observed in Figure 3.5. Round caps such as those of (8,7) and (9,6) help maintain a spherical shape in the nanoparticle; narrower and more elongated caps such as those of (11,5) and (13,0) cause the nanoparticle to adapt its shape to match more closely the shape of the nascent nanotube (Figures 3.5c and 3.5d). Similar reshaping effects have been observed from ETEM studies of SWCNT tip growth, a mode of growth in which the nanoparticle detaches from the substrate and remains attached to the nanotube tip, allowing greater mobility of the metal atoms and accommodation of the nanoparticle to the nanotube structure *via* capillary-driven surface diffusion.[143]

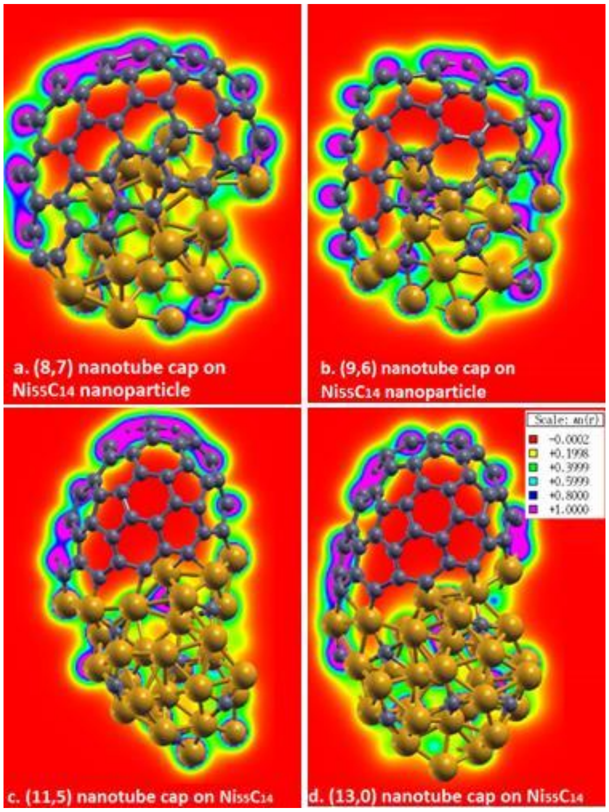

Figure 3.5 Electron density maps for the carburized nanoparticle with a cap of chiral indexes a. (8,7), b. (9,6), c. (11,5), and d. (13,0). The color images were obtained using the software XCrySDen[144].

3.4.5 Electronic Distribution

Changes in the electronic structure of the different nanoparticles considered in this study are examined by estimating partial atomic charges and charge differences using a grid-based Bader analysis algorithm[131], plotting electron density maps, and calculating the electron density of states. The distribution of charges between Ni and C atoms in the carburized nanoparticle is slightly shifted with increasing carbon content and is not affected by changes in temperature. The average magnitude of the Ni and C atomic charges are +0.12 e and -0.68 e respectively for $Ni_{55}C_{10}$, whereas for $Ni_{55}C_{14}$ the Ni and

C average charges are +0.18 e and -0.69 e respectively. Thus, the addition of C atoms to the carburized nanoparticle causes a stronger attraction between Ni and C evidenced by a slight increase in the magnitude of the average charges in both cases. This may also be a contributing factor to the wider distributions observed for the Ni-Ni and C-C distances in $Ni_{55}C_{14}$.

The electron density of the nanoparticles with and without model nanotube caps, after 3 and 8 ps of AIMD respectively, was mapped on planes parallel to the z direction. These planes were located to intersect rich regions of electron density in the nanoparticle and bonding between the nanotube C atoms as illustrated in Figure 3.5. The regions in red indicate the absence of electron density. The space around the nanoparticle is devoid of electron density showing that the size of the simulation box is sufficiently large to prevent interactions with periodic images. The electron density is localized around the closest contacts between C atoms in the nanotube cap and the Ni atoms at the nanoparticle surface, where catalyzed addition of C to atoms to the nanotube rim occurs. In all cases, high population of electron density is concentrated around C atoms both in the nanoparticle and the nanotube cap with electron densities of around 1 $e/Å^3$(pink regions), whereas an intermediate electron density population is found around Ni atoms (green regions). This suggests the occurrence of interactions involving charge transfer between Ni and C atoms, as revealed by their respective charges. Similar results have been reported in previous studies with pure Ni_{55} clusters indicating an electronic charge transfer from Ni atoms to C atoms at the nanotube edge[123]. In order to visualize and describe such interactions, further calculations of charge differences were performed for the nanoparticle with nanotube caps (combined system) and each individual component of the system (nanoparticle and nanotube cap); they are discussed in the next section.

To further understand the role of C atoms dissolved in the nanocatalyst structure, an estimation of the energy of adhesion of the nanotube cap to the nanoparticle was performed on both pure Ni_{55} and the $Ni_{55}C_{14}$ carbide nanoparticles in contact with the four model nanotube caps, after running in AIMD for a time sufficiently long to reach equilibration. The energy of adhesion (depicted in Figure A1.3) per carbon atom at the nanotube rim is fairly similar between metal and carbide nanoparticles. The maximum difference between energy of adhesion for a particular nanotube cap is 0.14 eV/C atom and no apparent preference for the nanotube models studied to attach to either nanoparticle were found.

3.4.6 Reactivity of the Nanoparticle

Regions of electron accumulation and depletion were calculated for the four nanotube caps in contact with the $Ni_{55}C_{14}$ nanoparticle to display an isosurface with an isovalue of 0.03 e/$Å^3$. Figures 3.6a and 3.6b illustrate the accumulation and depletion of electron density as result of the interaction between the carburized nanoparticle $Ni_{55}C_{14}$ and the nanotube cap of indexes (9,6). Regions of electron accumulation are mainly localized at the space between the C atoms of the nanotube cap rim and the surface Ni atoms in direct contact with them.

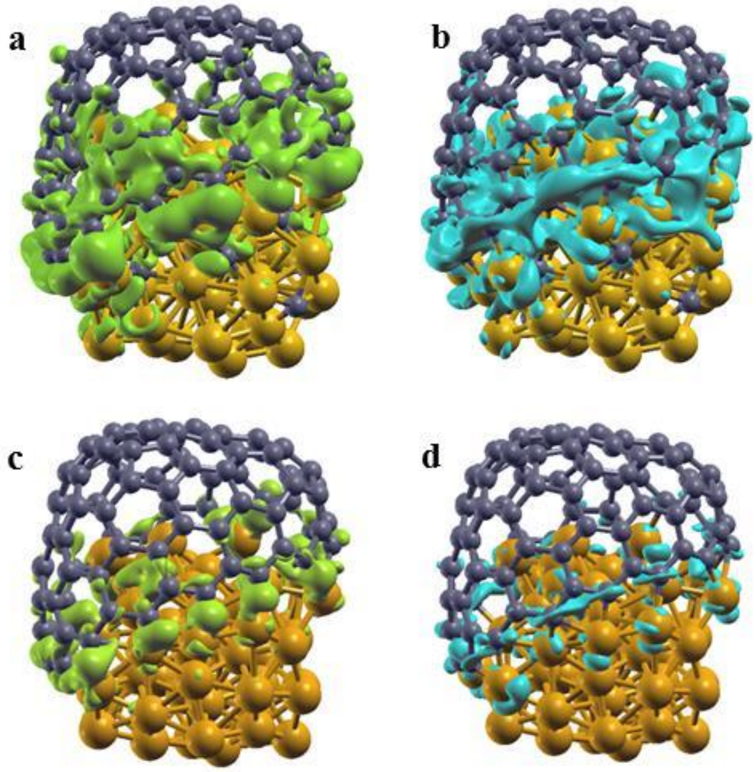

Figure 3.6 Charge density difference analysis for $Ni_{55}C_{14}$ (a and b) and Ni_{55} (c and d) nanoparticles in contact with a nanotube cap with chiral indexes (9,6). Green regions in a and c correspond to electron accumulation. Blue regions in b and d correspond to electron depletion.

This region of confined electron density provides an adequate reactive environment for the continuous incorporation of C atoms from the precursor environment in a typical CVD scheme. [145-146] Other regions of electron accumulation are located at the hexagons closest to the nanotube rim which may provide an environment that allows bond flexibility in the growing carbon lattice. This reasoning is consistent with previous observations indicating that C atoms in the vicinity of the rim are able to relocate within the nanotube network allowing the healing of defects[147]. Regions of electron depletion are mainly located in two types of regions: 1. Ni atoms in close contact with the nanotube cap. 2. Around C-C bonds located at the nanotube rim. This suggests that once C atoms have been incorporated into the nanotube rim, they partially donate their electron "share" to their neighbor Ni and C atoms in the vicinity of the rim, thus contributing to the reactivity of the nanotube-nanoparticle interface region and flexibility of the nanotube lattice near the cap rim. [146]

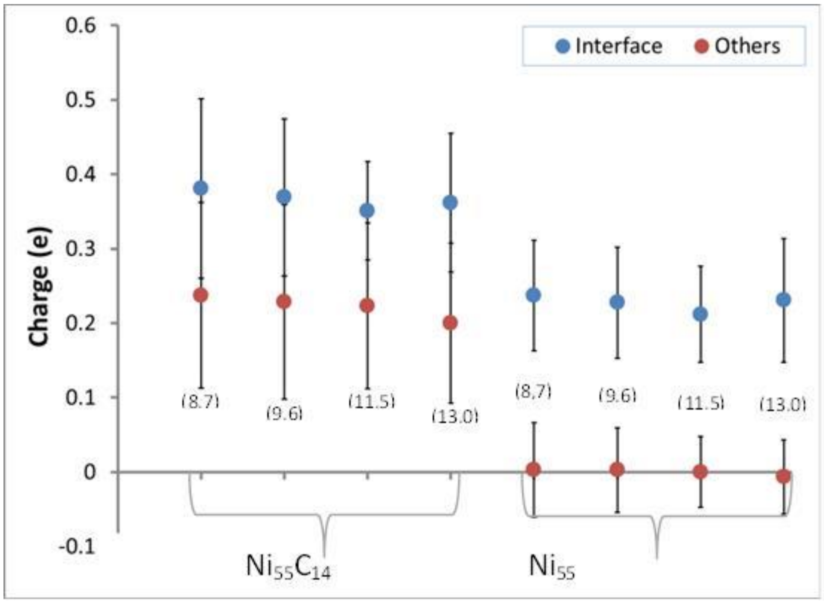

Figure 3.7 Average partial atomic charges for Ni atoms in $Ni_{55}C_{14}$ and Ni_{55} placed in contact with nanotube caps. Distinction is made between Ni atoms at the surface in contact with the cap (blue) and the remainder of Ni atoms (red).

The accumulation and depletion of electron density as result of the interaction between the Ni_{55} nanoparticle and the nanotube cap of indexes (9, 6) is depicted in Figures 3.7c and 3.7d. Regions of electron accumulation and depletion are located analogously in the metallic cluster Ni_{55} as in the carburized nanoparticle $Ni_{55}C_{14}$, however the degree of accumulation or depletion of electron density is notoriously larger in the carburized nanoparticle. The smaller individual regions of accumulation between the Ni surface atoms and the C atoms of the cap rim observed in Ni_{55} appear as a larger and more continuous region extended along the nanotube rim for $Ni_{55}C_{14}$. Similarly, disconnected depletion regions in the former appear merged in the latter. The implications of this observation may be significant in terms of reactivity, as electron rich environments are known to provide favorable conditions for sustained catalytic activity[148]. The presence of dissolved C atoms affects the electronic structure in the catalytic nanoparticle, increasing the strength of its interaction with the nascent nanotube and leading to larger electron accumulation and depletion regions. Evidence for the differences in the electronic structure of the two types of nanoparticles is found from the charge analysis of Bader and electron density of states. The density of states of Ni_{55} exhibits a population of electronic states concentrated in a smaller range of energies, and a lower density of unoccupied states above the Fermi level than $Ni_{55}C_{14}$, which is in agreement with electron accumulation and depletion diagrams and may be indicative of a higher reactivity of the $Ni_{55}C_{14}$ nanoparticle. Figure A.3 shows a comparison of DOS for both nanoparticles in contact with the (8, 7) cap. The analysis of charges summarized in Figure 3.7 also suggests a difference between the electronic structures of the two nanoparticles. Each Ni atom in both nanoparticles was classified as either “interface”, if the atom was in direct contact with the nanotube rim, or “other” if it was located anywhere else. Regardless of the type of cap, all interfacial Ni atoms had an average partial charge of $0.4e^-$ for the carburized nanoparticle whereas the same for the metal nanoparticle was close to around $0.2e^-$. Other internal and peripheral Ni atoms had an average close to $0.23e^-$ for the first case, whereas for the second it was close to $0.0e^-$. Thus, the presence of C atoms in the nanoparticle affects also Ni atoms not interacting directly with the rim, which may be exposed at the surface and may also contribute to the catalysis by virtue of a partial charge as opposed to being neutral as in the case of the pure Ni_{55}. It is worth mentioning that caps with different chiral indexes behaved in a similar fashion concerning the electronic structure description presented above.

3.5 Conclusions

The dynamic evolution of unsupported carburized Ni nanoparticles during the pre-growth and growth stages of single-walled carbon nanotubes was studied using density functional theory and *ab initio* molecular dynamics simulations. Carbon dissolution and stability of the carburized metal nanoparticle are observed throughout the simulation. Structural changes in the nanocatalyst structure are monitored through the extension of the simulation showing that in the absence of a substrate, the nanocatalyst fails to maintain a defined faceted structure. However, the floating catalyst accommodates to the shape of the nanotube in accordance with what is known as an “inverse template effect”[117]. The lack of association of carbon atoms inside the nanoparticle and evidence of short-range ordering from distance- and radial distribution function analyses may be indicators of the stability and potential for evolution of the nanoparticle system into a more thermodynamically stable phase such as that of a carbide phase. Moreover, lack of incorporation of C atoms from the nanoparticle into the nanotube rim may support the idea that a state of saturation or supersaturation of the nanoparticle is needed for precipitation of C from the stable Ni-C core to the surface, and incorporation to the nanotube rim to occur, leaving the most of the catalytic growth to the surface-diffusing C species as reported in previous studies[54]. Analyses of the electronic structure of the nanoparticle during growth reveal that a charge transfer process occurs from the surface Ni atoms and rim C atoms to the interfacial region between the growing nanotube and the nanoparticle. This process leaves an interfacial region rich in electron density, where incorporation of precursor C may continue the growth process, and electron-depleted regions in the vicinity of the nanotube rim that may allow rearrangement of the C atoms near the rim and healing of defects. A comparison between the charge transfer in a carburized nanoparticle and a pure metal nanoparticle reveals that the process occurs similarly in both systems, but in the case of the carburized nanoparticle the interfacial region is larger and almost continuous along the nanotube rim, whereas the metal nanoparticle displays a smaller and more localized accumulation region. Surface Ni atoms that are not in direct contact with the cap are also affected: a neutral charge characterizes surface Ni atoms in the pure nanoparticle, and positively charged Ni atoms are found at the carburized nanoparticle surface. These observations suggest that the carburized nanoparticle may be able to offer a more reactive environment for nanotube growth than the metallic one. Altogether, continued exploration of the structural and electronic characteristics of the nanocatalyst and its interactions with the growing nanotube in SWCNT synthesis may contribute with valuable insight that will eventually allow us to control the structure and properties of SWCNT.

CHAPTER IV

STRUCTURE OF SUPPORTED AND UNSUPPORTED CATALYTIC RH NANOPARTICLES: EFFECTS ON NUCLEATION OF SINGLE-WALLED CARBON NANOTUBES

4.1 Summary

Achieving a better control of the nucleation and growth of single-walled carbon nanotubes requires understanding of the changes in the catalyst structure and the interfacial phenomena occurring at the solid surface and the gaseous phase from the early stages of the synthesis process. Carbon nanotubes produced by chemical vapor deposition typically use carbon-philic metal catalysts such as Fe, Ni and Co, in which both surface C and dissolved C atoms contribute to the nanotube formation. In the present work, we use density functional theory to investigate the interactions of Rh, a noble metal, with carbon both as individual atoms gradually deposited on the catalyst surface from the precursor gas decomposition and as a nucleating seed adhered to the catalyst. Adsorption and limited dissolution of carbon atoms in the subsurface are found to be favorable in unsupported clusters of various sizes (Rh_{38}, Rh_{55} and Rh_{68}) and in Rh_{32} clusters supported on MgO(100) and MgO(111) surfaces. Changes in solubility, electron density transfer, and interactions of the Rh clusters with the support and the nascent nanotube are explored for increasing contents of carbon adsorbed on or dissolved inside the particles. A discussion on how such factors affect the lattice and electronic structure

of the catalyst particles is presented in the interest of obtaining insight that will allow the design of improved catalysts for controlled nanotube synthesis.

4.2 Introduction

The catalytic synthesis of carbon nanomaterials such as single-walled carbon nanotubes (SWCNTs) is typically carried out by chemical vapor deposition (CVD) using iron-group metal nanoparticles (Fe, Co, and Ni).[15] However, successful synthesis of carbon nanotubes has also been recently achieved on noble metal catalysts including Au[149-150], Pt[151-152] and Rh[153-154]. The interest in SWCNTs stems from their ample variety of applications[2] including electronic devices[6], biomedical applications[94], coatings[155], energy[4] and separations[156]. The possibility of producing nanotubes with specific structural features and properties requires achieving a high degree of control during the synthesis process. Therefore, it is important to understand the nucleation and growth mechanisms of SWCNTs to develop controlled synthesis strategies. In the current work, we use quantum mechanical simulations to look at the early stages of SWCNTs nucleation on Rh nanoparticles, beginning with carbon adsorption and dissolution, and seeking to discern the interactions between the catalyst particle with carbon and a metal oxide support.

Single-walled carbon nanotubes with a narrow diameter distribution between 1.1 and 1.4 nm have been grown on Rh/SiO_2 supported nanoparticles with the same range of diameter distribution. The narrow distribution observed was attributed to the high melting point of pure Rh catalyst.[154] High control of nanotube alignment and diameter distribution has been reported for Rh particles supported on silica and alumina,[157] and SWCNTs with preferential metallic behavior were synthesized on Rh/Si_3N_4 for various carbon sources, suggesting that the selectivity toward metallic nanotubes is due to structural features in the Rh particles.[153] However, the nucleation mechanisms of SWCNTs on noble metals such as Rh remain poorly understood and require further exploration.

On the interactions of noble transition metals and carbon, early studies of the structure and stability of transition metal carbides pointed at ‘outlying’ carbides with metals from the Pt-group (Ru, Rh, Pd, Os, Ir, and Pt) being highly unstable or non-existent.[158] Subsequently, estimation of the energy of formation and cohesion for various stoichiometries of bulk Rh carbides using *ab initio* calculations showed that particles with low C content have higher stability ($RhC_{x \leq 0.25}$).[159] Other studies have looked at molecular orbital analyses of the Rh-C molecular bond revealing the possible electronic states and high bond dissociation energy due to contributions from σ and π bonds; however, when considering interactions with other Rh atoms in the crystal, the bonding energy and electron transfer have been observed to depend on the structure and surface coordination number of Rh.[159-160] For small Rh_n metal nanoparticles ($n < 55$ atoms), high-density and close-packed configurations of Rh clusters are reportedly stable.[160] In general, low- energy transition metal nanoparticle structures include octahedrons, dodecahedrons, and icosahedrons, which represent low-energy structures depending on the particle size, with cases where more than one structure may have similar energy for a given size.[161] For instance, both icosahedral and octahedral structures of 55-atom Rh nanoparticles have been found to be stable, with the first type being slightly more stable than the latter.[160]

The structure, stability, and reactivity of nanoparticles can also be determined by the type of interactions of the catalyst particle with the support from the deposition of the catalyst on the substrate[162] and through the catalytic process.[163] For instance, modifications to alter the acidity/basicity of the support have been explored in Fe_2Co/Al_2O_3 and have been found to affect the activity and selectivity of the catalyst, with basic supports showing better performance.[22] Such behavior is attributed to involvement of the support in the reaction; however, it is believed that catalyst-support interactions and charge transfer at the interface may also influence the metal particle structure and properties.[163]

In this work, we seek to model the early stages of the nanotube nucleation process on unsupported and supported RhC_x nanoparticles with overall composition of carbon in the range of x = 0 to x = 0.5, using density functional theory (DFT). Rh particles with sizes ranging between 0.8 and 1.1 nm with low-energy structures[161] were considered as models. Two surface terminations of the MgO support are considered: MgO(100) and MgO(111). A description of the changes in the nanoparticle and nascent nanotube during nucleation is presented in terms the particle structure, energy of interaction with nanotube and support, and atomic charges of Rh and C atoms for increasing carbon content of the particle.

4.3 Computational Methodology

Density functional theory calculations as implemented in the Vienna *ab initio* simulation package (VASP)[124-128] were used to estimate the free energy of the system. The generalized gradient approximation (GGA) implemented in the exchange-correlation energy functional proposed by Perdew, Burke and Ernzerhof (PBE) was selected.[79] Valence electronic wave functions with a cutoff energy of 400 eV and projector augmented wave (PAW) pseudopotentials for the interactions between ionic cores and valence electrons were considered.[81, 129] Integration in the Brillouin zone was carried out with a Γ-point sampling. Electron partial occupancies were accounted for with a Gaussian smearing width of 0.05 eV. Geometry optimizations were performed using a conjugate gradient algorithm with convergence criterion of 10^{-3} eV. Electronic self-consistent iterations used a criterion of 10^{-4} eV. Atomic charges were estimated using the Bader charge analysis as implemented by Henkelman *et al*., where the electronic charge density is delimited by zero flux surfaces between atoms.[130, 164]

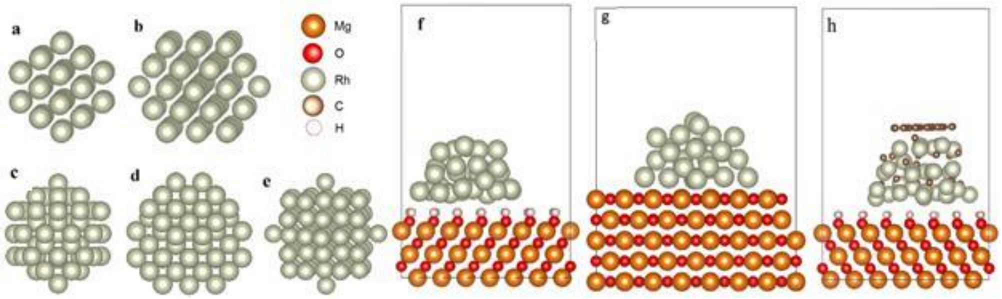

Figure 4.1 Models representing the unsupported (a) Rh_{38}-O_h, (b) Rh_{55}-O_h, (c) Rh_{55}-i_h, (d) Rh_{68}-$C3_v$, and (e) 68-O_h nanoparticles, Rh_{32} nanoparticles supported on (f) the (111) facet and (g) the (100) facet of MgO, and (h) Rh_{32} nanoparticle supported on MgO(111) with a graphene fragment adsorbed on its surface.

Two main models were considered to represent the catalytic Rh nanoparticles: (1) an unsupported model and (2) a supported model. The unsupported model consists of crystalline spherical Rh nanoparticles of different sizes: 38, 55, and 68 atoms corresponding to 0.8, 1.0, and 1.1 nm, respectively. The supported model consists of 32-atom hemispherical Rh nanoparticles deposited on a 5-layered MgO slab with either a hydroxylated (111) surface termination or a stoichiometric (100) surface termination. Unsupported nanoparticles representing low energy geometries[161] such as cubic octahedral symmetry (O_h), icosahedral (i_h), and trigonal $C3_v$ ($C3_v$) and octahedral supported nanoparticles, as illustrated in Figure 4.1, were built using the Materials Studio package.[165] The adsorption and dissolution of carbon after dissociation of the precursor gas on the catalyst surface were simulated in the model nanoparticles by progressively adding C atoms at energetically favorable locations: (a) hollow sites on the particle surface and (b) in octahedral sites of the particle subsurface, and allowing the system to relax between each addition. C atoms were placed in positions that allowed enough space between newly added atoms and previously added atoms in their relaxed positions. Incorporation of carbon into the nanoparticle proceeded until a composition of Rh_2C was reached. The change in free energy as a result of each carbon addition (energy of interaction, E_{int}) was estimated by subtracting the energy of an isolated C atom (E_c) multiplied by the number of C atoms added (n) and the particle system without carbon (E_{Rh} for the usupported particle, or $E_{Rh/MgO}$ for the supported particle) from the energy of the combined system (RhC_x or RhC_x/MgO), where x is the overall C composition expressed as the total number of C added divided by the number of Rh atoms. The final value of E_{int} is normalized dividing by the number of carbon atoms as described by eq 4.1 for the unsupported case and eq 4.2 for the supported case.

$$E_{\text{int}} = \frac{E_{RhC_x} - \left(E_{Rh} + nE_C\right)}{n} \tag{4.1}$$

$$E_{\text{int}} = \frac{E_{RhC_x/MgO} - \left(E_{Rh/MgO} + nE_C\right)}{n} \tag{4.2}$$

The adhesion energy of the cluster to the MgO support (E_{adh}) with increasing carbon content is estimated similarly by subtracting the sum of the energy of the carburized particle (E_{RhCx}) and the energy of the MgO slab (E_{MgO}) from the energy of the supported carburized nanoparticle ($E_{RhCx/MgO}$). The result is normalized dividing by the number of atoms in the particle located near the interface (n_i) with the support according to eq 4.2. Rh particles with different relative orientations with respect to the lattice of two MgO facets initially favoring: a) a high degree and b) a low degree of epitaxial match between particle and support are considered.

$$E_{adh} = \frac{E_{RhC_x/MgO} - \left(E_{RhC_x/MgO} + E_{MgO}\right)}{n_i} \tag{4.3}$$

The stability of the carbon atoms dissolved in the particle is assessed by determining the ratio of the number of carbon atoms that remain dissolved to the total number of carbon atoms added at a given C addition step. The state of a carbon atom as ‘dissolved’ or ‘adsorbed’ is determined by the number of nearest neighbors using a Rh-C cutoff distance of 2.20 Å[166]. C atoms with 5 or more metal nearest neighbors are considered to be dissolved, whereas C atoms with less than 5 metal-nearest neighbors are defined as adsorbed. Electron density maps and electron transfer are visualized using the XCrysDen[167] and VESTA[168] software.

The interactions between the supported Rh nanoparticles in their pure metal state and carburized state (selected overall composition of Rh_2C) with the nascent carbon nanotube nucleating on the nanoparticle's surface are modeled by placing a graphene fragment, consisting of 19 C atoms conforming 5 interconnected hexagons, on the surface of the supported Rh nanoparticles at a distance of 2.4 Å. The energy of adhesion of graphene to the supported Rh nanoparticle is calculated according to eq 4.4 by subtracting the energy of the supported nanoparticle and the energy of the graphene fragment from the energy of the combined system with graphene adhered on the supported Rh nanoparticle.

$$E_{adh} = E_{g+RhC_x/MgO} - \left(E_g + E_{RhC_x/MgO}\right) \tag{4.4}$$

4.4 Results and Discussion

4.4.1 Adsorption and Dissolution of Carbon in Unsupported Rh Nanoparticles

The sequential adsorption and dissolution of carbon in the model unsupported nanoparticles are described in terms of the energy of interaction for each C addition in Figure 4.2. For each carbon addition on the surface or subsurface of the Rh nanoparticles, the energy of the carburized particle is lower than the sum of the energy of the pure Rh nanoparticle and the number of C atoms separately. This result indicates that the incorporation of carbon into the structure of unsupported Rh nanoparticles is thermodynamically favored. The energy of interaction between the C added and the nanoparticle after each C addition is approximately constant with overall average values of -8.84 ± 0.08 eV for Rh38C$_x$, -8.74 ± 0.12 eV for Rh55C$_x$, and -8.82 ± 0.23 eV for Rh68C$_x$, and showed negligible variation among the different particle sizes considered in this study. Carbon addition was conducted either on the surface only or in the subsurface only of the nanoparticles; however, it was noted that the initial position of the added C atoms was susceptible to change after relaxation. Studies on the nucleation of graphene on the (111) facet of Rh using *in situ* scanning transmission microscopy have indicated that the estimated growth rate from surface diffusion alone does not match the overall rate, and therefore another contribution, namely from C dissolved in the Rh lattice, would also provide C for the formation of graphene.[169] Growth of mono- and multi-layer graphene on a monocrystalline Rh(111) surface required temperatures of 1170 K to allow dissolution of carbon to facilitate the growth of multiple layers.[170-171] Interestingly, Auger electron spectroscopy studies on Rh(111) have indicated the potential formation of an overlayer carbide phase starting at 750 K.[172]

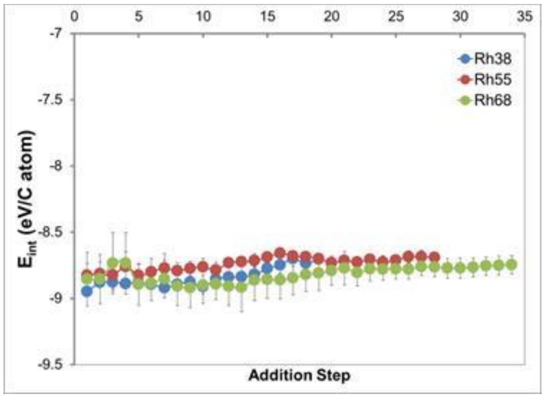

Figure 4.2 Energy of interaction for each successive addition of carbon atoms to the unsupported Rh nanoparticles of various sizes (38, 55 and 68 atoms).

Figure 4.3 shows the fraction of atoms dissolved from the total number of C added to each size of unsupported nanoparticles, which is calculated for increasing overall composition (x) of the nanoparticle (RhC_x). For the smallest particle size, C atoms tend to remain at or move to the particle surface at values of the particle C composition lower than 0.2. At higher composition, the two Rh_{38} particles seem to behave differently with one maintaining approximately 10% of its C dissolved in the subsurface for a composition range x between 0.2 and 0.4 and no carbon dissolved at $x = 0.5$. Contrastingly, the percentage of dissolved C in the other particle tends to increase and vary from 10% to 40% for C atoms initially placed in the subsurface. Distortion of the particle’s crystal lattice is observed as a result of the addition of carbon atoms is shown in Figure B.1. The structural changes in the nanoparticle may facilitate displacement of C atoms initially placed on the particle surface into the subsurface. The amount of C dissolved in those cases can reach up to 30% of the total C added. The largest particles considered here exhibit a low number of C atoms dissolved with 10% C atoms in the subsurface on average and little variation across values of overall C composition for both $C3_V$ and O_h particle structures. Particles of intermediate size consisting of 55 Rh atoms follow a different trend from other particle sizes. A higher amount of subsurface carbon remains in the particle with 62.5% C dissolved at low composition ($x = 0.15$) for the O_h particle, which further decreases to 50% at 0.27 and stabilizes at approximately 25% for $0.36 < x < 0.5$. A similar trend is observed for the I_h structure starting at a composition of 0.18 with 40% of subsurface carbon remaining dissolved, which further decreases and stabilizes at 25% for $0.27 < x < 0.5$. C atoms added on the surface of both types of Rh_{55}

particles dissolve in a lower proportion with 0 % C at low composition, rising to 20% at x = 0.18 and decreasing again to 5% at x = 0.5 for the O_h particle. In contrast, the I_h case starts dissolving carbon at x = 0.27 with 20 % C, slightly decreasing to 15 % at 0.5 composition. The different behavior observed for the particles containing 55 atoms may be attributed to their high stability and specific characteristics found in metal clusters with highly symmetric structures following series of particular sizes and geometries.[173-174] For example, Rh_{55} clusters with cuboctahedron and icosahedron structures reportedly exhibit a strong adsorption of CO than other particle geometries.[173] The composition (y) of dissolved carbon in the nanoparticle (RhC_y) subsurface, defined as the ratio of dissolved C to the number of Rh atoms, can be as high as 0.15 for the Rh_{38} nanoparticles, 0.13 for the Rh_{55} nanoparticles and 0.09 for the Rh_{68} nanoparticles. This result indicates possible variations in composition of stable subsurface carbide with particle size.

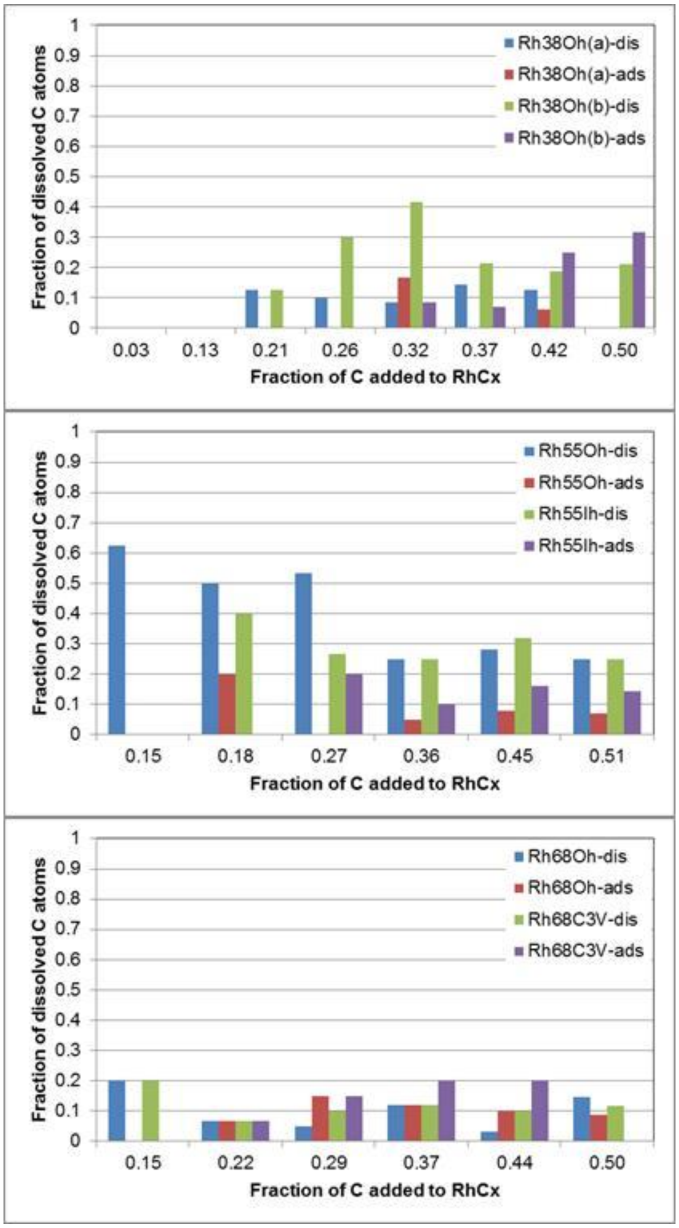

Figure 4.3 Fraction of added C atoms that dissolve or remain dissolved in the Rh particle for different overall C composition of nanoparticles with (a) 38, (b) 55 and (c) 68 Rh atoms with structures of octahedral (Oh), icosahedral (Ih) and trigonal $C3_V$ ($C3_v$) symmetry. Distinction between C atoms initially added on the surface (ads) and those dissolved in the subsurface (dis) is made.

The addition of carbon to the particles in this study proceeded until carburized particles with an overall composition of Rh_2C (or $x = 0.5$ in RhC_x) resembling a typical transition metal carbide stoichiometry were obtained. The amount of carbon added is below the saturation level of the particles' surface and insufficient to allow observation of carbon chains forming on the particle surface. Similar studies of carburization of Cu clusters have revealed early association of C atoms forming dimers, trimers and 4-membered C chains well below saturation with C.[175] This contrasting behavior between Rh and Cu may be indicative of different nucleation mechanisms with nucleation on Cu being predominantly driven by surface diffusion and Rh involving diffusion to and from the subsurface.

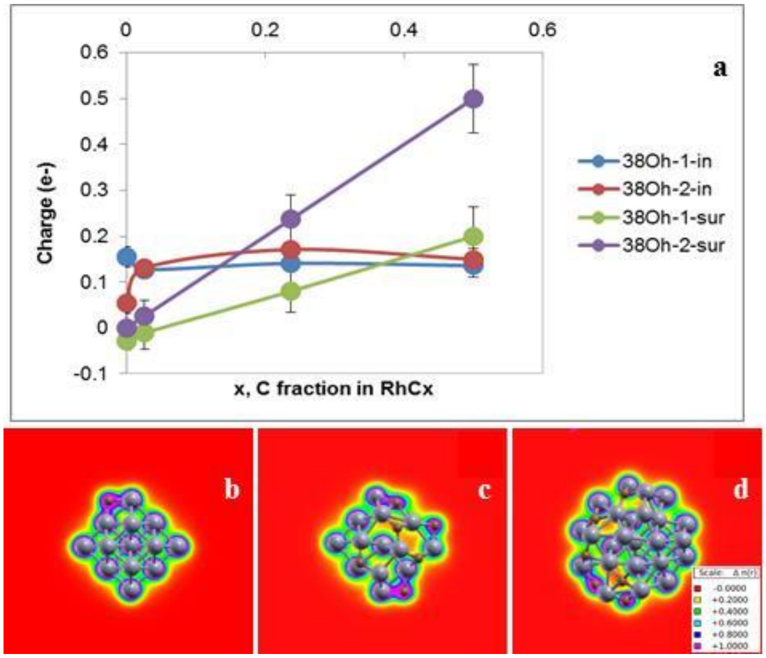

Figure 4.4 Calculated atomic charges and electron density maps in Rh_{38} particles. (a) Variation of atomic charges of Rh atoms located inside (in) and at the surface (sur) of Rh_{38} nanoparticles with increasing carbon composition. Electron density maps of unsupported Rh_{38} nanoparticles with varying overall carbon composition: (b) $RhC_{0.025}$, (c) $RhC_{0.25}$, and (d) $RhC_{0.5}$. Rh atoms are shown in grey and C atoms are shown in brown.

Changes in the atomic charges of Rh atoms were monitored as the overall C composition of the particles changed. Figure 4.4a shows the calculated atomic charges of Rh atoms located at the surface of the particle (sur) and the particle interior (in) for C composition of the RhC_x particle in the range of $0.0 < x < 0.5$. Inner Rh atoms possess average charges in the range of 0 e^- to +0.15 e^- for the range of compositions that were studied and showed little variation, which is similar to estimated atomic charges in Rh cluster reported in the literature (between + 0.05 e^- and +0.02 e^-).[160] The charges of surface Rh atoms in both pristine Rh_{38} structures ($x = 0$) tend to increase from neutral to

+0.2 e$^-$ and +0.5 e$^-$, respectively at x = 0.5, thus indicating an electron transfer from surface Rh atoms to the C atoms added. This difference in average charges between surface Rh of the two O_h Rh_{38} particles seems to be correlated with differences in the fraction of C dissolved, with the second particle having as much as a 20% to 30% higher amount of dissolved C than the first particle, as observed in Figure 4.3. The electron density maps depicted in Figures 4.4b and 4.4c show areas surrounding C atoms in the particle with a higher electron density coming from the surface Rh atoms. The 68-atom nanoparticles follow similar trends as shown in Figure B.2 with increasing average charges from 0 e- to +0.2 e- for surface Rh atoms and approximately constant neutral charge for inner Rh atoms. Surface Rh atoms in Rh_{55} show a slightly different trend with increasing average atomic charges of inner atoms up to +0.2 e- and minimal charge increase up to 0.05 e$^-$ for surface atoms. Atomic charges of carbon atoms remain almost constant at an average of -0.4 e$^-$ for different particle sizes and C composition (Figure B.2d). Charge transfer from Rh to C has been observed and reported in electronic structure studies of bonding between individual Rh and C atoms, with electrons being transferred from both the $4d^8$ and $5s^1$ orbitals of Rh.[176] Electron density maps projected on cross section planes of 55- and 68-atom particles with $RhC_{0.5}$ composition show areas of higher electron density around C atoms on the particle surface as a result of the partial electron transfer (Figure B.3).

4.4.2 Adsorption and Dissolution of Carbon in Supported Rh Nanoparticles

The energy required to add a C atom to a supported Rh_{32} nanoparticle is calculated according to eq 4.3 and shown in Figure 4.5. The calculated energy of interaction is compared among unsupported, supported on MgO(111) and supported on MgO(100) nanoparticles revealing values of energy for the different types of particles that converge with increasing C addition. The first addition of carbon to the Rh/MgO(100) nanoparticle entails on average a stronger interaction (-10.23 ± 1.75 eV/C atom) than Rh/MgO(111) (-9.41 ± 0.29 eV/ C atom) and the unsupported particle (-8.95 ± 0.01 eV/C atom). However, continued addition of carbon involves an amount of energy that converges for the three types of nanoparticles to approximately -9 eV/C atom at a composition of x = 0.5. Therefore, the presence and type of termination, either (111) or (100), of an MgO support does not seem to affect the energy of interaction between the carbon added and the Rh nanoparticle.

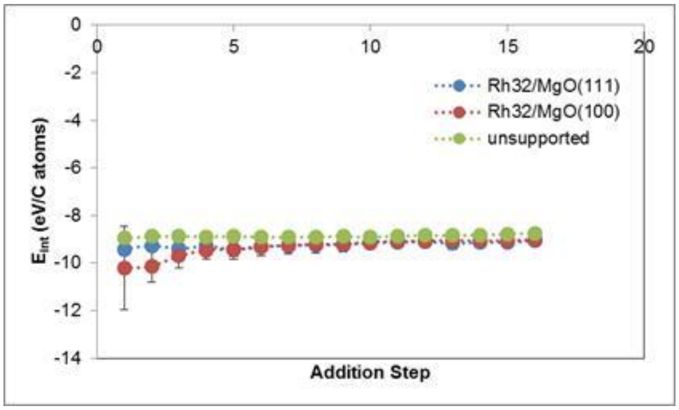

Figure 4.5 Energy of interaction for each successive addition of carbon atoms to the Rh_{32} nanoparticles supported on the (111) and (100) facets of MgO *versus* the unsupported case.

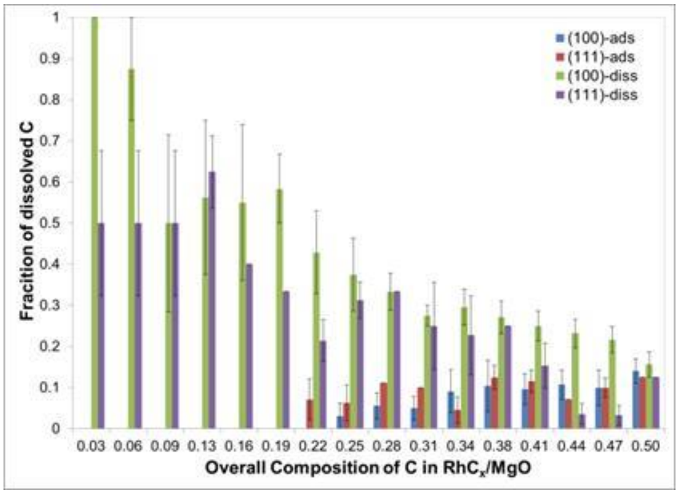

Figure 4.6 Variation of the fraction of the total number of C added that remain or become dissolved in the supported Rh nanoparticle with C overall composition. Distinction between the support termination, either (100) or (111), and initial location of each newly added C adsorbed on the surface (ads) or dissolved in the subsurface (dis).

Despite the similar energy associated with each C addition initially on the surface or subsurface, it is important to consider the location of carbon after relaxation. Figure 4.6 shows the fraction of carbon atoms that stay in or move into the subsurface after relaxation of the initial position as a function of the overall composition of the particle (x). The initial addition of carbon into the nanoparticle supported on MgO(100) remains dissolved in a high proportion (> 87 %) for x < 0.09, in contrast with the nanoparticle supported on MgO(111) which retains approximately 50% of C dissolved in the subsurface for x < 0.19. At C composition higher than 0.19, a steady decrease in the percentage of dissolved C atoms is observed for nanoparticles supported on both (100) and (111) facets of MgO, while a small amount of C begins to dissolve in the subsurface of particles with adsorbed C. These trends lead to a convergence at x = 0.5 among the different particles to approximately 15 % of the total C added staying dissolved or dissolving into the particle subsurface. The overall composition of carbon located inside the particle (y), described as the fraction of dissolved C with respect to the number of Rh atoms in the supported particles (RhC_y/MgO), does not exceed 0.10 and has a value of approximately y = 0.08 at the convergence point (x = 0.5). These composition values indicate a lower capacity of the supported Rh nanoparticles to dissolve C compared to unsupported particles of a similar size. For example, unsupported Rh_{38} particles reach a maximum value of y = 0.15 as discussed in the previous section.

4.4.3 Adhesion of Rh Nanoparticles on MgO During C Addition

The energy of adhesion of the Rh nanoparticle to the MgO support was estimated according to equation 3 for each C addition step as shown in Figure 4.7. The location of the carbon added to the nanoparticle (*i.e.* on the surface or in the subsurface) did not seem to affect the adhesion energy, and therefore distinction of initial C location is not shown. Instead, the effect of the relative orientation of the particle on the support was considered as a factor potentially affecting how strongly the particle interacts with the support. Two initial configurations of Rh deposited on the (100) and (111) facets of an MgO support with different degrees of lattice matching between the particle and the support were considered. The first configuration has a higher degree of epitaxial matching than the second configuration, and they are labeled as ‘1’ and ‘2’, respectively. The degree of lattice match was calculated by dividing the number or Rh atoms matching the MgO lattice divided by the total number of Rh in the layer in contact with the support. This ratio was determined after structural relaxation upon each C addition, and it is shown in Figure B.4. The presence of C atoms near the nanoparticle-support interface as a factor that may also influence the interaction between the two surfaces is monitored and showed in Figure B.5.

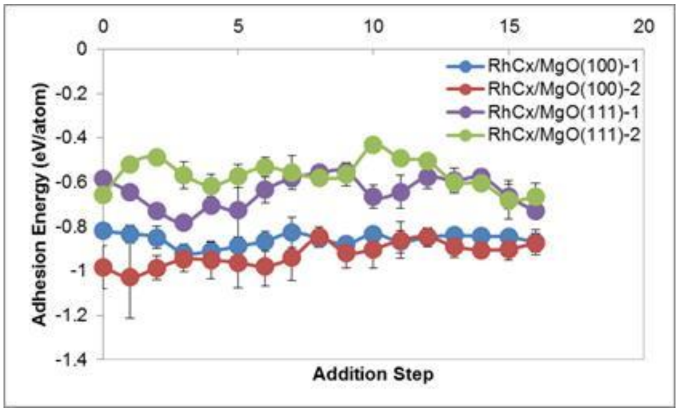

Figure 4.7 Energy of adhesion of Rh nanoparticles to an MgO support with facets (100) and (111) per Rh atom at the interface for two initial configurations of the nanoparticle with respect to each support facet with a high (or intermediate) and a low degree of lattice match labeled as ‘1’ and ‘2’, respectively.

The adhesion of the nanoparticle to the support in the absence of C atoms shows a stronger interaction for the particle with the lower degree of lattice match on the MgO(100) support with 1 eV per Rh atom at the interface, followed by the lattice-matched particle supported on MgO(100) with 0.8 eV per Rh atom. Particles supported on the MgO(111) facet show a weaker interaction of approximately 0.6 eV per Rh atom at the interface for the different relative configurations on the support. The overall trends indicate a negligible effect of the individual addition of C atoms to the particle and the initial particle-support relative position in the energy of adhesion. For example, the energy of the nanoparticles supported on MgO(100) varies between -0.8 eV/Rh and -1 eV/Rh as C addition progresses and finally converges to 0.87 eV/Rh. A similar behavior is observed for the particles supported on MgO(111) with small fluctuations between -0.4 and -0.9 eV/Rh converging at 0.7 eV/Rh. Previous DFT studies of the adhesion Co_2C nanoparticles supported on MgO(100) show slightly stronger adhesion energy in the range of -0.9 to -1.5 eV per metal atom. The interface in most cases was characterized by a majority of Co atoms atop O atoms of the support, matching the substrate lattice.[177] In the present work, the percentage of Rh atoms matching the MgO(100) lattice tends to increase as the structure of the nanoparticle is allowed to relax after each C addition with over 65 % of interfacial Rh atoms located atop O atoms (Figure B.4). In contrast, particles supported on MgO(111) tend to decrease the degree of lattice match below 40 % in most cases as carbon content increases. One exception is the particle labeled as RhC_x/MgO(111)-2 with a degree of lattice match that undergoes a gradual increase from the 11th C addition with 50 % reaching up to 65 – 70 % at the 15th addition on the particle's surface. This result coincides with another gradual increase in the number of C located near the particle-support interface as shown in Figure B.5. Despite those C atoms not being directly in contact with the support, they seem to affect the Rh lattice and contribute to increase the degree of epitaxial match in MgO(111)-supported particles. Other particles with C atoms added on the surface contain from 0 to 2 C atoms near the interface (or 0 – 12 % of the total C added), whereas particles with C added in the subsurface contained nearly 30 % of the C atoms relaxed to positions near the interface from the 5th C addition onwards for the epitaxial configuration, and under 12 % for the non-epitaxial configuration. Overall, the small number of C near the interface and the even smaller number of dissolved C as well as the degree of lattice match do not seem to exert a significant influence on the energy of adhesion normalized by the number of Rh atoms at the interface. However, changes on the surface termination and functionalization of the support, as demonstrated by the different values of adhesion energies involved in adsorption on the (100) facet terminated in Mg and O atoms and the (111) facet terminated in $(OH)^-$ groups, and the local composition of carbon at the interface seem to indicate an opportunity to modify the type and strength of interactions of the metal nanoparticle and the metal oxide support. In comparison, changes occurring at the interface such as the composition of carbon near the interface in MgO(100)-supported Co_2C, which can easily migrate in the nanoparticle and create a gradient, are observed to affect the strength of interaction and the number of Co atoms at the interface.[177]

Table 4.1 Average distance between the particle atoms (Rh and C) located at the particle's first layer (in contact with the surface) and the surface of the MgO support for pure metal and carburized supported Rh_{32} nanoparticles.

	Rh-support dist. (Å)	**C-support dist. (Å)**
Rh/MgO(111)	2.41	-
Rh/MgO(100)	2.15	-
Rh_2C/MgO(111)	2.22	3.54
Rh_2C/MgO(100)	1.94	2.94

Rh atoms in the nanoparticles remain organized in layers after structural relaxations between consecutive C additions. The bottom or first layer in contact with the surface consists of Rh atoms separated from the MgO support by an average distance that decreases with the incorporation of C in the nanoparticle as outlined in Table 4.1. On average, there is a greater distance separating Rh atoms from the (111) surface facet than the (100) surface facet of MgO with 2.41 Å for the pure Rh nanoparticle on MgO(111) decreasing to 2.22 Å for the carburized Rh_2C nanoparticle. In contrast, those supported on MgO(100) are separated by a distance of 2.15 Å for the pure Rh particle and 1.94 Å for the carburized Rh_2C particle. The closest location of C atoms to the support is between the first and second Rh layer at an average distance of 3.54 Å and 2.94 Å from the (111) and (100) surface facets of MgO, respectively. These results indicate that the termination of the support is an important factor affecting the deposition of the nanoparticle on the support. In addition, the structural changes in the nanoparticle support-distance and the accommodation of the particle lattice to the support, as C atoms are added, seem to lead to low-energy configurations with similar values of adhesion energy as described in Figure 4.7.

4.4.4 Electron Distribution at the Particle-Support Interface

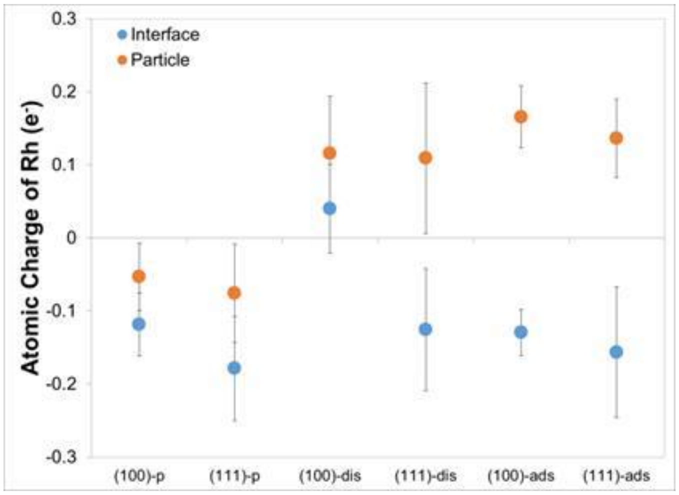

Figure 4.8 Average atomic charges for Rh atoms located near the nanoparticle-support interface (labeled as 'Interface') and elsewhere in the nanoparticle (labeled as 'Particle'). In order from left to right, each set of values corresponds to: pure Rh nanoparticles supported on MgO(100), pure Rh on MgO(111), $RhC_{0.5}$ on MgO(100) with carbon initially dissolved in the particle, $RhC_{0.5}$ on MgO(111) with carbon initially dissolved in the particle, $RhC_{0.5}$ on MgO(100) with carbon initially adsorbed in the particle, and $RhC_{0.5}$ on MgO(111) with carbon initially adsorbed in the particle.

The atomic charges of the Rh atoms in supported Rh nanoparticles were estimated using the Bader charge analysis and are shown in Figure 4.8, making distinction between Rh atoms near the interface with the support and elsewhere in the nanoparticle. Overall, Rh atoms located at the interface tend to have slightly negative charges whereas Rh atoms at other locations in the particle tend to have positive or close to neutral charges. Previous estimations of Rh atomic charges in 13- and 55- atom clusters using DFT have reportedly shown Rh with approximately neutral charges and slightly negative atoms depending on the coordination number.[160] For the pure particle supported on MgO(111), Rh atoms near the interface have an average negative charge of -0.17 e^- and -0.12 e^- when supported on MgO(100), while other Rh atoms in those particles virtually possess neutral charges (less than |-0.07| e^-). Rh in the carburized particles (Rh_2C) mostly maintains an average negative charge of -0.15 e^- at the interface and between +0.1 e^- and +0.15 e^- elsewhere in the particle due to the interactions and partial electron transfer to the added C atoms, which bear on average a charge of +0.4 e^-. The exceptions to this description are the carburized particles supported on MgO(100) with interfacial Rh atoms having slightly positive average charges (+ 0.05 e^-) instead of negative charges. Some of the aspects that may contribute to a different behavior in these particles are the almost perfect lattice match (~100%) as shown in Figures B.4b and B.7, and the relatively high number of dissolved carbon located near the interface after relaxation ~25-30 % of the total C added, in comparison with other particles (Figure B.5b). Changes in the nature of the interactions between the Rh nanoparticles and the support, such as the distribution of charges in Rh atoms at the different nanoparticle layers, may be influenced by structural features such as the degree of epitaxial match and the concentration of C atoms near the interface. Systematic studies of the interactions between nanostructured metal overlayers and oxide support surfaces[163] have identified two main aspects that determine the nature of the interactions, which are also noted here: 1) the interfacial charge redistribution, as observed in the current supported Rh depicted in Figure 4.9; and 2) atom transfer at the interface, which can manifest as rearrangement of the particle atoms at the interface to match or mismatch the support lattice, as discussed here and illustrated in Figure B.4, B.5, B.6, and B.7, or as diffusion of defects reported from experiments.[163] This offers possibility to control the catalyst structure and properties by seeking to alter the interface with the support.

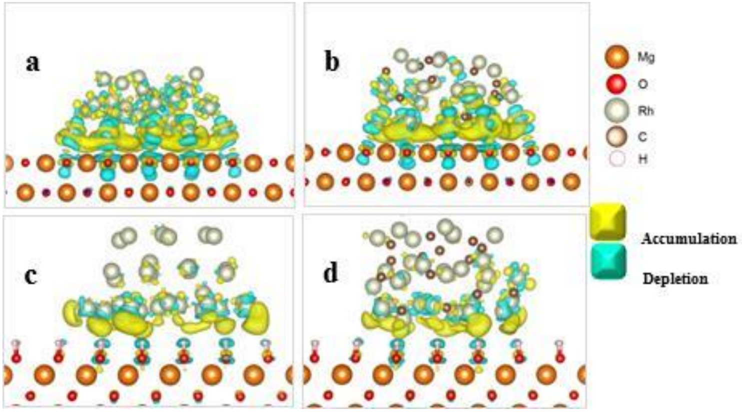

Figure 4.9 Regions of electron accumulation (yellow) and depletion (blue) at the particle-support interface of (a) Rh/MgO(100), (b) $RhC_{0.5}$/Mg(100), (c) Rh/MgO(111), and (d) $RhC_{0.5}$/MgO(111). Isovalue used: 0.03 $e^{-}/Å^{3}$.

Electronic density transfer as a result of the interactions between the pure and carburized particle and the (100) and (111) facets of the MgO support is described in terms of: a) electron accumulation regions and b) electron depletion regions, both of which can be identified in isosurfaces of electron density plotted according to electrostatic potentials. Figure 4.9a illustrates the pure nanoparticle supported on MgO(100) with regions of electron density accumulation mainly located at the particle-support interface in a delocalized manner and spread across the interface. Electron accumulation also occurs to a smaller extent on the surface Rh atoms while small regions of electron depletion are observed between the particle’s Rh layers. This double accumulation-depletion effect surrounding the Rh atoms outside of the interface produces on average neutrally charged Rh atoms while Rh at the interface remains slightly negative (Figure 4.8). More noticeably, electrons are depleted from the vicinity of O and Mg atoms in the MgO top layer and its neighboring layer, resulting in localized depletion regions as depicted in Figure 4.9a. Similarly, the regions of electron density accumulation in the carburized particle supported on MgO(100) can be found at the particle-support interface (Figure 4.9b), where electron density is transferred from regions of depletion between the interfacial Rh layer (1st layer) and its neighboring Rh layer (2nd layer), and between O and Mg atoms of the interfacial layer and subsequent layer of the MgO support. The main difference between the pure metal and carburized nanoparticle is the number of the Rh atoms involved in the particle support interaction. In the first case, Rh atoms in the topmost layer (farthest from the support) exhibit small regions of accumulation and depletion, whereas for the second case the same Rh atoms lack electron transfer induced by interactions with the support. Nevertheless, interactions between surface Rh and adsorbed (or dissolved) C occur, thus giving place to electron transfer between Rh and C. This results in slightly positive Rh atoms (+0.1 to +0.15 e^-), as shown in Figure 4.8, and C atoms bearing average negative charges of -0.4 e^-.

The Rh nanoparticles supported on MgO(111) exhibit regions of accumulation and depletion that correspond to those observed on the MgO(100) supported particles (Figures 4.9c and 4.9d), however some differences can be noted: 1) the electron density transfer effect is more confined to the interface between the particle and the support, which is in contrast with the (100)-supported particles where adjacent layers in the particle and support are also involved. 2) Regions of electron density accumulation are more localized appearing as small lobes directly below Rh atoms at the interface in comparison with the (100)-supported particles, in which accumulation regions are more spread across the interface. 3) Regions of depletion of electron density from the support are smaller and more localized in the close vicinity of the $(OH)^-$ groups of the MgO(111) support. Finally, the distribution of electron density accumulation and depletion regions due to electron transfer between the nanoparticle and the MgO(111) support appears to be unaffected by the presence of carbon dissolved in (or adsorbed on) the Rh nanoparticle.

4.4.5 Adhesion of Graphene on Supported Rh Nanoparticles

The interactions between a graphene seed, representing a nascent carbon nanotube, and an Rh nanoparticle supported on MgO are examined using a flat graphene fragment brought in contact with the supported particle models described in the previous section at an initial distance of 2.4 Å. For this purpose, supported particles with C compositions corresponding to pure Rh and Rh_2C deposited on both surface terminations of MgO (100) and (111) were selected. The adhesion energy of the graphene seed to the nanoparticle surface and the adhesion energy of the particle to the support are calculated according to eqs 3 and 4, respectively, and summarized in Table 4.2.

Table 4.2 Average adhesion energy between a graphene fragment and the supported pure metal or carburized particle and the average adhesion energy between the particle and the (111) or (100) facets of the MgO support with and without graphene.

Adhesion energy:	g-cluster (eV)	cluster-support (eV)	
		with graphene	without graphene
graph/Rh/MgO(111)	-19.12	-7.72	-9.61
graph/Rh/MgO(100)	-15.44	-7.92	-9.80
graph/Rh_2C/MgO(111)	-18.77	-8.61	-9.00
graph/Rh_2C/MgO(100)	-9.77	-9.35	-10.24

Graphene adheres more strongly on the particles supported on the (111) facet of MgO than on the MgO(100)-supported particles, with -19.12 eV for the pure Rh particle supported on MgO(111) and -15.44 eV for that supported on MgO(100). This observation can be related back to the effect of the support termination on the electron transfer described in Figure 4.9. The accumulation and depletion of electron density in the particle due to the interactions with the MgO(111) support involves almost exclusively Rh atoms located the interface, whereas most Rh atoms in the MgO(100)-supported particle are involved in the electron transfer process. This contrasting behavior may be an indicator of the effect that changes in the electronic structure, caused by different support terminations, can have on the particle's interaction with the nascent nanotube structure.

The calculated adhesion of graphene to the MgO(111)-supported carburized particles shows a weaker interaction than the MgO(111)-supported pure metal particles with a net energy difference of 0.35 eV. Similar effects have been reported when comparing the interactions of graphene to carburized Co surfaces and pure metal C surfaces, showing a weaker adsorption of graphene for the carburized surface than the pure metal surface.[121] The adhesion of graphene on the MgO(100)-supported carburized particles shows a significant drop when compared with the pure metal particle with a difference of 5.67 eV. Images of the relaxed structures of graphene adsorbed on the supported particle shown in Figure B.8 also provide evidence of a different behavior of the carburized particle deposited on Mg(100). The initially flat structure of the graphene fragments gets distorted after structural relaxation, as indicated by changes in the sheet's curvature and distance from the particle surface. Graphene fragments adsorbed on the surface of both pure metal and carburized particles supported on MgO(111) exhibit curved edges that accommodate to the curvature of the particles (Figures B.8c and B.8d). Such changes allow C atoms in graphene to remain at an average equilibrium distance of 2.02 Å from the pure Rh particle and 2.11 Å from the carburized particle. In a similar manner, graphene adhered on the surface of the pure Rh supported on MgO(100) has curved edges matching the particle's curvature (Figure B.8a) separated by an average distance of 2.02 Å. However, the graphene adsorbed on the carburized particle supported on MgO(100), with a lower adhesion energy of -9.77 eV, remains flat with edges that seem to detach from the particle surface (3.06 Å) after relaxation instead of curving to adopt the shape of the particle. This result may be correlated with other features that the

Rh_2C/MgO(100) nanoparticles have shown to differ from other supported particles. For example, interfacial Rh atoms in this case are slightly positive whereas negative values are observed in other particles (Figure 4.8); also, a higher degree of lattice match and high composition of carbon at the interface are observed than for other particles (Figures B.4b and B.5b). These factors were observed to affect the extent of the electron transfer between the support and the nanoparticle (Figure 4.9), and in turn may affect how the supported nanoparticle interacts with the nucleating nanotube. Furthermore, the adhesion energy of the particle to the support decreases as a result of graphene adhering onto the nanoparticle as described in Table 4.2. Due to the absence of structural changes in the particle at the interface with the support in the presence of graphene, the weaker particle-support adhesion energy may be attributed to changes in the electronic structure of the particle induced by the particle-graphene interactions.

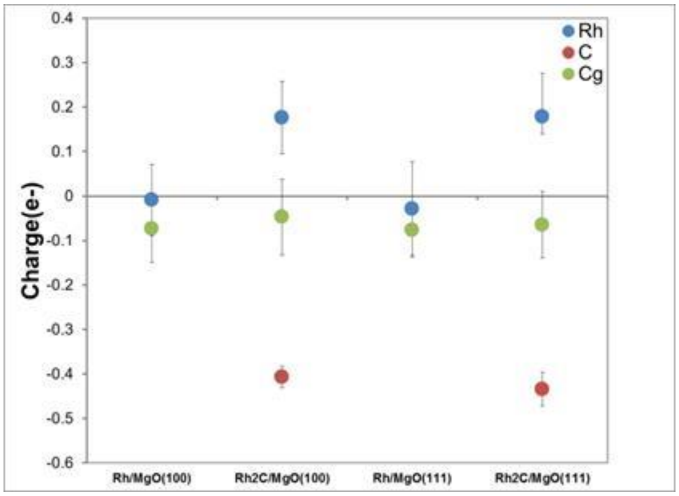

Figure 4.10 Atomic charges for Rh, C added to the particle (C), C from graphene fragment (Cg) for pure Rh nanoparticles and carburized Rh_2C nanoparticles supported on the (100) and (111) facets of MgO.

Additional information about the interactions between graphene and the supported nanoparticles can be obtained from the analysis of atomic charges. Figure 4.10 shows the calculated atomic charges for Rh atoms, individual carbon atoms added to the nanoparticle (C), and carbon atoms belonging to the graphene fragment (Cg). The nanoparticles considered include pure Rh and carburized Rh_2C nanoparticles supported on the (100) and (111) facets of MgO. Rh and Cg atoms in the pure Rh particles adsorbed on either support are virtually neutral with Cg having on average less than -0.1 e^- and Rh having approximately -0.01 e^-. Charge transfer between the supported pure Rh nanoparticle and the graphene fragment can thus be considered negligible. Conversely, Rh atoms in the carburized nanoparticles attached to either support possess a positive charge (+ 0.2 e^-) as a result of their interactions with the individual C atoms added to the particle. Those C atoms bear the same charge (-0.4 e^-) as individual C atoms in unsupported nanoparticles and supported nanoparticles without graphene, thus indicating that external interactions of the particle do not affect charge transfer between Rh and the individual C atoms added. Cg atoms, on the other hand, maintain an average charge lower than 0.1 e- with or without C in the particle. In all the particles considered, regions of accumulation and depletion of electron density due to interactions of the particle with graphene appear to be uniformly distributed around rhodium and carbon atoms (Figure B.9). Pure metal Rh and carburized Rh exhibit similar patterns of electron accumulation and depletion regions, contrasting with the significant differences in size of those regions observed for pure metal and carburized Ni nanoparticles in previous studies.[178] Instead, the size of the regions at the graphene-Rh interface is greater in comparison with regions located elsewhere in both metal and carburized particles. Nevertheless, the uniformity of their distribution creates an interaction that does not involve a net electron density transfer between graphene and the supported particle.

4.5 Conclusions

We studied the interactions between catalytic Rh nanoparticles and carbon in various forms, as individual C atoms sequentially adsorbed or dissolved and as a nucleating graphene seed, in the context of the early stages of nucleation and growth of single-walled carbon nanotubes using density functional theory. The sequential adsorption of C atoms on both unsupported and supported nanoparticles is observed to be energetically favorable. The energy of interaction between the added carbon and the Rh particle after each addition is constant and independent of the particle size and geometry for the unsupported particle, and unaffected by the MgO support surface termination for the supported particles. Dissolution of C is observed to occur in the subsurface of the nanoparticles, with a limited solubility that decreases with increasing particle size and due to the particle interaction with the support. The initial crystalline structure of the unsupported Rh nanoparticles gets distorted as C atoms are added. In contrast, the supported particles maintain a layered structure that tends to match the support lattice epitaxially for the MgO(100) support and non-epitaxially for the MgO(111) support. Adsorption and dissolution of C in the unsupported Rh nanoparticles involve partial charge transfer from outer Rh atoms of the nanoparticle to C while the inner Rh atoms remain neutral. Electron transfer in the supported cases also occurs between Rh and C and at the interface between Rh and the support. Electron accumulation at the particle-support interface makes interfacial Rh atoms appear to have a slightly negative charge, while Rh atoms located elsewhere show electron deficiency as a result of the interactions with adsorbed and dissolved C. The adhesion energy of each Rh atom to the MgO support is stronger for the Mg- and O- terminated (100) surface facet than for the $(OH)^-$ terminated (111) facet. Furthermore, factors such as amount of carbon near the interface, type or surface termination of the support, and the degree of particle-support epitaxial match were found to influence the extent of the charge transfer and the overall particle-support adhesion. Finally, the adhesion of a graphene seed to the supported nanoparticles is stronger for particles without C dissolved and supported on the hydroxylated MgO(111). On the other hand, the overall energy of adhesion of the Rh nanoparticle to the support tends to decrease when the seed is nucleating on its surface and increase when C is present in its structure. These results demonstrate that the interactions between a nucleating nanotube and the catalytic nanoparticle can be influenced by modifying the particle-support interface and seeking conditions to change the carbon solubility of the nanoparticle. Further exploration and elucidation of such relationships has the potential to help advance the development of strategies to use the catalyst structure to define the nanotube structure.

CHAPTER V

NUCLEATION OF GRAPHENE AND ITS CONVERSION TO SINGLE WALLED CARBON NANOTUBES[*]

5.1 Summary

We use an environmental transmission electron microscope to record atomic-scale movies showing how carbon atoms assemble together on a catalyst nanoparticle to form a graphene sheet that progressively lifts-off to convert into a nanotube. Time-resolved observations combined with theoretical calculations confirm that some nanoparticle facets act like a vice-grip for graphene, offering anchoring sites, while other facets allow the graphene to lift-off, which is the essential step to convert into a nanotube.

5.2 Introduction

Single-walled carbon nanotubes (SWCNTs) continue to be one of the most desirable materials for nanotechnology device integration.[2] For example SWCNTs exhibit high on/off current ratios, large charge carrier mobilities and high current carrying capacity making them ideally suitable for making nanoscale transistors.[179-180] Yet limited SWCNTs based technologies have emerged on the market because of the lack of control on the structure of SWCNTs, *i.e.*, diameter, defect density, length and chiral angle. During SWCNTs growth, the nucleation step, which sets the stage for the addition of

---

[*] Reprinted with permission from "Nucleation of Graphene and its Conversion to Single-Walled Carbon Nanotubes" by M. Picher, P. A. Linn, J. L. Gomez-Ballesteros, P. B. Balbuena, and R. Sharma, 2014. *Nano Letters*. 14, 6104-6108, Copyright 2014 by The American Chemical Society.

subsequent atomic building blocks, is crucial because the precise arrangement of carbon atoms controls their opto-electronic properties.[100] Theoretical simulations have shown that during carbon nanotube synthesis by catalytic chemical vapor deposition (C-CVD), the carbon precursor is decomposed on the catalyst surface generating carbon atoms that assemble first into a graphene nucleus *via* sp^2 hybridization.[181] The graphene nucleus then propagates on the catalyst nanoparticle surface and progressively wraps around the nanoparticle surface converting into a hemispherical cap *via* incorporation of carbon pentagons in the initial honeycomb structure.[35-36, 182] The structure of the cap at the time of its lift-off determines the chirality of the SWCNT, which should remain the same as more carbon atoms are added to the tubular structure, as long as the thermodynamic conditions do not change.[183-184]Although these simulations provide a fundamental framework for nanotube growth,[185-187] they lack connectivity to experimental growth conditions. For example, most of the simulations are performed on a free-standing catalyst particle, ignoring the catalyst-support interactions, and at a significantly higher temperature compared to the typical C-CVD experimental conditions. Moreover, *in situ* atomic scale observations have elucidated some salient features of carbon nanotube growth that were in direct conflict with theoretical predictions, *e.g.* nanotubes grow from solid particles,[188-189] the structure of catalyst particle can be metal carbide.[50, 190] Therefore direct atomic scale observations are needed to elucidate the nucleation and growth process of single walled carbon nanotubes under growth conditions.

5.3 Methodology

5.3.1 High Resolution ESTEM

We employ an environmental scanning transmission electron microscope operated at 300 KV, equipped with an image corrector and a charge coupled digital (CCD) camera. Co-Mo/MgO catalyst powder was provided by Prof. Zafar.[191] A drop of catalyst suspension in isopropanol was deposited on a SiC membrane heating chip. The sample was loaded in the microscope and heated to 750 ºC in 10 Pa of O_2. After 15 min, the sample was cooled to room temperature and O_2 flow was terminated. The sample was then heated to 625 ºC and 0.005 Pa of C_2H_2 was introduced. The videos were recorded at a frame rate of 6 s^{-1} at an electron dose of 10^5 nm^2s^{-1} which was not found to significantly affect the growth process, as the same carbon nanotube structures formed in the regions exposed and unexposed by the electron beam.

5.3.2 DFT Calculations

The work of adhesion for the Co carbide surfaces was obtained through density functional theory (DFT) calculations using the Vienna *ab initio* simulation package, VASP [81, 124, 129] with the projector augmented wave (PAW) pseudopotential for the core electrons, plane-wave basis set with a cutoff energy of 400 eV for the valence electrons.

The surfaces were obtained by cleaving the initial structure of the carbide [192] along the planes (020) and (210) using Materials Studio [17]. Four slabs were generated, two with Co or C terminated (020) surfaces and other two with Co or Co-C terminated (210) surfaces. Each of them was composed of 36 Co atoms and 18 C atoms maintaining the stoichiometric ratio Co_2C. The atoms were distributed in six layers, of which the two bottom ones were fixed to simulate the bulk whereas the surface layers were allowed to relax. The dimensions of the simulation cells were 0.9 nm x 0.9 nm x 1.8 nm for the (020) surface and were 0.9 nm x 1.0 nm x 1.8 nm for the (210) surface. Periodic boundary conditions were applied in the x, y, and z directions to resemble an infinitely long slab in the x and y directions but separated from its periodic image in the z-direction by a 1.3 nm vacuum gap. Graphene was modeled as a non-periodic fragment containing five hexagonal rings, so that the lattice could freely accommodate itself to the carbide surface. The graphene fragment has dangling bonds at its rim. Each structure was optimized separately using a conjugate-gradient algorithm to relax the atoms to their ground state. After convergence the graphene was placed on top of each surface at a distance of 0.245 nm and optimized for structural relaxation. The convergence criteria for the electronic self-consistent loop was set to be 10^{-4} eV and for atomic relaxation 10^{-3} eV. The work of adhesion is the energy per unit area necessary to bring two free surfaces into contact. We estimated the work of adhesion from the following relation [92]. The free energies of the individual systems Co_2C and graphene were subtracted from the energy of the combined system and divided by the contact area (eq 5.1).

$$W_{adh} = \frac{E_{Co_2C+g} - \left(E_{Co_2C} + E_g\right)}{A} \tag{5.1}$$

5.3.3 Structure Identification Method

High resolution images (Figure C.1a) were obtained for structural analysis using fast Fourier transformation (FFT or digital diffractogram) (Figure C.1b). Measured d-spacing and angles were matched with known phases containing Co, O, Mg, and C using a software, called CrystalSphere, developed at NIST. The structures of known phases were retrieved from JCPDS files available at http://www-i.ncnr.nist.gov/icsd/. In the first step, the program uses these files to match all measured d-spacing to the same phase within a specified error and identifies the crystal planes (Table S1). After that, the measured angles between the planes, selected in the first step, are matched. In the final step, a zone axis is assigned. A structure match is assigned only if all (two or more) measured d-spacing, the angles between them, and a common zone axis are matched to a known phase. The structure was further confirmed by matching FFT with a calculated diffraction pattern of the assigned phase (Figure C.1c Since 1nm to 3 nm nanoparticles have been reported to have lattice expansion or contraction owing to its high surface to volume ratio [193], the tolerance error for d-spacing is ≈6 %, and the plane angle is ≈10 %.). A number of other particles, active for CNT growth (Figure B.2) were also measured to ensure the structure identification as the structures of Co_3C and Co_2C are very similar and undistinguishable in certain orientations. Results are given in Table S2. It is interesting to note that the FFTs could sometimes be indexed for both structures but the errors for Co_2C are lower than for Co_3C, within the expected measurement constraints for small particles (*e.g.* particle 5 and 6). Based on our detailed analysis the structure of active particles was assigned to be Co_2C and a crystal structure model was built based on the FFT analysis result to identify the surface planes and their structure that defines the nanoparticle geometry (Figure B.3).

5.4 Results and Discussion

5.4.1 Nucleation of Graphene on Cobalt Carbide Surfaces

The main challenge for direct imaging of nucleation is that it involves a small number of atoms and a short time scale, and thereby requires a combination of high spatial and temporal resolution. We have overcome this constraint by reducing the growth rate to harmonize with the temporal resolution of our recording media. We have employed an environmental scanning transmission electron microscope (ESTEM),[194] equipped with an image corrector and a digital video recording system, to follow SWCNT growth using a low pressure of acetylene (C_2H_2) as the carbon source and a Co-Mo/MgO catalyst (Materials and Methods in Appendix C). Figure 5.1 shows time resolved high resolution images extracted from a video recorded at a frame rate of 6 s^{-1} at 625 °C in 0.005 Pa of C_2H_2. A number of nanoparticles, ranging from 1 nm to 2.5 nm in size, oriented along low index zone axes on MgO are visible within a recorded 20 nm x 20 nm area. Most of these nanoparticles were active for nanotube. Two-dimensional lattice resolution in most of the particles, marked as P1 and P2 in Figure 5.1 and P3, P4, P5 and P6 in Appendix C, Figure C.1, is maintained throughout the observation period of 104 s. At the start of our video recording (Time = 0 s) the structures of P1 and P2 were Co_3C and CoO, respectively, as determined from the Fast Fourier transforms (FFT) of the images (Figure C.2 in Appendix C). After 58 s, P1 converted into Co_2C, a carbon richer phase and P2 converted into Co_3C (Figure 5.1b).[192] This transition of metal oxide to metal carbide indicates that P1 may have converted to Co_3C before we started recording the video. In general all nanoparticles converted to Co_2C structure before nanotube nucleation. Iron carbide formation during carbon nanotube growth has been previously observed,[50, 190] but similar direct evidence for cobalt carbide had not been reported. A number of other particles, active for CNT growth (Figure C.1 and Table C.2) were also measured to ensure the structure identification of active particles as the structures of Co_3C and Co_2C are very similar and undistinguishable in certain orientations. These measurements confirmed Co_2C structure as the active phase for nanotube nucleation here.

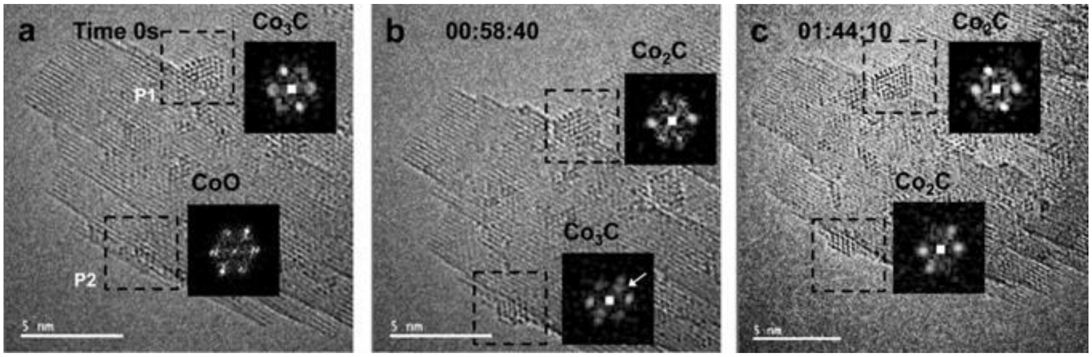

Figure 5.1 Structural transformation of catalyst nanoparticles after C_2H_2 introduction. (a, b, c) A series of high resolution images extracted from a digital video recorded after introducing 0.005 Pa C_2H_2 at 625 °C. FFTs from the particles P1 and P2 regions (insets) are used for structure identification. Structure of P1 converted from Co_3C (a) to Co_2C (b) while P2 changed from CoO (a) to Co_3C (b) and then to Co_2C (c) before nucleating SWCNTs. The white arrow in FFT of particle P2 indicates the contribution from MgO support. Scale bars are 5 nm.

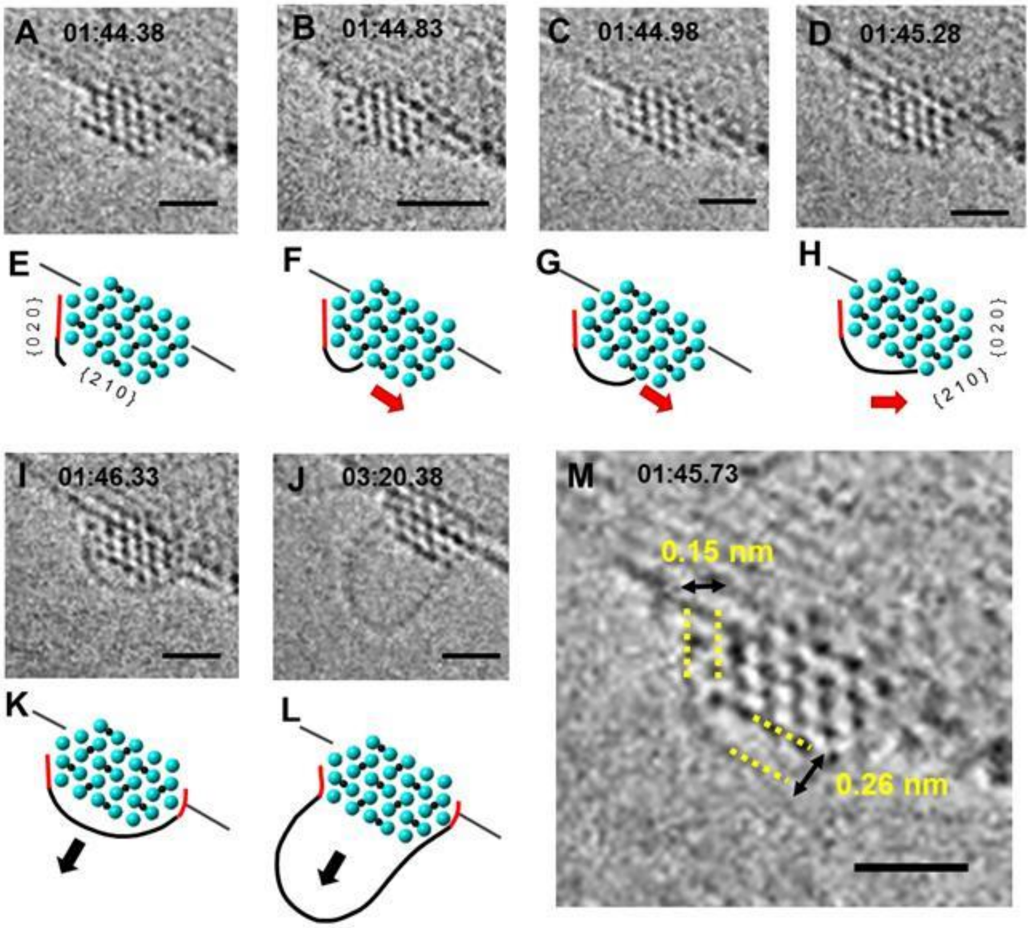

Figure 5.2 *In situ* time-resolved ETEM observation of SWNT nucleation and growth. (a, b, c, d) (i) (j) A series of images extracted from a digital video of a Co_2C nanoparticle showing SWCNT growth. (e, f, g, h) (k) (l) Corresponding atomic models. The active surfaces of the catalyst are identified to be (020)c and (210). The red lines indicate the stronger adhesion between graphene and metal on the two $Co_2C_{(020)}$ surfaces and black line shows slightly lifted graphene from (210) surface that results in the formation of cap and growing SWCNT. The arrows are guiding the growth directions. (m) Snapshot showing the average distances between the growing structure and the (020) and (210) catalyst surfaces before the nanotube lift-off. Scale bars are 1 nm.

Although the nominal composition of the catalyst contains Mo[20] which was confirmed by energy dispersive x-ray analysis and electron energy-loss spectroscopy of large catalyst/support areas but we did not find any Mo in active catalyst particles. Therefore we do not have direct experimental evidence to decipher the exact role of Mo for SWCNT growth.

Higher magnification images of nanoparticle marked as P2 in Figure 5.1 are shown in Figure 5.2. The Co_2C nanoparticle is orientated along the zone axis and is bound by (020) and (210) planes in projection (Figure 5.2a and 5.2e). We first observe a graphene embryo to nucleate on the corner of $Co_2C_{(020)}$ and $Co_2C_{(210)}$ surfaces (Figure 5.2a) and spread over the $Co_2C_{(210)}$ surface during the growth (Figure 5.2b). The observed bending of the growing graphene is proposed to be stabilized by the insertion of pentagons,[134] which is the first step in forming the hemispherical cap. The graphene is in close contact with $Co_2C_{(020)}$ surface but is slightly lifted from $Co_2C_{(210)}$ which is confirmed by the average measured distances of (0.15 ± 0.01) nm[*] and (0.26 ± 0.01) nm[*] (Figure 5.2m). With its left side anchored to the $Co_2C_{(020)}$ surface, the lateral expansion occurs *via* atomic scale jumps of its right edge on $Co_2C_{(210)}$ (Figures 5.2b-d, f-h). This expansion of tube diameter may also be favored by the reduction of the curvature energy.[195] Once the graphene reaches the second $Co_2C_{(020)}$ surface, both sides are anchored to $Co_2C_{(020)}$ surfaces (Figures 5.2i and 5.2k). In a remarkable process, the incorporation of additional carbon atoms results in cap lift-off on the (210) plane and nanotube growth, while the sides stay anchored to the (020) surfaces. At this point, the nanotube cap structure is determined and the elongation starts with well-defined diameter and chiral angle (Figures 5.2j and 5.2l).[186] It is interesting to note that on (210) surface C atoms are separated by four Co atoms. Therefore a facet with less than four atoms may have only Co atoms and also provide anchoring point (Figure 5.2k).

5.4.2 Work of Adhesion of Graphene on the Cobalt Carbide Surface

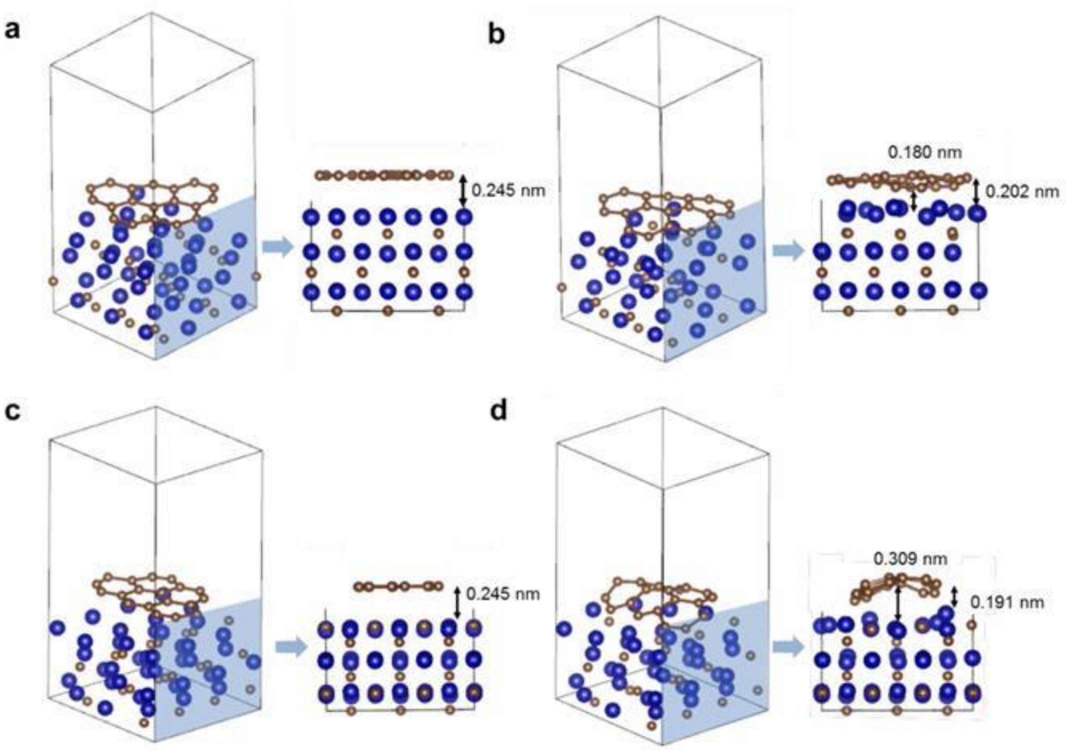

Figure 5.3 Models used in DFT simulation of graphene relaxation on $Co_2C_{(020)}$ and $Co_2C_{(210)}$ surfaces. (a) (c): Graphene sheets were initially placed at a distance of 0.245 nm from a Co terminated $Co_2C_{(020)}$ surface and at the same distance from a Co-C terminated $Co_2C_{(210)}$ surface, respectively. After relaxation of graphene on Co_2C surfaces, distance changes to 0.180 nm to 0.202 nm from $Co_2C_{(020)}$ (b) and to 0.191 nm to 0.309 nm from $Co_2C_{(210)}$ (d). These distances are in close agreement with the measured distance (Figure 5.2m). For each panel, a 3D view (left) and a side view (right) are proposed for visual clarity.

The anchoring of graphene on $Co_2C_{(020)}$ and its detachment from $Co_2C_{(210)}$ surfaces observed here in the 2D images can be explained by density functional theory (DFT) calculations, where full 3-D nature of the graphene/nanoparticle interaction can be explored. The Co_2C (020) and (210) surfaces are identified as Co terminated and Co-C terminated, respectively (Materials and Methods, Figure C.3 and Figure C.4 in Appendix C), which are reported to be stable terminations for these surfaces.[196] The distances between the graphene sheet and these two surfaces, and the corresponding work of adhesion values were calculated starting from the models as shown in Figure 5.3a and 5.3c. After relaxation, the graphene sheet is almost flat and in close contact with Co terminated (020) surface. The calculated distance between graphene and the nanoparticle ranges from 0.180 nm to 0.202 nm (Figure 5.3b). On the other hand, it forms a dome on Co-C terminated (210) surface with calculated distances of 0.191 nm on the edge and 0.309 nm at the center, respectively (Figure 5.3d). These values are in close agreement with experimental measurements (Figure 5.2m). The calculated work of adhesion for graphene on Co terminated (020) surface is higher than for Co-C terminated (210) surface with corresponding values of adhesion to be -26.5 eV nm^{-2} and -14.4 eV nm^{-2}, respectively (Table C.2 in Appendix C). Therefore, the nanoparticle surface termination plays a critical role in determining the work of adhesion between graphene and the nanoparticle: a Co terminated surface favors graphene anchoring, providing a 'vice grip' like hold, while a Co-C terminated surface promotes graphene detachment and cap lift-off. In both simulation and experiment, the central part of the graphene sheet is observed to be lifted from the (210) surface, but the edge of the graphene sheet is maintained in close contact with (210) surface forming a convex-like structure. Despite a low work of adhesion, the growing structure remains attached at its edge. This can be explained by the presence of dangling bonds at the graphene edges which tend to bind with the nanoparticle to be stabilized.

5.5 Conclusions

In summary, we have illustrated how atomically resolved dynamic imaging, combined with theoretical calculations, provide essential insights into nanomaterial nucleation and growth process. We find that catalytically active nanoparticles possess adjacent surfaces with dissimilar works of adhesion for graphene. We propose that this disparity between facets is essential for CNT growth as it offers the necessary combination of anchoring and lift-off sites. This favors the conversion of the graphene nucleus into a nanotube and prevents nanoparticles from encapsulating, which is one of the major causes of catalyst deactivation and reduction in CNT synthesis yield.[197-199] These first atomic scale observations show that, since the nanotube cap structure and the diameter are controlled by nanoparticle facet geometry, the chirality will also be determined at this stage. In future this information can be used to design a catalyst/support system for large scale synthesis of single walled CNTs with pre-defined chirality. A prerequisite for achieving this control is a strong catalyst/support interaction to preserve the distinct nanoparticle facets under growth conditions, as observed in our Co/MgO system. We believe that associating this type of catalytic system with a very narrow nanoparticle diameter distribution is essential for deterministically obtain SWCNTs with specific diameters and chiralities, and thus specific opto-electronic properties. Such experimental atomic resolution movies provide a consistent nano-scaled input for growth simulation models.

CHAPTER VI

NANOCATALYST SHAPE AND COMPOSITION DURING NUCLEATION OF SINGLE-WALLED CARBON NANOTUBES*

6.1 Summary

The dynamic evolution of nanocatalyst particle shape and carbon composition during the initial stages of single-walled carbon nanotube growth by chemical vapor deposition synthesis is investigated. Classical reactive and *ab initio* molecular dynamics simulations are used, along with environmental transmission electron microscope video imaging analyses. A clear migration of carbon is detected from the nanocatalyst/substrate interface, leading to a carbon gradient showing enrichment of the nanocatalyst layers in the immediate vicinity of the contact layer. However, as the metal nanocatalyst particle becomes saturated with carbon, a dynamic equilibrium is established, with carbon precipitating on the surface and nucleating a carbon cap that is the precursor of nanotube growth. A carbon composition profile decreasing towards the nanoparticle top is clearly revealed by the computational and experimental results that show a negligible amount of carbon in the nanoparticle region in contact with the nucleating cap. The carbon composition profile inside the nanoparticle is accompanied by a well-defined shape evolution of the nanocatalyst driven by the various opposing forces acting upon it both from the substrate and from the nascent carbon nanostructure.

---

* Reprinted with permission from "Nanocatalyst Shape and Composition During Nucleation of Single-Walled Carbon Nanotubes" by J. L. Gomez-Ballesteros, J. C. Burgos, P. A. Lin, R. Sharma, and P. B. Balbuena, 2015. *RSC Advances*. 5, 106377-106386, Copyright 2015 by The Royal Society of Chemistry.

This new understanding suggests that tuning the nanoparticle/substrate interaction would provide unique ways of controlling the nanotube synthesis.

6.2 Introduction

The availability of large-scale arrays of semiconducting nanotubes with specific structures and perfect alignment would constitute a revolutionary step in the field of electronics allowing for smaller dimensions, higher efficiency, and speed of operation in devices such as field-effect transistors (FET).[200-202] However, such structures are currently lacking,[203] limiting the incorporation of single-walled carbon nanotubes (SWCNTs) into electronic circuits. Approaches to overcome this limitation include separation *via* assisted dispersion,[204] electrophoresis,[205] ion exchange chromatography[206] and density-gradient ultracentrifugation,[104, 207] allowing separation by electronic behavior (metallic or semiconducting)[104, 204-205] or specific chiral structure.[206-207] Alternatively, controlling the nanotube structure during synthesis *via* control of the catalyst structure is considered a promising strategy.[15] The structure and properties of SWCNTs are believed to be defined during the catalyzed synthesis process. Once the nascent cap is fully formed, its structure is maintained throughout growth, provided the reaction conditions do not drastically change[183] and major rearrangements do not occur in the catalytic nanoparticle.[39] The existence of a correlation between nanocatalyst structure and the nascent nanotube cap, previously observed and reported as the *template effect*,[36, 113, 116] can play a crucial role defining the nanotube structure and may allow for the development of strategies to control SWCNT morphology during the synthesis process.

SWCNTs are typically synthesized by catalytic chemical vapor deposition (C-CVD), a process carried out with floating or supported transition metal nanocatalysts (Fe, Co, Ni, Cu, etc.) and hydrocarbons, ethanol, or CO as precursors.[107-108] SWCNT growth has been observed on both pure metal[60, 114, 149, 208] and carbide nanoparticles[50-51, 115, 121] posing questions about the stability of such phases and their role in the nucleation process and motivating investigation of the catalyst structural evolution during nanotube formation. One of the hypotheses proposed to explain nanotube growth is the vapor-liquid-solid mechanism (VLS);[209] in which carbon atoms diffuse into a liquid nanoparticle followed by nucleation on the catalyst surface and growth. Evidence for this mechanism comes from observation of fluctuations in the nanoparticle shape[50, 143] and decrease in the melting point of nanoparticles.[210] In contrast, direct observations of stable crystalline facets during nucleation and growth[121] indicate that the catalyst nanoparticle may be in a solid state in which its shape may fluctuate, but is stabilized by the forces acting upon it. In the case of supported nanocatalysts, metal oxide substrates are typically used and observed to influence the nanoparticle shape,[51, 211] and the nanotube mode of growth and anchorage in some cases.[212] The nucleation of small carbon islands on the particle surface of floating Ni and Fe catalysts has been investigated with density functional theory (DFT), focusing on the thermodynamics of carbon dissolution, precipitation and coalescence[46, 213] and the stability of carbide[214] compared to that of metal particles[122] during nucleation. Although some insights into the role of dissolved C as the driving force for nucleation have been introduced from these previous studies, most of them were focusing on static analyses of floating catalysts. However, a more thorough description of variations in the structure and composition of the particle due to the effect of interactions with the nascent cap and the support can be obtained from the dynamic evolution of the catalyst and nanotube during nucleation.

In the present work, we focus on the evolution of the structure of the catalyst nanoparticle during the early stages of carbon dissolution and nucleation of SWCNTs. Variations in shape, atomic ordering, and carbon concentration profile are studied by a combination of reactive molecular dynamics (RMD) and *ab initio* molecular dynamics (AIMD) simulations and analyses of real-time atomic-resolution videos taken in an environmental transmission electron microscope (ETEM). We look closely at the interactions of the nanoparticle with the substrate and the nucleating nanotube cap, and their effect on the nanoparticle structural parameters.

6.3 Methodology

6.3.1 Computational Details

Our approach employs two types of molecular simulations. Classical reactive molecular dynamics (RMD) simulations emulate the catalytic growth of single-walled carbon nanotubes in the tens of nanoseconds time scale, whereas *ab initio* molecular dynamics (AIMD) simulations allow observation of short time phenomena (order of tens of ps) providing detailed information on the chemical nature of the interactions of the involved species. In the RMD simulations the carbon-carbon interactions are described by a reactive bond order potential[89] that includes corrections with respect to the original potential developed by Brenner and collaborators.[215] The modifications consist of an extended parameterization that regulates carbon-carbon interactions inside catalyst nanoparticles. On the other hand, the metal-carbon interactions are represented through a reactive potential[89] according to the Tersoff scheme[216] that takes into account the hybridization states of C atoms and distinguishes among dissolved and surface C atoms, according to atomic coordination criteria. Metal-metal interactions are described by the many-body Sutton-Chen potential,[88] which has been successfully used to describe several properties of transition metals.[217-219] The metal/support interaction is parameterized: the adsorption strength of the catalyst nanoparticle to its support is set to 370 meV per atom (6.11 $\mathrm{eV \cdot nm^{-2}}$), an energy value which lies within the range reported for catalytic transition metal clusters supported on ceramic substrates such as Ag/MgO (1.43 $\mathrm{eV\ nm^{-2}}$ to 3.99 $\mathrm{eV\ nm^{-2}}$),[220-221] Pb/MgO (4.81 $\mathrm{eV\ nm^{-2}}$),[221] and Cu/MgO (11.98 $\mathrm{eV\ nm^{-2}}$).[222-223] The initial RMD system is formed by a carbide-like catalyst nanoparticle deposited on a rectangular monolayer substrate model. The substrate was placed at the bottom of a periodic box of the same cross sectional area as the area of the support, 3.98 nm wide (x-direction) and 3.88 nm deep (y- direction). A catalyst nanoparticle with the composition of cobalt carbide is then deposited on top of the substrate. The initial composition of the carbide-like particle is Co_2C; however its structure is that which results when 80 carbon atoms are dissolved into the pure metal catalyst made of 160 cobalt atoms. The vacuum of the periodic box is set in 50 nm height, providing the necessary volume to bring the pressure down to values as low as ≈ 18 kPa. This value represents the lowest nonzero pressure that can be achieved in the precursor gas phase; it results in supplying one single precursor atom into the periodic box. The temperature and the volume of the system are kept constant throughout the simulation. The atomic velocities of the system are adjusted to a target temperature of 650 °C through a thermostat.[89] The integration of the equations of motion is done through the predictor-corrector algorithm, using an integration time step of 0.5 fs until a total simulation time of 50 ns has been reached.

In addition, the interactions between a Co_2C nanoparticle and an MgO substrate are studied through AIMD simulations carried out using the Vienna *ab initio* simulation package (VASP)[124-128] with the Perdew-Burke-Ernzerhof exchange-correlation functional.[79] The projected augmented wave (PAW) pseudopotentials[81, 129] were employed to describe the electron-ion core interactions. The plane wave describing the valence electron density was expanded up to a cutoff energy of 400 eV. Γ-point sampling of the Brillouin zone is used for integration in reciprocal space. The partial occupancies were assigned considering a Gaussian smearing with a 0.05 eV width. Before performing AIMD, the structures were allowed to relax using a conjugate gradient algorithm until the energy difference was lower than 10^{-3} eV between consecutive relaxation steps and 10^{-4} eV between electronic self-consistent steps. AIMD simulations were carried out using the NVT ensemble at 600 ^{o}C with the Nosé thermostat and a time step of 1 fs. Atomic charges were estimated using the Bader analysis of charges,[130-131] in which the total charge of an atom is defined by the electron density enclosed by zero-flux surfaces. The AIMD model consists of a faceted Co_2C

nanoparticle containing 24 Co atoms and 12 C atoms (approximately 0.7 nm in diameter) deposited on a 1.5 nm x 1.5 nm five-layer periodic slab of MgO substrate. This model emulates a supported nanoparticle at an early stage in the nanotube growth process, prior to the nucleation of the carbon structure at typical growth conditions: 600 °C and ultra-low C pressure. The (200) surface facet of MgO and the (020) (only Co atoms at the interface) and (210) (Co and C atoms at the interface) facets of Co_2C were considered, as they have been observed and reported from environmental transmission electron microscopy (ETEM) studies.[121] Relaxation of the individual structures was performed allowing surface atoms to find positions of lower energy. In the case of MgO, the number of layers was selected based on convergence of the surface energy. In all cases of MgO relaxation, the two bottom layers were fixed at the bulk structure while the top layers were allowed to relax. Two different configurations (nanoparticle located epitaxial and almost non-epitaxial with respect to the MgO substrate) were used for each of the (200) and (210) surface orientations.

6.3.2 *In Situ* Experimental Details

An environmental transmission electron microscope (ETEM), operated at 300 kV, was employed to capture images of SWCNT growth. Acetylene (C_2H_2) and Co_xMo_{1-x}/MgO were used as carbon precursors and a catalyst-support, respectively. The catalyst/support was prepared by wet chemical method as described previously.[191] The catalyst-support system was first heated to 750 °C in oxygen (100 Pa) to remove impurities such as gaseous hydrocarbon adsorbed on the surface of the catalyst-support system. This step also resulted in oxidizing the metal nanoparticles, but they become reduced prior to CNT formation.[121] Then the sample was cooled down to a SWCNT growth temperature at 650 °C in vacuum (10^{-4} Pa) for 10 minutes before 0.01 Pa C_2H_2 was introduced. Atomic-resolution real-time videos were then acquired at 10 frames per second and used for phase identification.[121]

6.4 Results and Discussion

6.4.1 Carbon Distribution in the Catalyst Nanoparticle

Carbon atoms in RMD simulations are initially added at a partial pressure of 820 kPa to the catalytic surface, where atoms diffuse into the catalyst. The solubility of C atoms in the nanoparticle at this pressure is extremely high and the C concentration inside the nanoparticle rapidly reaches the Co:C ratio in Co_2C. In order to create the initial Co_2C model for the RMD simulations, the high-pressure (820 kPa) precursor gas flow is stopped as soon as the desired composition is obtained. This system is then exposed to low pressure conditions (18 kPa) for nucleation and growth. The steep decrease in the reaction pressure reverses the tendency of C atoms to saturate the Co clusters allowing initially dissolved C atoms to precipitate onto the catalyst surface. As this precipitation continues, the concentration of C atoms within the catalyst stabilizes. A relatively stable solution is reached at 15 ns, when the diffusion in both directions, in and out of the catalyst, becomes even, keeping constant (≈ 40 atoms) the total amount of carbon dissolved in the metal nanoparticle (Figure 6.1). The end of the C stabilization period marks the start of the cap nucleation stage, where the precipitated carbon, along with new catalyzed carbon, combine to initiate the formation of carbon chains and networks on top of the catalyst surface. Throughout this process, changes in shape and local composition take place in the catalyst nanoparticle, as a result of the dynamics of the C atoms diffusing in and out and association of C atoms on the surface. Variations in C composition of the particle throughout the nucleation process are driven by local differences in C chemical potential: dissolved carbon, carbon precipitated to the particle surface and carbon at the edges of the islands with unsaturated bonds. Therefore as the nanotube begins to nucleate, a decrease in the subsurface carbide species is expected due to variations in the local environment of C atoms and changes in the metal-carbon interaction.[46] This decrease in C concentration reportedly prevents the formation of new islands on the catalyst surface, and favors coalescence of the existing carbon formations on the surface.[213]

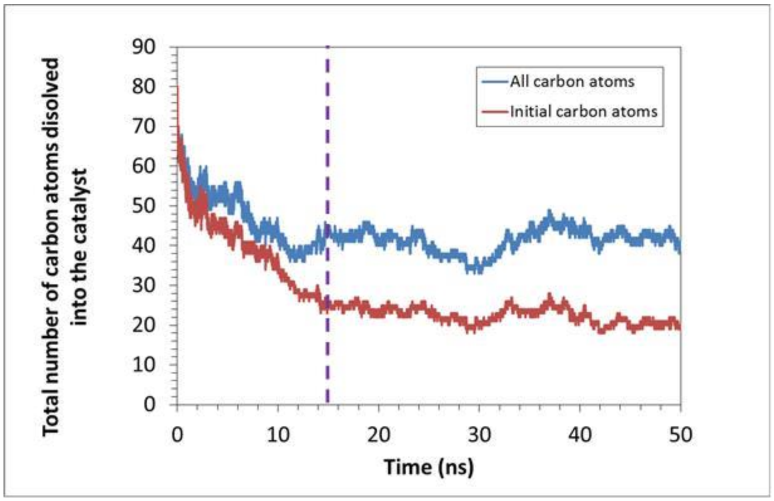

Figure 6.1 Number of carbon atoms inside the catalyst nanoparticle obtained from simulations. The red curve corresponds to the atoms forming the initial carbide composition that remain dissolved in the nanoparticle. The blue curve represents the sum of all dissolved atoms: those remaining from the initial carbide composition and the new ones incorporated from the gas phase. The purple line indicates the time when a Co_xC_y solution reaches a relatively stable global composition.

6.4.2 Evolution of Catalyst Nanoparticle Shape

Besides the global concentration of carbon atoms, a detailed analysis of the local concentration of carbon within the catalyst provides information about the routes of carbon dissolution and diffusion during SWCNT nucleation and growth. Z-density profiles are generated from the RMD trajectories by computing the number of atoms of a given species present in successive planes parallel to the substrate; each of the planes are stacked in the direction perpendicular to the substrate, thus defining the location of atomic layers. Z-density plots herein reported contain profiles for both carbon and metal atoms, where the height of each peak represents the population of the species in each layer. However, the Co:C ratio does not exclusively determine the presence of a nucleating carbide phase. Other factors such as the nearest neighbor distances and structural stability of the metallic solvent atoms could be indicators of carbide nucleation. Thus, Z-density profiles are used to obtain information about time evolution of the catalyst nanoparticle shape as they are related to the total number of peaks observed in the carbon and metal profiles. For instance, during the process of stabilization of the carbon concentration, the height of the first metal peak increases and the total number of peaks decreases (Figure 6.2: 5 ns to 7.5 ns). The higher metal peak in contact with the substrate reveals the spread of metal atoms on the substrate leading to a reduction in the number of atomic layers in the catalyst nanoparticle.

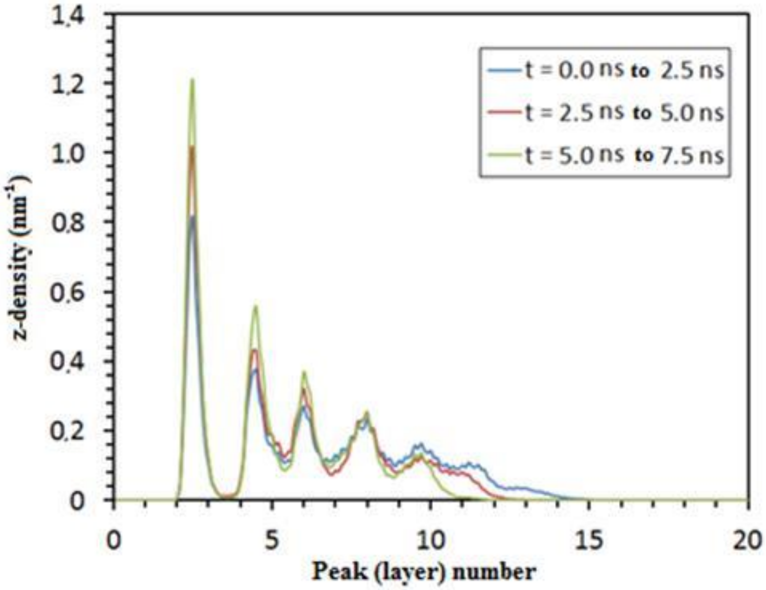

Figure 6.2 Z-density profiles for metal atoms forming the catalyst nanoparticle. Each curve corresponds to profiles calculated over 2.5 ns intervals. The number of peaks and the height of each peak provide information about the catalyst nanoparticle shape. The substrate is located at z = 0. The time interval corresponds to the C stabilization stage (see Figure 6.1).

As the global carbon concentration stabilizes and the carbon cap nucleation starts, the catalyst nanoparticle undergoes minimal variations in its shape. During cap nucleation, the metal atoms decrease their tendency to spread on the substrate surface finding some structural stability, although some nanocatalyst height reduction is still seen in this period, as shown in Figure 6.3a. The end of the nucleation stage takes place once the carbon cap completely covers the top of the catalyst surface (Figure 6.3a at 34 ns). When this event occurs, the catalyst nanoparticle finally stops spreading on the support and starts recovering some height as result of a counteracting force coming from the cap, which pulls the metal and dissolved carbon atoms upwards (Figure 6.3a). This phenomenon can be associated with step flow mechanisms observed through *in situ* experiments using an environmental TEM in which the catalyst particle undergoes a reversible deformation right before the cap lifts off.[143, 224] This elongation will be eventually followed by a shape recovery as result of the cap release.[143]

We have recorded the catalyst shape dynamics in real-time using environmental TEM. Figure 6.3b shows that the catalyst spreads laterally, as shown by the decrease in the number of atomic layers, before cap nucleation. During cap nucleation at the catalyst nanoparticle surface (time period 13.6 s to 14.2 s), the catalyst nanoparticle height reduces the most. Then the catalyst stops spreading and its height recovers one atomic layer when the cap forms fully and starts to lift off. The catalyst shape evolution in our *in situ* observations (Figure 6.3b) qualitatively agrees with the simulated results, even though they are in different time scales (Figure 6.3a) and different precursor pressures. The accelerated dynamics employed in our simulation model[89] are able to represent well the behavior observed in the experiments due to the ability to model the mechanisms involved in the nucleation process (*e.g.* C dissolution, C bulk and surface diffusion, and C precipitation to the particle surface). These are simultaneously responsible for the changes in shape and composition in the nanoparticle.

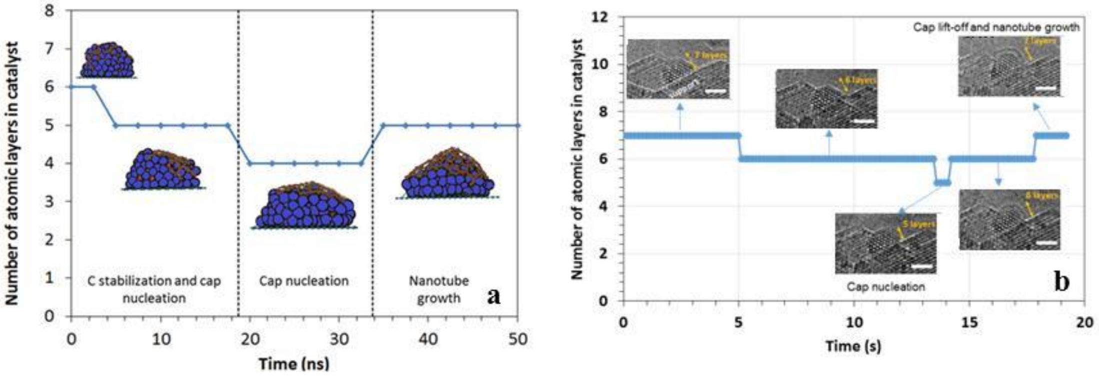

Figure 6.3 Shape evolution of the catalyst nanoparticle during the various nucleation and growth stages. a) RMD simulations illustrate that during carbon stabilization, the metal layer in contact with the substrate tends to wet the substrate (first ≈15 ns). Carbon nucleation starts before carbon stabilization is reached and leads to further reduction in the number of layers of the nanocatalyst particle. The slight vertical elongation of the nanocatalyst particle coincides with the beginning of the growth stage. b) In qualitative agreement with the simulated results, *in situ* experimental observations show that the nanocatalyst particle spreads laterally with decreasing number of atomic layers before the cap nucleation ends (at approximately 13 s). The bar is 1 nm.

Reshaping effects on the catalytic nanoparticle during SWCNT nucleation can thus be summarized as a) spreading of the nanoparticle on the substrate and a concomitant decrease in the number of layers while the global C composition is stabilized and the carbon cap nucleates; and b) elongation of the nanoparticle as the newly formed cap lifts off. Such events can seemingly be attributed to the interplay between the interactions of the carburized nanoparticle with the substrate and with the nascent cap. Previous RMD studies varying the substrate/catalyst adhesion energy E_{adh}[38, 211] showed that the strength of interaction between the substrate and the nanocatalyst plays an important role in determining the dynamics of the nanoparticle shape. In this work, we performed AIMD simulations of Co_2C nanoparticles deposited on MgO substrates aimed to emulate the experimental setting. As explained above, based on our previous work,[121] $Co_2C_{(020)}$ and $Co_2C_{(210)}$ the two facets potentially in contact with the support, are taken as the base model for the calculations. The initial configurations were constructed by bringing into contact the relaxed structures of a Co_2C slab cleaved along the (020) and (210) planes, exhibiting a pure Co termination and a Co-C termination respectively, with a five-layer MgO slab cleaved along the (200) plane. Changes in the nanoparticle shape and relative atomic distribution with respect to the substrate are observed as a result of the temperature-induced dynamics at 600 ^{o}C. Two initial configurations were considered for each termination differing in their relative location with respect to the substrate: i) most of the Co atoms are located on top of Mg atoms (indicated by the numeral 1- preceding the facet type), ii) most of the Co atoms are located in positions other than on top of Mg atoms (indicated by the numeral 2-). However after a period of equilibration, interfacial Co atoms are displaced from their original position preferring locations atop O atoms at the substrate interface in all cases (Figure D.1). Such behavior has been observed and described from calorimetric measurements[221] and theoretical calculations of transition metal clusters on the (100) facet of MgO[222-223] suggesting a covalent interaction between O and Co. The current AIMD simulations indicate that although the facets in the initial models are not kept, systems based on the same surface facet maintain structural similarities among them. These AIMD simulations, where the nanoparticle/substrate effect is separated from that of the nascent cap/nanoparticle, reveal that the nanoparticle shape is in part influenced by the nanoparticle/substrate interaction strength, which in turn is determined by the structure of the facet in contact with the substrate. After an equilibration period, the substrate induces a redistribution of C atoms in the catalyst that differs from the initially organized carbide structure, as C atoms, displaced from their original locations, intercalate among pure Co and Co-C layers (Figure 6.4). Moreover, the (020) –based nanoparticles tend to adopt a rounded cubic shape, whereas the (210) ones rearrange into an egg-shape. In the absence of a driving force, no C aggregation or precipitation on the nanoparticle surface is observed. In all cases, the nanoparticle/substrate interface contains predominantly Co atoms, with the migrated C atoms appearing between the Co layer in contact with the substrate and the adjacent Co layer. This Co-enrichment of the layer in contact with the substrate (Figure 6.4) is in agreement with that observed in the RMD simulations.

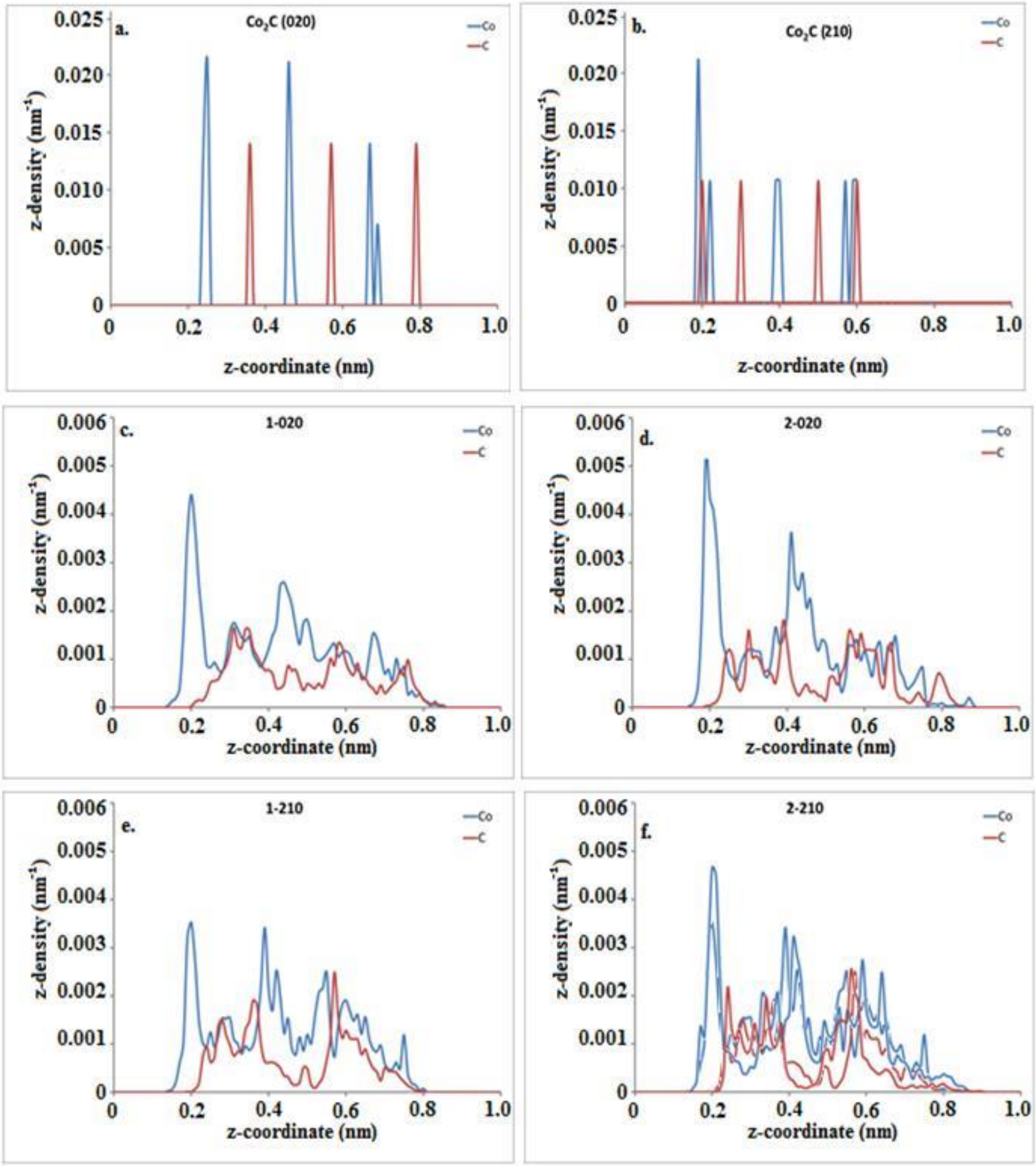

Figure 6.4 Z-density profiles for Co and C atoms forming the supported nanoparticle from AIMD simulations of Co_2C nanoparticles on MgO substrates. Initial configurations of a) $Co_2C(020)$, and b) $Co_2C(210)$. c, d, e, f) Density profiles after 3 ps. Changes in the catalyst shape are evidenced by irregularities in the height, distribution and extension of the peaks. Overall, the atomic distribution in the supported nanoparticle models evolves toward a first layer of pure Co in contact with the substrate, followed by alternations between a layer with Co and C in almost equal proportion and another of pure Co. The substrate is located at $z = 0.0$ nm.

In order to quantify the nanoparticle-substrate interactions, we estimate the strength of adhesion of the nanoparticle to the support surface per Co atom at the interface, E_{adh}, in the cases studied. We calculated the energy of adhesion by subtracting the energies of the individual components of the system ($E_{\mathrm{Co_2C}}$ and E_{MgO}) frozen in their interacting configuration from the energy of the combined system $E_{\mathrm{Co_2C/MgO}}$ divided by the number of Co atoms at the interface N_{Co} as illustrated in eq 6.1.

$$E_{adh} = \frac{E_{Co_2C/MgO} - \left(E_{MgO} + E_{Co_2C}\right)}{N_{Co_i}} \tag{6.1}$$

Figure 6.5 shows the calculated energies of adhesion per Co-atom for each of the models considered. Since the values are normalized, a direct comparison between energies of adhesion can be established. The calculated values are comparable to the experimental and theoretical values reported between transition-metal clusters and an MgO support; the strength is in the moderate to strong range.[221, 223]

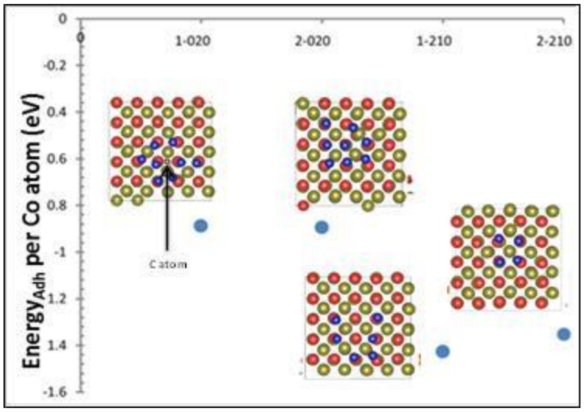

Figure 6.5 Energy of adhesion per Co atom for each configuration of the two surface facets studied: (020) and (210). The insets next to each label illustrate the nanoparticle-substrate interface for each case depicted with Mg atoms in green, O atoms in red, Co atoms in blue and C atoms in brown. Due to the fact that the nanoparticle/substrate interface contains predominantly Co atoms, only one C atom depicted as a small brown sphere is shown in the 1-020 system.

For a given nanoparticle facet in contact with the substrate (for example (020) or (010)), the calculated adhesion energies do not depend on the specific initial location of such facet with respect to the substrate lattice. In contrast, nanoparticles exposing different facets display different nanoparticle/substrate adhesion energies. In spite of these energetic differences, Figures 6.4 and D.1 show that both (020) and (210) based structures on MgO evolve towards similar composition of the nanoparticle contact layer (pure Co) and comparable distances between Co and substrate atoms (Figure D.2). In addition, a smaller number of Co atoms is found at the contact layer in the (210)-based structures and these atoms are subject to a stronger interaction with the substrate compared to the (020)-based ones.

A closer look at the interactions between the substrate and the Co_2C nanoparticle models can be obtained from an estimation of partial atomic charges and charge transfer between atoms at the interface (Figure D.3). Atomic charges in the substrate atoms show equal magnitudes (≈ 1.38 e^-) with positive and negative signs for Mg and O respectively, indicating a neutral net charge in the substrate. No significant difference in the average charge distribution was found between substrate atoms at the interface and in the bulk of the support.

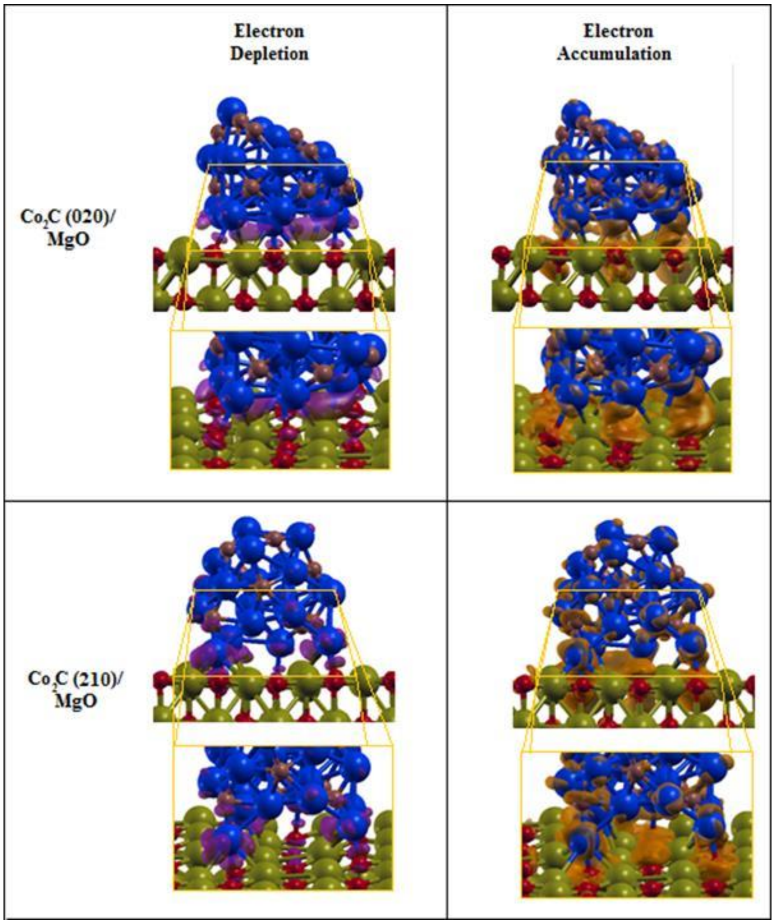

Figure 6.6 Accumulation (orange) and depletion (purple) of electron density in 2-(020) and 1-(210). Regions of electron accumulation are located around O atoms (red) and the interface with the nanoparticle. Regions of depletion are located around Co atoms (blue) across the layer in contact with the substrate revealing charge transfer from the nanoparticle to the substrate (Co→O). Mg atoms and C atoms are depicted in green and brown respectively.

Average partial charges for Co atoms near the substrate/nanoparticle interface which are evaluated separately from atoms elsewhere in the nanoparticle, exhibit a slightly higher average positive charge (0.39 e^- and 0.44 e^-) than Co atoms in the rest of the nanoparticle (0.28 e^- and 0.27 e^-) in the (210)-based nanoparticles. The opposite trend is observed for the (020)-based structures. Similarly, C atoms located closer to the substrate bear charges with higher magnitude (more negative) than C atoms located elsewhere. These results suggest that this polarization of the nanoparticle atoms close to the interface with the ionic crystal substrate may contribute to the stronger interaction of the (210)-based nanoparticles (≈ 1.4 eV per Co atom) compared to the (020) case (≈ 1 eV per Co atom). Altogether, as carbon is being dissolved in the nanoparticle and the nucleation process begins, the nanoparticle shape (described in terms of the number of layers and the relative distribution of atoms therein) is dependent on the strength of interaction of the nanoparticle with the substrate. This interaction is shown to be related to the extent of the electron transfer between the interfacial metal atoms and their neighboring C and O atoms (Figure 6.6), which in turn is affected by the way metal atoms are distributed at the interface. As the nucleation stage starts and the nanotube cap is formed, a competition between the nanoparticle/cap and the nanoparticle/substrate interactions will arise which leads to particle reshaping as shown in Figure 6.3. Moreover, carbon redistribution inside the nanoparticle is also induced by nucleation as discussed next.

6.4.3 Carbon Gradient Inside the Catalyst During Cap Nucleation Stage

Changes in the local distribution of C atoms are observed in both ETEM images and RMD simulations during the cap nucleation stage after the global carbon concentration stabilizes. Z-density profiles from RMD simulations (Figure 6.7) are used to generate carbon concentration profiles (Figure 6.8) for various time frames of the nucleation stage. The C atoms are highly concentrated near the catalyst support, and depleted away from it (Figure 6.7). The ratio of C to metal is quantified by the peak heights of carbon and metal in the Z-density profile at each layer position. The analysis of carbon concentration does not include the pure metal contact layer (negligible carbon concentration) which is due to a strong repulsion exerted by the support potential over carbon atoms, as shown from the DFT analysis (Figures 6.5 and 6.6) where the interfacial energies are dominated by the Co-O interactions. This repulsion leads to a pure metal phase near to the nanoparticle/support interface, and a highly concentrated carbon-metal solution in the immediately adjacent layer. The carbon concentration decreases almost linearly in the perpendicular direction out of the support plane, passing through different stoichiometric carbide compositions (Figure 6.8). At the top of the catalyst (layer 3 in Figure 6.8), the cluster is almost depleted in carbon as the cap is being formed on the nanocatalyst surface. The carbon to metal ratio drops to as low as 0.1 (Figure 6.8). Metal subsurfaces depleted of C have also been observed during graphene growth on Ni(111) surfaces using X-ray photoelectron spectroscopy (XPS) suggesting that the presence of C free subsurface layers may act as catalyst for both diffusion of C from the bulk and desorption at the surface for incorporation of C to the graphene.[225] Classical molecular dynamics and DFT static optimizations of Ni and Fe floating catalysts during nucleation of SWCNTs have also demonstrated variations of the C concentration in the particle.[213-214] In contrast with what is observed here with supported catalysts, the relative C distribution for the floating catalysts is found to be more homogenous throughout the nanoparticle[213] and different carbide configurations are reportedly similar in stability, indicating that carbide intermediate species with different configurations may be likely to co-exist.[214]

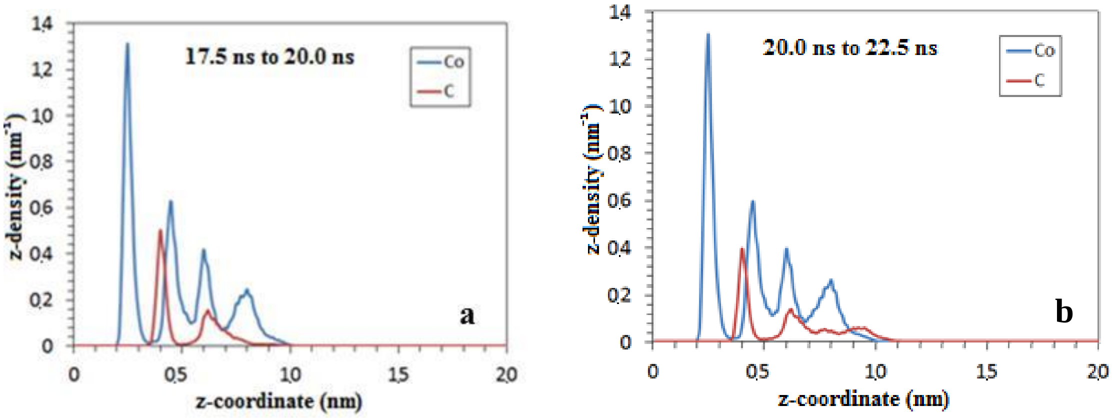

Figure 6.7 Z-density profiles for two intervals of 2.5 ns (where a) 17.5 ns to 20.0 ns and b) 20.0 ns to 22.5 ns) within the nucleation stage in RMD simulations. The location of the peaks indicates the presence of a high atomic density in a 0.01 nm thick slice, parallel to the support plane located at z =0.

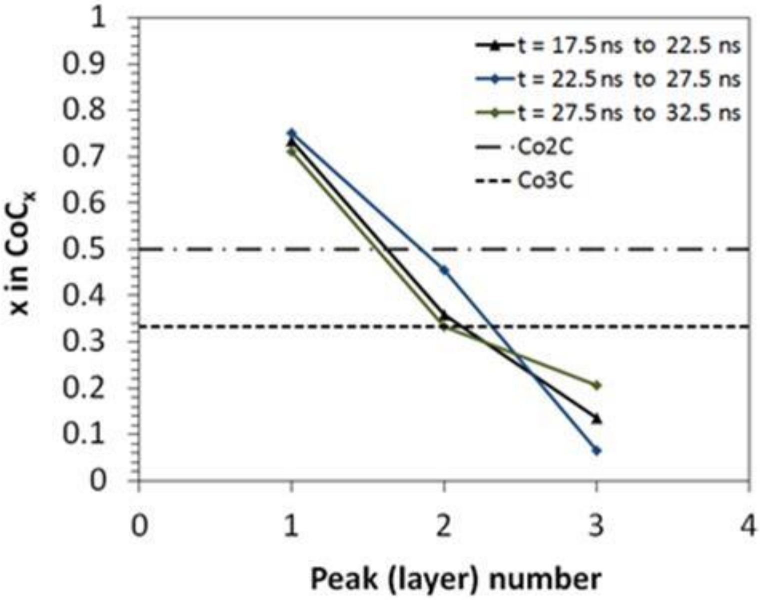

Figure 6.8 Local concentration profiles of carbon atoms relative to metal atoms at the nucleation stage from RMD simulations. Each concentration curve corresponds to an interval of 5 ns, computed as an average of concentrations obtained from two consecutive z-density profiles of 2.5 ns each. The concentration points are obtained from z-carbon density profiles reported in Figures 6.7. Layers are numbered 1 to 3 from the bottom to the top layer. The horizontal lines indicate the C/Co atomic ratio of two known carbide phases: Co_2C and Co_3C.

AIMD simulations of a graphene seed deposited on top of the supported Co_2C/MgO nanoparticles show a similar trend (Figure 6.9). Three atomic layers can be identified: the bottom layer containing Co atoms located atop O atoms in the substrate, a middle layer containing C atoms and a top layer consisting of Co atoms in contact with the graphene seed after 1/3 of the C atoms from inside the nanoparticle are incorporated into the graphene structure that adopts a cap shape. In agreement with the C concentration profile discussed in Figure 6.8, C atoms are distributed in the middle layer and between layers with decreasing local composition from bottom to top (*i.e.* 4 C atoms between layers 1 and 2, 3 C atoms in layer 2 and 1 C atom between layers 2 and 3). The *global* composition of C in the nanoparticle changes from Co_2C to Co_3C due to the incorporation of C atoms to the graphene, which also allows the graphene fragment to reorganize its structure including pentagons and inducing curvature into the structure. Typical meta-stable carbides present in the bulk Co-C phase diagram (*e.g.* Co_2C and Co_3C) can be formed following saturation of carbon in the solid solution, accompanied by carbon precipitation as graphene.[226] Our model emulates the limit of ultra-low pressure during growth, therefore diminishing the dynamics of C migration and incorporation of C to the graphene, and causing the *global* Co-C stoichiometry inside the nanoparticle to be stabilized as Co_3C.

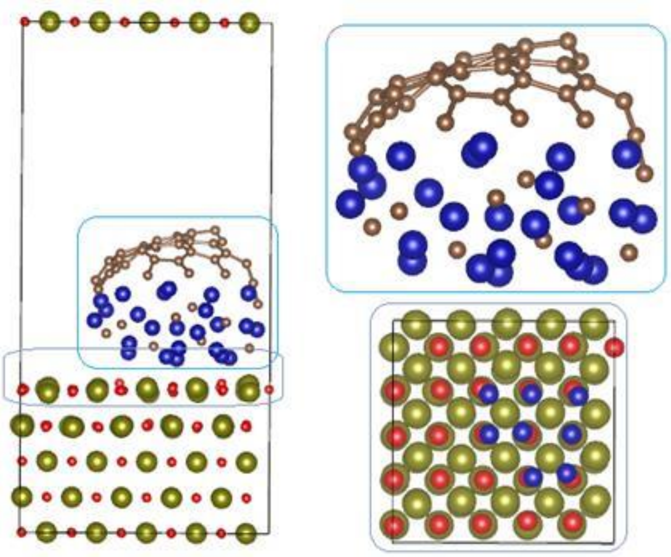

Figure 6.9 Snapshot from AIMD simulations (t = 3ps) of the Co_2C/MgO + graphene model with insets for the carburized nanoparticle with graphene (top right) and top view of the contact layer of Co atoms deposited on MgO (bottom right). Color code: Mg atoms in green, O atoms in red, Co atoms in blue and C atoms in brown.

This analysis suggests that the carbon cap forms out of carbon atoms supplied from the nanocatalyst particle topmost layer, which in turn compensates its depletion taking carbon atoms from lower layers *via* diffusion, as observed in RMD simulations. The linear concentration gradient depicted in Figure 6.8 is then roughly kept throughout the nucleation stage, exhibiting a wide range of carbon concentrations, including Co_2C and Co_3C carbide stoichiometric relations in the heart of the catalyst nanoparticle. The nucleation process ends with the formation of a graphitic carbon cap extended all over the top catalyst, which covers at least the two topmost layers of metal.

Furthermore, we use atomic-resolution images extracted from real-time videos to measure the distances between atomic columns and angles between them to identify the metal and or carbide phase present during growth. We have established an image process scheme to locate the position the atomic columns by template matching. For each atomic column, the distances between neighboring atom columns were averaged, and these values were used to identify the structure and thereby composition of the area (Co or Co-carbide). Prior to CNT formation, CoO nanoparticles are reduced to Co during C_2H_2 exposure before converting to Co_3C and then to Co_2C, as reported earlier.[121] Moreover, nanoscale chemical analysis confirmed that the Mo, though present in the catalyst-support system, was not present in any of the nano-particles, whether these nanoparticles were active or inactive for SWCNT growth. Therefore the role of Mo is not clear at this point and therefore not included in our simulations. However, during the nucleation process (13.4 s to 14.24 s), the images show the presence of Co-carbides (Co_2C or Co_3C) in the layers close to the support, and a depletion of carbon away from the support (mostly pure Co) (Figure 6.10), which is in agreement with our RMD and AIMD results. Similar results have been predicted by combining TEM images and concentration profiles obtained by numerically solving a steady-state diffusion equation for Ni nanoparticles during plasma enhanced CVD. Precipitation rates were predicted to be higher just below the gas-metal surface in correlation with the concentration gradient.[227] In our simulation studies, small fluctuations of the C concentration profile with time are observed, suggesting that precipitation rates and thus nanotube growth rates may also fluctuate due to changes in carbon solubility and diffusion in different regions of the nanoparticle.

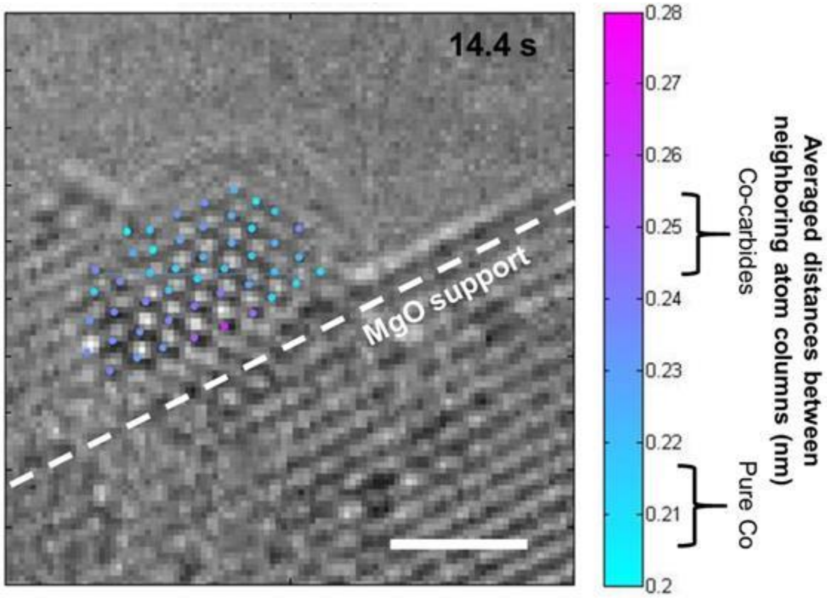

Figure 6.10 Atomic-resolution image in the cap nucleation stage. Atom columns of the catalyst nanoparticle are located and colored according to their average distances between neighboring atom columns (gradient color maps from light blue to purple). Regions of Co-carbides and pure Co in the particle show the carbon depletion zone away from the MgO support and covered by the carbon cap. Scale bar is 1 nm.

6.5 Conclusions

The dynamic evolution of supported Co carbide nanoparticles (Co_2C/MgO) during the nucleation stage of single-walled carbon nanotube growth was explored using reactive- and *ab initio* molecular dynamics simulations coupled with *in situ* environmental transmission electron microscopy imaging. Changes in the nanocatalyst shape and composition are examined throughout the nucleation process beginning with carbon dissolution, diffusion and formation of carbon chains on the surface until a cap is fully formed and the nanotube structure defined. The amount of carbon dissolved in the carbide-like nanoparticle decreases as C atoms precipitate at the surface. Once nucleation of the surface C atoms begins, a steady state global C concentration is reached. Changes in the nanoparticle shape occur linked with changes in the dynamics of C atoms according to experiments and RMD simulations: a decrease of the nanoparticle height and spreading over the substrate is observed while the C composition is stabilized, no changes occur as the cap is being formed, and subsequent elongation and shape recovery take place due to interactions with the cap as it lifts off. The main two factors influencing nanoparticle shape and C distribution can thus be summarized as: interactions with the substrate and interactions with the nascent nanotube. The nanoparticle evolution in relation to its interaction with the substrate from AIMD studies reveals that the nanoparticle/substrate interface is dominated by interactions between Co atoms located atop O atoms in the substrate. Strong nanoparticle/substrate interactions are characterized by electron transfer and re-arrangement of Co atoms at the interface stemming from a given Co_2C surface termination (*i.e.* (020) and (210)). The interactions of the nanocatalyst with the cap are responsible for the C gradient observed along the direction perpendicular to the substrate in both simulations and experiments. This suggests that the catalyst topmost layer is a primary source of C atoms for the formation of the nanotube cap. Overall, the combination of atomistic simulations and *in situ* observation of SWCNT growth provides insights into the fundamental phenomena driving the observed changes in the nanoparticle and allows the identification of key aspects for the formulation of models and mechanisms to better understand and control the catalytic process.

CHAPTER VII

DIRECT EVIDENCE OF ATOMIC-SCALE STRUCTURAL FLUCTUATIONS IN CATALYST NANOPARTICLES

7.1 Summary

Rational catalyst design requires an atomic scale mechanistic understanding of the chemical pathways involved in the catalytic process. A heterogeneous catalyst typically works by adsorbing reactants onto its surface, where the energies for specific bonds to dissociate and/or combine with other species (to form desired intermediate or final products) are lower. Here, using the catalytic growth of single-walled carbon nanotubes (SWCNTs) as a prototype reaction, we show that the chemical pathway may in-fact involve the entire catalyst particle, and can proceed *via* the fluctuations in the formation and decomposition of metastable phases in the particle interior. We record *in situ* and at atomic resolution, the dynamic phase transformations occurring in a Cobalt catalyst nanoparticle during SWCNT growth, using a state-of-the-art environmental transmission electron microscope (ETEM). The fluctuations in catalyst carbon content are quantified by the automated, atomic-scale structural analysis of the time-resolved ETEM images and correlated with the SWCNT growth rate. We find the fluctuations in the carbon concentration in the catalyst nanoparticle and the fluctuations in nanotube growth rates to be of complementary character. These findings are successfully explained by reactive molecular dynamics (RMD) simulations that track the spatial and temporal evolution of the distribution of carbon atoms within and on the surface of the catalyst particle. We

anticipate that our approach combining real-time, atomic-resolution image analysis and molecular dynamics simulations will facilitate catalyst design, improving reaction efficiencies and selectivity towards the growth of desired structure.

7.2 Introduction

Revealing the mechanisms by which nanometer sized catalysts act in chemical reactions and material syntheses is essential for the precise control of reaction rate, product selectivity, and ultimately, catalyst design. For example, based on the existing understanding of heterogeneous catalysis, it is assumed that the role of the catalyst in the synthesis of carbon nanotubes (CNTs) by catalytic chemical vapor deposition (C-CVD), is to decompose adsorbed carbon precursors and act as a template for CNT (graphene) nucleation.[228-229] However, the detailed steps leading to graphene nucleation and subsequent nanotube growth have not been experimentally established. An alternative hypothesis, suggested by Baker *et al.* [230], and later supported by molecular dynamics simulations[47], is that the catalyst acts as a reservoir, dissolving carbon atoms in a liquid phase that precipitates C in a solid form (carbon fibers) after reaching a supersaturated concentration, analogous to the vapor-liquid-solid (VLS) mechanism proposed for silicon nanowire growth [231]. However, *in situ* high-resolution transmission electron microscopy (HRTEM) studies have shown that the catalyst particles are crystalline, and not liquid, during CNT growth [51, 188-189, 232]. These results suggest a vapor-solid-solid (VSS) mechanism, where the carbon atoms may diffuse on the solid catalyst surface, to form the nanotube without dissolving into the catalyst[188, 233]. However, if dissolution of

C into the catalyst particle were to occur, there are two possibilities: 1) formation of a stable carbide, leading to inactivation of the catalyst [234], or 2) formation of a solid solution or metastable carbides that allow for continued catalytic activity [50, 121, 190, 235]. In this latter scenario, the carbon in the catalyst nanoparticle represents a reactive intermediate that can combine with surface carbon.

Recently, metal catalyst particles have been reported to convert to a carbide phase prior to CNT growth [121],[190, 236]. Several theoretical studies on nucleation and growth of CNT using various simulation techniques[186] including reactive molecular dynamics[55, 237], tight binding[136, 238], and time-stamped force-biased Monte Carlo simulations[239] of Ni and Co catalysts have suggested that carbon atoms diffusing in and out of metal particles are present at different stages of the process, thereby providing evidence that carbon atoms indeed diffuse into the catalyst bulk prior to incorporating into SWCNTs. Structural heterogeneity for cobalt catalyst nanoparticles during triple wall carbon nanotube growth has also been reported [235]. The lower energy of M-C bond formation, for example, 2.6 eV for Ni-C compared to 6.6 eV for C-C bonds [89, 240], and the stronger cohesion energy per formula unit of Ni-C (10.1 eV) compared to Ni-Ni (4.5 eV) and C-C (7.4 e)[238] favor metal carbide formation over graphene as explained in an earlier report.[55] However, the existence of carbide structures raises further questions concerning the role of the catalyst in nucleating CNTs: does carbon diffuse on the surface of the metal carbide or *via* the bulk, as proposed for metal particles? Or do metastable carbide structures, formed under non-equilibrium conditions, play a part?

By employing an *in situ* environmental transmission electron microscope (ETEM) as an experimental platform and reactive molecular dynamics (RMD) simulations [177, 194] We resolve the entire process from the nucleation and growth of a SWCNT from a single catalyst nanoparticle to termination (catalyst deactivation). Here, we present the observed and simulated time-resolved structural dynamics of catalyst nanoparticles under non-equilibrium conditions during SWCNT growth and compare the chemical changes associated with phase fluctuations to the carbon incorporation rate in growing nanotubes. Intriguingly, we identify two sources of carbon supporting the SWCNT growth 1) Surface diffusing C atoms that are incorporated at a constant rate 2) C atoms diffusing out of metastable carbides in the particle bulk, incorporated at fluctuating time intervals. Our results hold relevance for a number of other chemical reactions where Co nanoparticles are used as active catalysts for *e.g.* Fischer Tropsch process for hydrocarbon synthesis and petroleum cracking [241]. A broader implication of this study is that our methods may be employed to resolve dynamic atomic-level processes in heterogeneous catalysis.

7.3 Methodology

7.3.1 ETEM Experiments

Atomic-resolution videos of SWCNT growth were recorded using an environmental transmission electron microscope (ETEM), operated at 300 kV and equipped with an image corrector, at a rate of 10 frames per s. Acetylene (C_2H_2) and Co_xMo_{1-x}/MgO (prepared by wet chemical methods)[191] were used as carbon precursors and a catalyst-support system, respectively. The catalyst-support system was first heated to 750 °C in oxygen (100 Pa) to remove impurities such as gaseous hydrocarbons adsorbed on the surface. Then the sample was cooled to the SWCNT growth temperature of 650 °C in vacuum (0.0001 Pa), and was maintained at this temperature for 10 minutes before exposing to 0.01 Pa of C_2H_2. Crystalline Co clusters precipitated from the support and formed 2 nm to 5 nm sized particles. These particles nucleated and grew SWCNTs. No molybdenum was found within the nanoparticles as reported earlier [121].

7.3.2 Simulation Methods

Classical reactive molecular dynamics (RMD) simulations as implemented in our SIMCAT code [89] were employed to simulate the catalyst particle during SWCNT growth. The model consists of a carbide-like particle (1.8 nm diameter, 160 atoms) with Co_2C composition deposited on a rectangular monolayer substrate model in an atmosphere of a C precursor gas model ($P \approx 18{,}000$ Pa, corresponding to 1 C atom in the box). The simulation box was 3.98 nm long, 3.88 nm wide, and 50 nm deep. The reactive empirical bond order (REBO) Brenner potential [90], which is based on the Tersoff [216] and Tersoff-Brenner potentials [242] was used to represent carbon-carbon interactions. Metal-carbon interactions were described using a DFT-parameterized potential based on a many-body scheme based on the Tersoff potential that combines Morse-type repulsive and attractive terms with an additional screening parameter which takes into account the coordination of C atoms to distinguish between surface atoms and dissolved C atoms, and different hybridization states [89]. The many-body Sutton-Chen potential[88] was used to describe the metal-metal interaction and the metal-substrate interaction was parameterized using an average adsorption strength of 6.11 eV·nm^{-2}. A predictor-corrector algorithm and a time step of 0.5 fs were used in the integration of the equations of motion and the temperature was maintained at 650 °C using the Nosé-Hoover thermostat [89]. The dissolution residence time (τ_D) is the time that a C atom remains dissolved in the particle. A number of metal first nearest-neighbor (MNN) greater than or equal to 5 (MNN ≥ 5) was used as criterion to determine whether C atoms were dissolved or not. C atoms that do not dissolve in the particle ($\tau_D = 0$ ns) are labeled as SD, those remaining dissolved for less than 3 ns (0.001 ns $\leq \tau_D \leq 3$ ns) as BD, and those remaining dissolved for longer ($\tau_D \geq 3$ ns) as CF.

7.4 Results and Discussion

7.4.1 Environmental TEM

Figure 7.1a is a frame extracted from a video of SWCNT growth from a (2.5 ± 0.04) nm diameter Co catalyst particle (uncertainties represent the deviation from a perfectly spherical shape) supported on MgO. As reported earlier, the metal particle converts to a carbide phase with continued exposure to C_2H_2, before nucleating a SWCNT [121] The video sequence used here was captured after the nucleation of a SWCNT with its rim anchored to the particle, enclosing approximately one-third of the top portion of the particle (marked by arrows in Figures 7.1a and 7.1d). Within this individual (2.5 ± 0.04) nm diameter particle, two distinct regions with different structures and a clear boundary, can be visually identified (Figures 7.1a and 7.1d): a region of the particle that is mostly enclosed in the SWCNT (R1), and the rest of the particle (R2). By measuring lattice spacings and angles from the fast Fourier transforms (FFTs) of the high-resolution images (Figures 7.1b and 7.1c), the structures of the regions R1 and R2 are identified as Co metal and Co_2C, respectively (Figure E.5 and Table E.1). While the co-existence of Co, Co_2C and other related phases in an active catalyst particle has been reported [235], 'direct evidence' in the images showing two structures with a pronounced boundary has not been reported before. *Ex situ* electron diffraction studies of Co have also reported the formation of Co_3C and Co_2C at 450 °C and 500 °C, respectively, that decomposed to Co upon heating above 650 °C[192]]. It is possible that such metastable structures with clear boundaries co-exist in nanoparticles under non-equilibrium conditions and can only be revealed by high resolution images acquired under reaction conditions.

In addition to the co-existence of these two distinct structures, their respective areas (R1 and R2) are observed to fluctuate during SWCNT growth (Figures 7.1e-h). In order to quantitatively evaluate the relative areas of R1 and R2, and their evolution with time, careful measurements of distances between individual atomic columns in each frame are required. We establish an image processing scheme (IPS) that locates the atomic-column positions in each frame, measures the average first nearest-neighbor distance for every individual column, and then assigns atomic columns as belonging to the Co metal (0.22 nm) or Co-carbide (0.25nm) phases accordingly [243] (Figure E.6). The high precision of the IPS (7 pm and 15 pm for Co and Co-carbide respectively) enables the accurate assignment of phases and identification of phase boundaries [243]

This quantification finds the size of the Co area (R1) at 4.0 s to be approximately 1.33 times larger (Figure 7.1e) than that at 10.0 s (Figure 7.1f). After 10.0 s, the size of this area increases again (Figure 7.1g), and then decreases at 40.0 s (Figure 7.1h). The variation in sizes of R1 can be attributed to the difference between the rate of carbide decomposition (r_1, eq 7.1) and formation (r_2, eq 7.2). This leads to a decrease (xC) or increase (yC) in the total carbon amount ($\mathit{\Delta(t)}$) in the particle (eq 7.3) under non-equilibrium conditions.

$$Co_2C \xrightarrow{r_1} Co_2C_{1-x} + xC \tag{7.1}$$

$$yC + Co_2C_{1-y} \xrightarrow{r_2} Co_2C \tag{7.2}$$

$$\Delta(t) = r_1(t) - r_2(t) \tag{7.3}$$

The data-rich IPS results are also employed to evaluate the carbon content in the particle at any given time. We first carefully measure the carbon distribution within the particle in one frame (Figure 7.2a). The ratios of carbon to Co (C:Co) in each atomic layer are shown in Figure 7.2b, where layer 1 is in contact with the MgO support and layer 10 is the top surface that is enclosed by the growing SWCNT (red arrow). We find that the C:Co ratio is 0.5 in the first three atomic layers, and then gradually drops down to 0.31 in the next five layers. For the 9th and 10th atomic layers, the ratios for are approximately 0.16 (Figure 7.2b).

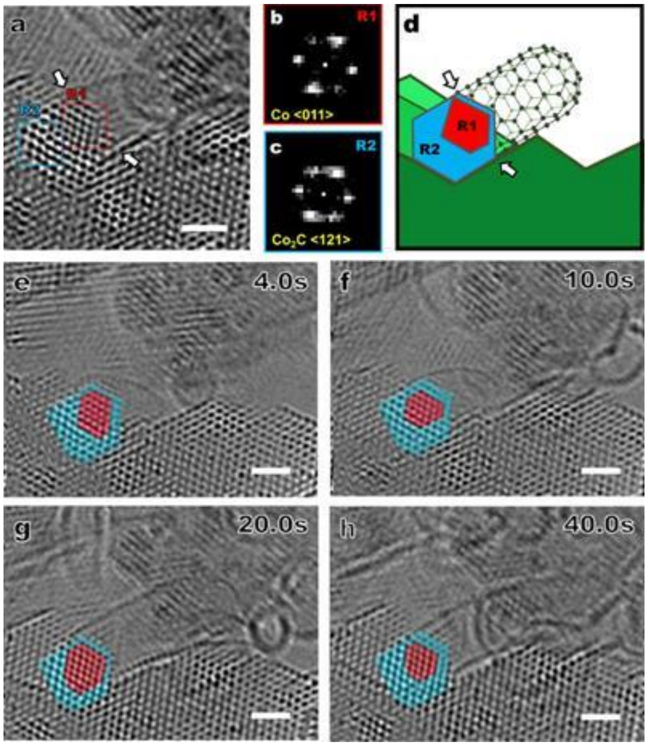

Figure 7.1 Co and Co_2C domains in catalyst nanoparticle and dynamic fluctuations in their relative areas. (a) A high-resolution image of a catalyst particle during SWCNT growth that contains two distinct regions, R1 and R2. (b) and (c) FFT from R1 and R2 showing the structures in R1 and R2 as Co and Co_2C, respectively. (d) A simplified illustration of Figure 7.1a identifying the catalyst particle with the two structures R1 and R2, in contact along one edge with the MgO substrate, which is in the same plane (dark green). MgO planes below the particle, are marked as lighter shades of green. (e-h) High-resolution snapshots of CNT growth at 4.0 s (e), 10.0 s (f), 20.0 s (g), and 40.0 s (h). Co (R1) and Co-carbide (R2) areas are colored red and blue, respectively, to highlight the change in respective areas with time. All scale bars represent 1 nm.

Experimentally, the number of carbon atoms in the nanoparticle at time *t* ($C_p(t)$) can be obtained from individual frames of the growth video by measuring the volume of the Co_2C region, relative to the volume of the catalyst particle (Figure E.6). Figure 7.2c shows the variation in $C_p(t)$ as a function of time. The amount of carbon inside the particle fluctuates aperiodically until the supply of carbon precursor is ended. For instance, the amount of carbon drops to (163 ± 3) atoms at 3.6 s, increases again to (210 ± 3) atoms at 9.8 s, and then drops to (162 ± 3) atoms at 16.5 s. The uncertainty in $C_p(t)$ is derived by propagating the uncertainty in atomic position identification (15 pm) through equations shown in the Appendix E. In order to elucidate the role of carbide phase for the SWCNT growth, we measure relative change in the length of the growing SWCNT with time. Since the diameter of the growing SWCNT remains relatively unchanged during this observation period, we obtain number of the carbon atoms added during a specific time period by measuring the increase in the arc length of the tube profile (Figure E.7) in each frame. The plot in Figure 7.2d shows the variation in the number of carbon atoms added to the SWCNT as a function of time. A stochastic fluctuation in the growth periods and intervals between growth periods is observed and is in agreement with earlier reports.[244-245]

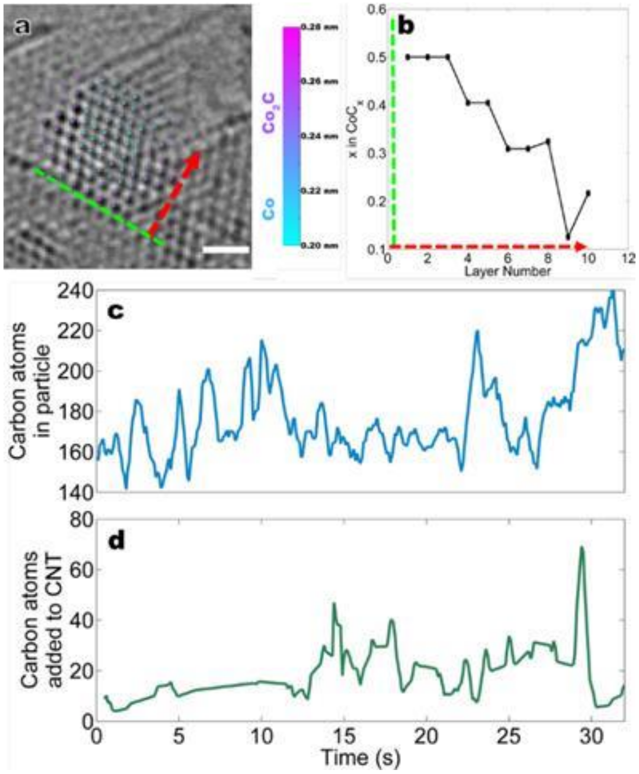

Figure 7.2 Experimentally measured, spatial (layer-wise) and temporal variations in carbon content in the nanoparticle and the growing SWCNT. (a) A single high resolution frame after applying IPS showing the location of atomic columns, where inter-atomic column distances ranging 0.20 nm to 0.22 nm or 0.23 nm to 0.26 nm correspond to Co or Co_2C, respectively. 1st atomic layer of the catalyst particle is in contact with MgO support (green dashed line), and the 10th layer is inside the SWCNT. Atomic layers are numbered 1 to 10 away from the green line. The scale bar represents 1 nm. (b) Corresponding local ratios of carbon and Co as a function of atomic layer. (c) Number of carbon atoms in the catalyst particle $C_p(t)$; and (d) the number of carbon atoms added to growing nanotube plotted as a function of time. A moving average of 10 frames is applied to smooth the data (raw data in Figure E.8).

The carbon amount in the catalyst particle and in the tube at specific time intervals can be compared from the data provided in Figures 7.2c and 7.2d. As the number of carbon atoms added to the tube increases in the time period between 10.0 s to 15 s (Figures 7.2d), $C_p(t)$ decreases (Figure 7.2c). On the other hand, $C_p(t)$ increases until 23.8 s while the tube growth rate decreases to a local minimum. These comparisons suggest that the variations in the particle composition, *i.e.* low and high carbon concentration, in the measured time period might be inversely related to SWCNT growth rate (Figures 7.2c-d). The complementary character of the fluctuations in SWCNT growth rate and particle carbon content implies that fluctuations in the SWCNT growth could be related to the periods of carbide formation and carbide decomposition.

7.4.2 Reactive Molecular Dynamics

In order to better relate the carbide formation and decomposition reactions to the tube growth, we examine the trajectories of individual C atoms in a Co nanoparticle by reactive molecular dynamics simulations (RMD) and identify the role of different types of C atoms and their contribution to the growth process. The RMD simulations were performed on a model 1.8 nm diameter Co_2C particle deposited on a rectangular monolayer substrate in an atmosphere of a C precursor gas model ($P \approx 18{,}000$ Pa, Figure 7.3a). The particle size was intentionally kept smaller and the reaction conditions, such as carbon precursor pressure, more aggressive in the simulations than in the experiment in order to decrease the calculation time needed to observe complete events from the simulations. We note that recent advances on accelerated molecular dynamics and hyperdynamics simulations have been reported and new methodologies are currently being developed such as collective variable-driven hyperdynamics (CVHD) [246] or hybrid approaches that combine reactive molecular dynamics with time-stamp force-bias Monte Carlo simulations[247], both of which could satisfactorily reproduce the dynamic behavior of reactive systems up to time scales of seconds without altering reaction conditions. Previous studies using the current approach have shown that the mechanisms of nucleation and growth are the same for different particle sizes.[55] The kinetics are also analogous for different particle sizes [54] and the carbon precursor concentration. [237] Thus, we can qualitatively compare our simulations to the experiment results. Using a dissolution residence-time criterion, as reported previously,[54] C atoms can be classified into three types: 1) atoms that are predominantly involved in diffusion on the particle surface (SD), or 2) in the bulk (BD) before becoming part of the growing nanotube structure or 3) atoms that remain dissolved in the nanoparticle for prolonged periods of time, which makes them candidates for participation in carbide formation (CF) (Figure E.1).

After the nanotube cap is formed and the nucleation stage concluded, the carbon concentration in each atomic layer is obtained by calculating the ratio of z-density profiles for each atomic species (Co and C) in each layer (Figure E.2). The C:Co ratios from each atomic layer are averaged over 5 ns in three different reaction time zones (35 ns to 40 ns, 40 ns to 45ns and 45 ns to 50 ns). In each time zone, the ratio decreases linearly along the normal away from the substrate plane (direction guided by the arrow in Figure 7.3a) from 0.8 to 0.2, and stabilizes in the 4th layer at approximately 0.2 (Figure 7.3b). It is noted that the carbon concentration profile corresponding to the growth stage (Figure 7.3b) has similarity with that of the nucleation stage reported in our earlier work[177], which indicates that such carbon gradient starts to be generated at earlier times and consolidates at the growth stage. This analysis does not include the pure metal layer in contact with the support, as C atoms undergo repulsion from the support and the first peak of C atoms from the z-density profiles is located closer to the second Co peak than to the first one (Figure E.2). Although the particle size is smaller in the simulation than in the experiments, both of them show that carbon stays inside the particle, and the C:Co ratio drops moving perpendicularly away from the substrate plane and remains at ≈ 0.2 in the particle region located inside the growing SWCNT (Figures 7.2b and 7.3b). For the layer that is in contact with the substrate, the C:Co ratio can be as high as 0.75 in the simulation, which includes SD, BD and CF types of C atoms. This ratio is restricted to a maximum value of 0.5 in the experimental measurements, as from the images we can only identify the carbon amount associated with the Co_2C phase and not the dissolved C atoms, if present. Moreover, the C:Co ratio for each atomic layer in time zone 45 ns to 50 ns is generally lower than those for the other two time zones; especially the ratio in layer 4 (≈ 0.1 in 45 ns to 50 ns time zone) implying that the total carbon amount in the particle varies during SWCNT growth, which agrees with our experimental results.

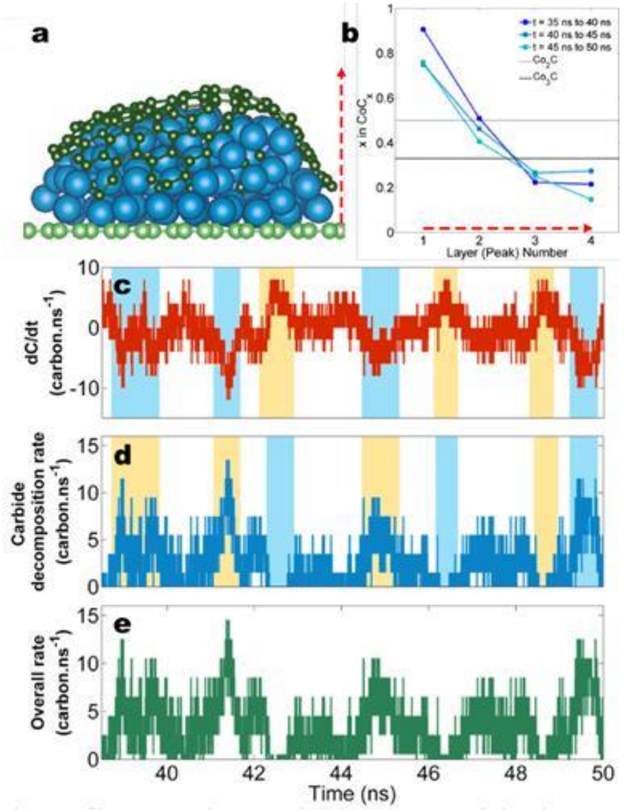

Figure 7.3 Simulated spatial (layer-wise) and temporal variations in carbon content in the nanoparticle and the growing SWCNT. (a) Simulated catalyst particle (on a support) that nucleates a SWCNT with atomic layers from 1 to 4 numbered in the direction of the red arrow. (b) Corresponding ratios of carbon and metal as a function of each atomic layer at different time intervals (35 ns to 40 ns, 40 ns to 45 ns, 45 ns to 50 ns). The values are obtained from z-density profiles reported in Appendix E information (Figure E.1. (c) Variation in the number of carbon atoms in the particle with time. (d) Carbide decomposition rate, r_1, estimated from an atomic balance of carbon atoms in the particle (eq 7.4) *versus* time. Yellow or light blue regions indicate an increase or decrease, respectively, in either growth rate or carbon concentration in the particle. (e) Nanotube growth rate (surface diffusion contribution not included) estimated directly from the total number of atoms that leave the particle *versus* time.

To further examine the role of carbide in nanotube growth, a thorough atomic balance of C atoms from the RMD trajectories is performed. The C atomic balance equation (eq 7.4) shows that the carbide decomposition rate, r_1, is a function of three components.

They are the carbon dissolution (carbide formation) rate, r_2, (Figure E.3), the variation of C content in the particle with time, dC/dt, and C diffusion across the C gradient in the particle, $D_c(\nabla^2 C)$ (Figure E.3).

$$r_1 = r_2 + \frac{dC}{dt} - D_C\left(\nabla^2 C\right) \tag{7.4}$$

As estimated from the RMD trajectories, the carbon atoms rate (r_2) is 1.50 $\cdot\mathrm{ns}^{-1}$ (Figure E.4a, we note that rates reported from RMD calculations are much larger than actual experimental rates due to the accelerated nature of these simulations). In contrast, dC/dt exhibits a fluctuating behavior in agreement with experimental observations (Figures 7.3c and 7.2c, respectively). Molecular transport of C atoms inside the particle is described in equation 4 as the product of the diffusion coefficient of atomic carbon in the particle multiplied by the variation of the carbon concentration gradient across the nanoparticle. The diffusion term (D_c) is estimated from the mean-squared displacement and Einstein's diffusivity equation (Figures E.4b). The variation of the carbon gradient in the direction perpendicular to the substrate is estimated from the C composition profiles by fitting the curves in Figure 7.3b to a quadratic function and analytically calculating the second derivative with respect to position in the z-direction. We find that the diffusion coefficient is $(1.29 \pm 0.07) \times 10^{-11}$ $\mathrm{m}^2\cdot\mathrm{s}^{-1}$, which is in agreement with reported diffusion coefficients of C dissolved in transition metals such as Ni (ranging between $10^{-11}\mathrm{m}^2\cdot\mathrm{s}^{-1}$ and $10^{-10}\mathrm{m}^2\cdot\mathrm{s}^{-1}$),[55] and the second derivative of the carbon concentration per nm^2 varies between 0.14 carbon atoms and 0.23 C atoms. Thus, by knowing r_2, dC/dt and $D_c(\nabla^2 C)$, r_1 is obtained *via* equation 4 as a function of time (Figure 7.3d). In addition to obtaining the rates of carbide decomposition (r_1), the overall tube growth rate is also determined by monitoring independently the carbon atoms that leave the particle (Figure 7.3e). Despite the accelerated dynamics intrinsic to our simulation model, the results obtained are in qualitative agreement with experimental measurements. The calculated r_1 has the same fluctuations as the tube growth and its value is consistently lower than that of the tube growth by approximately 2 carbon atoms per ns. This observation is in qualitative agreement with experimental results (Table S2), which find the number of carbon atoms integrated into the SWCNT to be larger than the number of carbon atoms ejected from the bulk of the particle by a factor of 2. This implies that the carbon from the carbide decomposition is forming the tube and the difference suggests that another C source is contributing to the tube growth.

RMD simulations show that a considerable percentage of C atoms in the catalytic process participate in surface diffusion, which fluctuates between 15 % and 55 % (Figure E.1). Some of these carbon atoms diffusing on the surface may become part of the nanotube as a function of time as illustrated in Figure 7.4. The growth rate due to surface diffusion is estimated to be 1.03 carbon atoms$\cdot$ns^{-1} from the slope of the straight line that fits the data. These results indicate a constant addition of C atoms to the nanotube from C atoms diffusing on the surface, in contrast to the fluctuating behavior originating from C atoms diffusing out of the particle bulk.

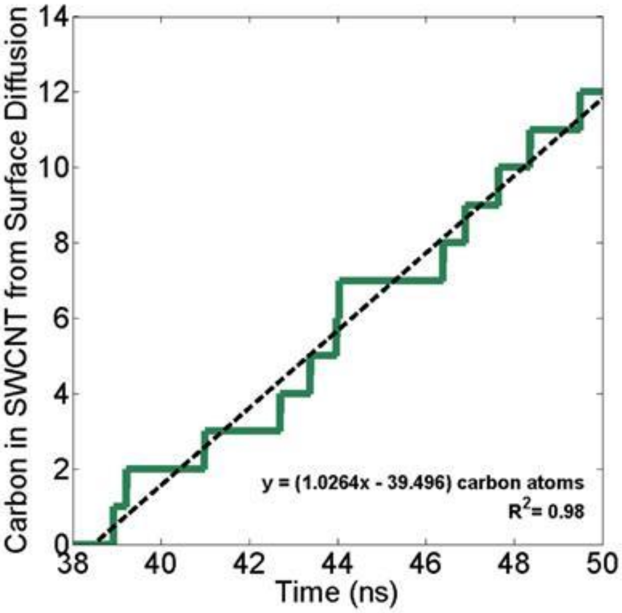

Figure 7.4 Simulated number of surface diffusing carbon atoms added to SWCNT *versus* time. The rate of growth due to surface diffusion is estimated to be the slope of a straight line fit to the data relating the number of surface carbon atoms incorporated into the nanotube and time. The fit has a coefficient of determination of 0.98.

7.5 Conclusions

To summarize, both atomic-resolution images and RMD simulations show that two distinct phases; Co and Co-carbide phases co-exist in a single catalyst particle during SWCNT growth. The carbon-rich phase (carbide) is generally in contact with the support (MgO), and the carbon-poor Co is away from the support and in contact with the SWCNT rim. We propose that the carbon feedstock from the precursor decomposes at the catalyst surface, and part of the resulting carbon diffuses into the particle to form metal carbide. Once the tube forms and partially covers the particle surface, the carbon may not be able to diffuse into the particle efficiently, making the carbide phase unstable. Therefore, a carbon-depleted region that is covered by the tube rim is present during growth. Such a carbon gradient acts as a driving force causing carbon atoms to diffuse over the particle towards the surface. This resolves the mechanism of carbon diffusion in particle sizes below 5 nm. This mechanism is in contrast with the one previously proposed by Baker *et al*., who suggest that the driving force of carbon diffusion is due to a temperature gradient, despite the fact that it is very difficult to sustain any significant temperature gradient in such small particles.[32] In the real-time videos, volume ratios of these two phases change as a function of time, consistent with the fluctuating measured SWCNT growth rate. The simulations indicate that the rate of tube formation from surface diffusion is constant, while the fluctuating growth observed both experimentally and in simulation suggests that bulk processes within the particle are important. By employing automated image analysis of the large data set (generated by the real-time atomic-resolution videos), we provide first quantitative experimental evidence that the carbon concentration profile developed inside the catalyst is a critical determinant in tube formation, and that the tube growth rate depends on the rates of carbide formation and decomposition. These results are further corroborated by RMD simulations. We also show that this new approach to probe the atomic scale mechanisms for heterogeneous catalysis.

CHAPTER VIII

CONCLUSIONS AND RECOMMENDATIONS

Various aspects of the catalytic synthesis of single-walled carbon nanotubes on transition metal nanoparticles were studied by combining atomistic simulations at the RMD, DFT, and AIMD levels with *in situ* experimental observations. The evolution of the catalyst as it facilitates the assembling of C into a curved honeycomb lattice was studied to understand its role in shaping the nanotube structure. Beginning with adsorption, dissolution and nucleation of carbon on the catalyst surface, we study the complex interactions between the catalytic particle with the nascent nanotube and with the support. Carbon transport and transformations in the structure and composition of the nanoparticle were monitored as nucleation of the nanotube and growth occurred. The most significant findings of this study are summarized below.

Evidence in favor of the possibility of a carbide phase being present in Ni nanoparticles during nucleation and growth of SWCNTs was obtained using DFT and AIMD simulations where: a) the energetically favorable dissolution of carbon occurs at the interstitial sites of the nanoparticle at the synthesis conditions, b) dissolved C atoms do not form bonds inside the catalyst, and c) C atoms inside the particle remain dissolved at low C concentrations while the growing nanotube is attached to the particle. The interactions between the nanotube and the catalyst were characterized by charge transfer from surface Ni atoms to C atoms at the nanotube rim. Regions of accumulation of electron density were located at the nanotube-catalyst interface and the nanotube rim, while regions of depletion were located near surface Ni atoms in contact with the nanotube, and C atoms in the vicinity of the nanotube rim. This electron density distribution explains the high reactivity of Ni and C atoms located at the interface and the flexibility of C-C bonds to rearrange and heal structural defects while they remain in the vicinity of the interface. A contrast between carburized Ni particles and pure Ni nanoparticles showed a greater electron density transfer for the carburized particle, indicating the possibility of different interactions and reactivity for particles with varying content of C dissolved.

Favorable adsorption and limited C solubility in the catalytic particle was determined from DFT simulations of carbon interacting with a noble metal catalyst (Rh). The energy of interaction of each successive addition of carbon to Rh nanoparticles is constant and independent of particle size (for small Rh particles ~0.8 nm to 1.1 nm), geometry and type of support (either OH-terminated MgO(111), or Mg- and O-terminated MgO(100)). Nevertheless carbon solubility is affected by particle size and the presence of the MgO support, with smaller unsupported particles allowing a slightly higher amount of carbon dissolved in their structure. The interaction of the particle with the individual C atoms added and with the (100) and (111) terminations of MgO is characterized by electron density accumulated at the particle support interface and electron transfer from surface Rh atoms to adsorbed and dissolved C atoms. Factors such as amount of carbon near the interface, type or surface termination of the support, and the degree of particle-support epitaxial match were found to influence the extent of the charge transfer and the overall particle-support adhesion. Particles with higher C content near the interface and C atoms, higher degree of epitaxial match with the support, and deposited on the (100) facet of MgO tend to interact more strongly with the support. A graphene seed placed on the Rh particle surface shows a stronger adhesion to the particle without carbon dissolved and deposited on the MgO(111) facet. In contrast, the adhesion of the particle to the support decreases in the presence of the nucleating nanotube and it tends to increase when individual C atoms are deposited on or absorbed in the nanoparticle. These results indicate the possibility of modifying the catalyst structure and interactions with the nanotube by selecting the particle support, and providing conditions to change its composition.

ETEM measurements of the structure of MgO-supported Co carbide revealed that surface termination and surface local C composition of the catalyst affect the catalyst-nanotube interactions during nucleation. Investigations of this phenomenon using DFT simulations demonstrated that the nanotube seed remains flat and more strongly attached to Co terminated surface facets than C-containing ones, where detachment and curvature of the nanotube seed is observed. We propose that this disparity between facets is essential for CNT growth, as it offers the necessary combination of anchoring and lift-off sites. This favors the conversion of the graphene nucleus into a nanotube and prevents nanoparticles from encapsulating, which is one of the major causes of catalyst deactivation and reduction in CNT synthesis yield.

Reactive molecular dynamics simulations and *in situ* ETEM of the nucleation of single walled carbon on CoxC/MgO particles provided detailed information about the evolution of the nanoparticle structure and composition. Come of the changes observed during the initial stages include the expansion of the particle on the support as C dissolves, flattening during nucleation of the nascent nanotube, and elongation as the nanotube cap lifts off the catalyst surface. Carbon transport in and out of the particle establishes a constant gradient along the catalyst particle in the direction perpendicular to the support plane. The first catalyst layer in contact with the support is made out of metal atoms, followed by metal layers with a relatively high C concentration that gradually decreases towards the particle surface. The results from experiment and simulations show agreement and validation of the RMD methodology used.

Further extension of the RMD and ETEM analyses into the growth stage demonstrates the stability of the C gradient established during the nucleation stage. Moreover, two distinct phases coexisting in the nanoparticle are identified: a carbide phase in contact with the support and a metal phase in contact with the growing nanotube. C dissolved near the interface with the nanotube is depleted as it bonds to the nanotube structure. Some C atoms remain dissolved in the carbide region for a long time, while others diffuse through the particle toward the carbon-depleted region to become part of the nanotube. The identified carbide and metal regions fluctuate in size as nanotube growth proceeds indicating the continuous formation and decomposition of a metastable carbide phase in the nanoparticle during growth. The rate of tube formation due to surface diffusion estimated from RMD simulations is constant, while a fluctuating growth rate observed both experimentally and in simulation suggests that both surface and bulk processes within the particle are important. These results show that the tube growth rate is affected by the rates of metastable carbide formation and decomposition.

Considering the results presented in this dissertation, a general recommendation is the continued characterization of the catalyst nanoparticle transformations and interactions with the growing nanotube combining molecular simulations and *in situ* measurements. Specific recommendations for future work are outlined below.

•Implementation of methodologies that allow the simulated growth of SWCNTs at time scales that resemble the observed rates in experiments will provide a more direct comparison and evidence of nucleation and growth mechanisms presented in this work and proposed in the future. Algorithms that can potentially reach such time scales include: accelerated molecular dynamics and hyperdynamics, and hybrid approaches such as RMD + time-stamp force-biased Monte Carlo simulations.

•Development and implementation of force fields and models within the RMD framework that would allow an explicit representation of the support, given the impact that it can have on the selective growth of carbon nanotubes, as previously reported in the literature and as discussed in the present work.

•SWCNTs for some applications, such as their use in electronics, are required to be grown as forests or bundles with similar electrical properties and highly aligned in some cases. The collective effect that nanotubes growing in close proximity can have on the individual structure and orientation of each nanotube can be investigated using ETEM and multiscale modeling approaches, from the DFT level to understand interactions involving electron transfer to RMD and other approaches to simulate models with large numbers of atoms.

•Selective growth of SWCNTs has been successfully achieved using bimetallic catalysts, which can combine the activity of two different metals and other physical properties such as high melting point, to yield nanoparticles with desired catalytic and stable structural features at the reaction conditions. The combined use of molecular simulations such as DFT, AIMD, RMD, and others with *in situ* measurements of bimetallic catalysts can provide valuable information to formulate mechanisms that explain the performance obtained with these catalysts and propose new catalysts with improved activity and selectivity for the growth of SWCNTs.

•Modification of the catalyst surface to change the catalytic activity can be applied during the catalyst preparation or occur due to adsorption of reaction products of the C precursor gas decomposition, such as H or O, depending on the reactants used. The effect of functionalization of the catalyst surface and interfaces with the nanotube and with the support on nucleation of SWCNTs can be investigated using DFT and AIMD simulations.

REFERENCES

1. Iijima, S., Helical microtubules of graphitic carbon. *Nature* **1991,** *354* (6348), 56-58.

2. De Volder, M. F.; Tawfick, S. H.; Baughman, R. H.; Hart, A. J., Carbon nanotubes: present and future commercial applications. *Science* **2013,** *339* (6119), 535-539.

3. Karami, M.; Bahabadi, M. A.; Delfani, S.; Ghozatloo, A., A new application of carbon nanotubes nanofluid as working fluid of low-temperature direct absorption solar collector. *Solar Energy Materials and Solar Cells* **2014,** *121*, 114-118.

4. Kim, J.-K.; Kim, Y.; Park, S.; Ko, H.; Kim, Y., Encapsulation of organic active materials in carbon nanotubes for application to high-electrochemical-performance sodium batteries. *Energy & Environmental Science* **2016,** *9* (4), 1264-1269.

5. Han, S.-J., Toward high-performance electronics based on carbon nanomaterials, 2016 *IEEE International Conference on Electron Devices and Solid-State Circuits (EDSSC)*, IEEE: **2016**, *1*, 161-164.

6. Park, S.; Vosguerichian, M.; Bao, Z., A review of fabrication and applications of carbon nanotube film-based flexible electronics. *Nanoscale* **2013,** *5* (5), 1727-1752.

7. Chou, T.-W.; Gao, L.; Thostenson, E. T.; Zhang, Z.; Byun, J.-H., An assessment of the science and technology of carbon nanotube-based fibers and composites. *Composites Science and Technology* **2010,** *70* (1), 1-19.

8. Liu, X.; Wang, M.; Zhang, S.; Pan, B., Application potential of carbon nanotubes in water treatment: a review. *Journal of Environmental Sciences* **2013,** *25* (7), 1263-1280.

9. Chen, Z.; Tabakman, S. M.; Goodwin, A. P.; Kattah, M. G.; Daranciang, D.; Wang, X.; Zhang, G.; Li, X.; Liu, Z.; Utz, P. J., Protein microarrays with carbon nanotubes as multicolor Raman labels. *Nature Biotechnology* **2008,** *26* (11), 1285-1292.

10. Gomez-Gualdron, D. A.; Burgos, J. C.; Yu, J.; Balbuena, P. B., Carbon nanotubes: engineering biomedical applications. *Progress in Molecular Biology and Translational Science* **2010,** *104*, 175-245.

11. Eatemadi, A.; Daraee, H.; Karimkhanloo, H.; Kouhi, M.; Zarghami, N.; Akbarzadeh, A.; Abasi, M.; Hanifehpour, Y.; Joo, S. W., Carbon nanotubes: properties, synthesis, purification, and medical applications. *Nanoscale Research Letters* **2014,** *9* (1), 393.

12. Avouris, P., Molecular electronics with carbon nanotubes. *Accounts of Chemical Research* **2002,** *35* (12), 1026-1034.

13. Charlier, J.-C.; Blase, X.; Roche, S., Electronic and transport properties of nanotubes. *Reviews of Modern Physics* **2007,** *79* (2), 677.

14. Saito, R.; Dresselhaus, G.; Dresselhaus, M., Trigonal warping effect of carbon nanotubes. *Physical Review B* **2000,** *61* (4), 2981.

15. Jourdain, V.; Bichara, C., Current understanding of the growth of carbon nanotubes in catalytic chemical vapour deposition. *Carbon* **2013,** *58*, 2-39.

16. Yang, F.; Wang, X.; Li, M.; Liu, X.; Zhao, X.; Zhang, D.; Zhang, Y.; Yang, J.; Li, Y., Templated Synthesis of Single-Walled Carbon Nanotubes with Specific Structure. *Accounts of Chemical Research* **2016,** *49* (4), 606-615.

17. Journet, C.; Maser, W.; Bernier, P.; Loiseau, A.; De La Chapelle, M. L.; Lefrant, d. l. S.; Deniard, P.; Lee, R.; Fischer, J., Large-scale production of single-walled carbon nanotubes by the electric-arc technique. *Nature* **1997,** *388* (6644), 756-758.

18. Scott, C. D.; Arepalli, S.; Nikolaev, P.; Smalley, R. E., Growth mechanisms for single-wall carbon nanotubes in a laser-ablation process. *Applied Physics A* **2001,** *72* (5), 573-580.

19. Moisala, A.; Nasibulin, A. G.; Kauppinen, E. I., The role of metal nanoparticles in the catalytic production of single-walled carbon nanotubes—a review. *Journal of Physics: Condensed Matter* **2003,** *15* (42), S3011.

20. Lamouroux, E.; Serp, P.; Kalck, P., Catalytic routes towards single wall carbon nanotubes. *Catalysis Reviews* **2007,** *49* (3), 341-405.

21. Hiraoka, T.; Bandow, S.; Shinohara, H.; Iijima, S., Control on the diameter of single-walled carbon nanotubes by changing the pressure in floating catalyst CVD. *Carbon* **2006,** *44* (9), 1853-1859.

22. Magrez, A.; Smajda, R.; Seo, J. W.; Horvath, E.; Ribič, P. R.; Andresen, J. C.; Acquaviva, D.; Olariu, A.; Laurenczy, G.; Forró, L. s., Striking influence of the catalyst support and its acid–base properties: new insight into the growth mechanism of carbon nanotubes. *ACS Nano* **2011,** *5* (5), 3428-3437.

23. Bachilo, S. M.; Balzano, L.; Herrera, J. E.; Pompeo, F.; Resasco, D. E.; Weisman, R. B., Narrow (n, m)-distribution of single-walled carbon nanotubes grown using a solid supported catalyst. *Journal of the American Chemical Society* **2003,** *125* (37), 11186-11187.

24. Lolli, G.; Zhang, L.; Balzano, L.; Sakulchaicharoen, N.; Tan, Y.; Resasco, D. E., Tailoring (n, m) structure of single-walled carbon nanotubes by modifying reaction conditions and the nature of the support of CoMo catalysts. *The Journal of Physical Chemistry B* **2006,** *110* (5), 2108-2115.

25. Fouquet, M.; Bayer, B. C.; Esconjauregui, S.; Blume, R.; Warner, J.; Hofmann, S.; Schlögl, R.; Thomsen, C.; Robertson, J., Highly chiral-selective growth of single-walled carbon nanotubes with a simple monometallic Co catalyst. *Physical Review B* **2012,** *85* (23), 235411.

26. He, M.; Jiang, H.; Liu, B.; Fedotov, P. V.; Chernov, A. I.; Obraztsova, E. D.; Cavalca, F.; Wagner, J. B.; Hansen, T. W.; Anoshkin, I. V., Chiral-selective growth of single-walled carbon nanotubes on lattice-mismatched epitaxial cobalt nanoparticles. *Scientific Reports* **2013,** *3*, 1460.

27. Yang, F.; Wang, X.; Zhang, D.; Yang, J.; Luo, D.; Xu, Z.; Wei, J.; Wang, J.-Q.; Xu, Z.; Peng, F., Chirality-specific growth of single-walled carbon nanotubes on solid alloy catalysts. *Nature* **2014,** *510* (7506), 522-524.

28. Yang, F.; Wang, X.; Zhang, D.; Qi, K.; Yang, J.; Xu, Z.; Li, M.; Zhao, X.; Bai, X.; Li, Y., Growing zigzag (16, 0) carbon nanotubes with structure-defined catalysts. *Journal of the American Chemical Society* **2015,** *137* (27), 8688-8691.

29. Yang, F.; Wang, X.; Si, J.; Zhao, X.; Qi, K.; Jin, C.; Zhang, Z.; Li, M.; Zhang, D.; Yang, J.; Zhang, Z.; Xu, Z.; Peng, L.-M.; Bai, X.; Li, Y., Water-Assisted Preparation of High-Purity Semiconducting (14,4) Carbon Nanotubes. *ACS Nano* **2016**, *11*(1), 186-193.

30. Dai, H.; Rinzler, A. G.; Nikolaev, P.; Thess, A.; Colbert, D. T.; Smalley, R. E., Single-wall nanotubes produced by metal-catalyzed disproportionation of carbon monoxide. *Chemical Physics Letters* **1996,** *260* (3), 471-475.

31. Bladh, K.; Falk, L.; Rohmund, F., On the iron-catalysed growth of single-walled carbon nanotubes and encapsulated metal particles in the gas phase. *Applied Physics A* **2000,** *70* (3), 317-322.

32. Zhao, J.; Martinez-Limia, A.; Balbuena, P., Understanding catalysed growth of single-wall carbon nanotubes. *Nanotechnology* **2005,** *16* (7), S575.

33. Balbuena, P. B.; Zhao, J.; Huang, S.; Wang, Y.; Sakulchaicharoen, N.; Resasco, D. E., Role of the catalyst in the growth of single-wall carbon nanotubes. *Journal of Nanoscience and Nanotechnology* **2006,** *6* (5), 1247-1258.

34. Gómez-Gualdrón, D. A.; Balbuena, P. B., The role of cap chirality in the mechanism of growth of single-wall carbon nanotubes. *Nanotechnology* **2008,** *19* (48), 485604.

35. Gómez-Gualdrón, D. A.; Balbuena, P. B., Effect of metal cluster-cap interactions on the catalyzed growth of single-wall carbon nanotubes. *The Journal of Physical Chemistry C* **2008,** *113* (2), 698-709.

36. Reich, S.; Li, L.; Robertson, J., Control the chirality of carbon nanotubes by epitaxial growth. *Chemical Physics Letters* **2006,** *421* (4–6), 469-472.

37. Reich, S.; Li, L.; Robertson, J., Epitaxial growth of carbon caps on Ni for chiral selectivity. *Physica Status Solidi (b)* **2006,** *243* (13), 3494-3499.

38. Gomez-Gualdron, D. A.; McKenzie, G. D.; Alvarado, J. F.; Balbuena, P. B., Dynamic evolution of supported metal nanocatalyst/carbon structure during single-walled carbon nanotube growth. *ACS Nano* **2011,** *6* (1), 720-735.

39. Neyts, E. C.; van Duin, A. C.; Bogaerts, A., Changing chirality during single-walled carbon nanotube growth: a reactive molecular dynamics/Monte Carlo study. *Journal of the American Chemical Society* **2011,** *133* (43), 17225-17231.

40. Wagner, R.; Ellis, W., Vapor-liquid-solid mechanism of single crystal growth. *Applied Physics Letters* **1964,** *4* (5), 89-90.

41. Baker, R.; Barber, M.; Harris, P.; Feates, F.; Waite, R., Nucleation and growth of carbon deposits from the nickel catalyzed decomposition of acetylene. *Journal of Catalysis* **1972,** *26* (1), 51-62.

42. Baker, R.; Harris, P.; Thomas, R.; Waite, R., Formation of filamentous carbon from iron, cobalt and chromium catalyzed decomposition of acetylene. *Journal of Catalysis* **1973,** *30* (1), 86-95.

43. Kukovitsky, E. F.; L'Vov, S. G.; Sainov, N. A., VLS-growth of carbon nanotubes from the vapor. *Chemical Physics Letters* **2000,** *317* (1–2), 65-70.

44. Helveg, S.; Lopez-Cartes, C.; Sehested, J.; Hansen, P. L.; Clausen, B. S.; Rostrup-Nielsen, J. R.; Abild-Pedersen, F.; Nørskov, J. K., Atomic-scale imaging of carbon nanofibre growth. *Nature* **2004,** *427* (6973), 426-429.

45. Takagi, D.; Kobayashi, Y.; Hibino, H.; Suzuki, S.; Homma, Y., Mechanism of gold-catalyzed carbon material growth. *Nano Letters* **2008,** *8* (3), 832-835.

46. Page, A. J.; Yamane, H.; Ohta, Y.; Irle, S.; Morokuma, K., QM/MD simulation of SWNT nucleation on transition-metal carbide nanoparticles. *Journal of the American Chemical Society* **2010,** *132* (44), 15699-15707.

47. Ding, F.; Bolton, K.; Rosen, A., Nucleation and growth of single-walled carbon nanotubes: A molecular dynamics study. *The Journal of Physical Chemistry B* **2004,** *108* (45), 17369-17377.

48. Shariat, M.; Shokri, B.; Neyts, E. C., On the low-temperature growth mechanism of single walled carbon nanotubes in plasma enhanced chemical vapor deposition. *Chemical Physics Letters* **2013,** *590*, 131-135.

49. Zhang, S.; Tong, L.; Hu, Y.; Kang, L.; Zhang, J., Diameter-specific growth of semiconducting SWNT arrays using uniform Mo2C solid catalyst. *Journal of the American Chemical Society* **2015,** *137* (28), 8904-8907.

50. Yoshida, H.; Takeda, S.; Uchiyama, T.; Kohno, H.; Homma, Y., Atomic-scale *in-situ* observation of carbon nanotube growth from solid state iron carbide nanoparticles. *Nano Letters* **2008,** *8* (7), 2082-2086.

51. Hofmann, S.; Sharma, R.; Ducati, C.; Du, G.; Mattevi, C.; Cepek, C.; Cantoro, M.; Pisana, S.; Parvez, A.; Cervantes-Sodi, F., *In situ* observations of catalyst dynamics during surface-bound carbon nanotube nucleation. *Nano Letters* **2007,** *7* (3), 602-608.

52. Nanda, K.; Sahu, S.; Behera, S., Liquid-drop model for the size-dependent melting of low-dimensional systems. *Physical Review A* **2002,** *66* (1), 013208.

53. Homma, Y.; Kobayashi, Y.; Ogino, T.; Takagi, D.; Ito, R.; Jung, Y. J.; Ajayan, P. M., Role of transition metal catalysts in single-walled carbon nanotube growth in chemical vapor deposition. *The Journal of Physical Chemistry B* **2003,** *107* (44), 12161-12164.

54. Gomez-Gualdron, D. A.; Balbuena, P. B., Characterization of Carbon Atomistic Pathways during Single-Walled Carbon Nanotube Growth on Supported Metal Nanoparticles. *Carbon* **2013,** *57*, 298-309.

55. Gómez-Gualdrón, D. A.; Beetge, J. M.; Balbuena, P. B., Characterization of Metal Nanocatalyst State and Morphology during Simulated Single-Walled Carbon Nanotube Growth. *The Journal of Physical Chemistry C* **2013,** *117* (23), 12061-12070.

56. Yasuda, H.; Mori, H., Phase diagrams in nanometer-sized alloy systems. *Journal of Crystal Growth* **2002,** *237*, 234-238.

57. Srivastava, C., Nano-size and miscibility gap. *Advanced Materials Research, Trans Tech Publications* **2012**, *585*, 8-13.

58. Sutter, E. A.; Sutter, P. W., Giant carbon solubility in Au nanoparticles. *Journal of Materials Science* **2011,** *46* (22), 7090.

59. He, M.; Amara, H.; Jiang, H.; Hassinen, J.; Bichara, C.; Ras, R. H.; Lehtonen, J.; Kauppinen, E. I.; Loiseau, A., Key roles of carbon solubility in single-walled carbon nanotube nucleation and growth. *Nanoscale* **2015,** *7* (47), 20284-20289.

60. Lin, M.; Ying Tan, J. P.; Boothroyd, C.; Loh, K. P.; Tok, E. S.; Foo, Y.-L., Direct observation of single-walled carbon nanotube growth at the atomistic scale. *Nano Letters* **2006,** *6* (3), 449-452.

61. Wirth, C.; Hofmann, S.; Robertson, J., State of the catalyst during carbon nanotube growth. *Diamond and Related Materials* **2009,** *18* (5), 940-945.

62. Kumar, M.; Ando, Y., Chemical vapor deposition of carbon nanotubes: a review on growth mechanism and mass production. *Journal of Nanoscience and Nanotechnology* **2010,** *10* (6), 3739-3758.

63. Deck, C. P.; Vecchio, K., Prediction of carbon nanotube growth success by the analysis of carbon–catalyst binary phase diagrams. *Carbon* **2006,** *44* (2), 267-275.

64. Andrievsky, R.; Gurov, K., Self-diffusion in interstitial phases. *The Physics of Metals and Metallography* **1968,** *26* (5), 48-52.

65. Bridge, M.; Prior, K.; Lambert, R., The effects of surface carbide formation on the adsorption-desorption kinetics of CO on smooth and stepped cobalt surfaces. *Surface Science Letters* **1980,** *97* (1), L325-L329.

66. Didziulis, S. V.; Frantz, P.; Fernandez-Torres, L. C.; Guenard, R. L.; El-bjeirami, O.; Perry, S. S., Coordination chemistry of transition metal carbide surfaces: detailed spectroscopic and theoretical investigations of CO adsorption on TiC and VC (100) surfaces. *The Journal of Physical Chemistry B* **2001,** *105* (22), 5196-5209.

67. Alvarez, W. E.; Kitiyanan, B.; Borgna, A.; Resasco, D. E., Synergism of Co and Mo in the catalytic production of single-wall carbon nanotubes by decomposition of CO. *Carbon* **2001,** *39* (4), 547-558.

68. Stolojan, V.; Tison, Y.; Chen, G. Y.; Silva, R., Controlled growth-reversal of catalytic carbon nanotubes under electron-beam irradiation. *Nano Letters* **2006,** *6* (9), 1837-1841.

69. He, Z.; Maurice, J.-L.; Gohier, A.; Lee, C. S.; Pribat, D.; Cojocaru, C. S., Iron catalysts for the growth of carbon nanofibers: Fe, Fe3C or both? *Chemistry of Materials* **2011,** *23* (24), 5379-5387.

70. Ding, F.; Larsson, P.; Larsson, J. A.; Ahuja, R.; Duan, H.; Rosén, A.; Bolton, K., The importance of strong carbon− metal adhesion for catalytic nucleation of single-walled carbon nanotubes. *Nano Letters* **2008,** *8* (2), 463-468.

71. Fan, X.; Buczko, R.; Puretzky, A. A.; Geohegan, D. B.; Howe, J. Y.; Pantelides, S. T.; Pennycook, S. J., Nucleation of single-walled carbon nanotubes. *Physical Review Letters* **2003,** *90* (14), 145501.

72. Henry, C. R., Surface studies of supported model catalysts. *Surface Science Reports* **1998,** *31* (7), 231-325.

73. Page, A. J.; Ding, F.; Irle, S.; Morokuma, K., Insights into carbon nanotube and graphene formation mechanisms from molecular simulations: a review. *Reports on Progress in Physics* **2015,** *78* (3), 036501.

74. Wang, Z.-l.; Hui, C., Electron microscopy of nanotubes. *Springer Science & Business Media*, New York: **2013**.

75. Schrödinger, E., Quantisierung als eigenwertproblem. *Annalen der Physik* **1926,** *385* (13), 437-490.

76. Born, M.; Oppenheimer, R., Zur quantentheorie der molekeln. *Annalen der Physik* **1927,** *389* (20), 457-484.

77. Hohenberg, P.; Kohn, W., Inhomogeneous electron gas. *Physical Review* **1964,** *136* (3B), B864.

78. Roothaan, C. C. J., New developments in molecular orbital theory. *Reviews of Modern Physics* **1951,** *23* (2), 69.

79. Perdew, J. P.; Burke, K.; Ernzerhof, M., Generalized gradient approximation made simple. *Physical Review Letters* **1996,** *77* (18), 3865.

80. Perdew, J. P.; Chevary, J. A.; Vosko, S. H.; Jackson, K. A.; Pederson, M. R.; Singh, D. J.; Fiolhais, C., Atoms, molecules, solids, and surfaces: Applications of the generalized gradient approximation for exchange and correlation. *Physical Review B* **1992,** *46* (11), 6671.

81. Blöchl, P. E., Projector augmented-wave method. *Physical Review B* **1994,** *50* (24), 17953.

82. Kohn, W., Analytic properties of Bloch waves and Wannier functions. *Physical Review* **1959,** *115* (4), 809.

83. Rahman, A., Correlations in the motion of atoms in liquid argon. *Physical Review* **1964,** *136* (2A), A405.

84. Hermansson, K.; Lie, G. C.; Clementi, E., On velocity scaling in molecular dynamics simulations. *Journal of Computational Chemistry* **1988,** *9* (3), 200-203.

85. Berendsen, H. J.; Postma, J. v.; van Gunsteren, W. F.; DiNola, A.; Haak, J., Molecular dynamics with coupling to an external bath. *The Journal of Chemical Physics* **1984,** *81* (8), 3684-3690.

86. Hoover, W. G., Canonical dynamics: equilibrium phase-space distributions. *Physical Review A* **1985,** *31* (3), 1695.

87. Adelman, S.; Doll, J., Generalized Langevin equation approach for atom/solid-surface scattering: General formulation for classical scattering off harmonic solids. *The Journal of Chemical Physics* **1976,** *64* (6), 2375-2388.

88. Sutton, A. P.; Chen, J., Long-range Finnis–Sinclair potentials. *Philosophical Magazine Letters* **1990,** *61* (3), 139-146.

89. Martinez-Limia, A.; Zhao, J.; Balbuena, P. B., Molecular dynamics study of the initial stages of catalyzed single-wall carbon nanotubes growth: force field development. *Journal of Molecular Modeling* **2007,** *13* (5), 595-600.

90. Brenner, D. W.; Shenderova, O. A.; Harrison, J. A.; Stuart, S. J.; Ni, B.; Sinnott, S. B., A second-generation reactive empirical bond order (REBO) potential energy expression for hydrocarbons. *Journal of Physics: Condensed Matter* **2002,** *14* (4), 783.

91. Marx, D.; Hutter, J., *Ab initio* molecular dynamics: basic theory and advanced methods. *Cambridge University Press*: **2009**.

92. Sholl, D.; Steckel, J. A., Density functional theory: a practical introduction. *John Wiley & Sons*: **2011**.

93. Cao, Q.; Rogers, J. A., Ultrathin Films of Single-Walled Carbon Nanotubes for Electronics and Sensors: A Review of Fundamental and Applied Aspects. *Advanced Materials* **2009,** *21* (1), 29-53.

94. Kam, N. W. S.; O'Connell, M.; Wisdom, J. A.; Dai, H., Carbon nanotubes as multifunctional biological transporters and near-infrared agents for selective cancer cell destruction. *Proceedings of the National Academy of Sciences of the United States of America* **2005,** *102* (33), 11600-11605.

95. López-Lorente, A. I.; Simonet, B. M.; Valcárcel, M., The Potential of Carbon Nanotube Membranes for Analytical Separations. *Analytical Chemistry* **2010,** *82* (13), 5399-5407.

96. An, K. H.; Kim, W. S.; Park, Y. S.; Moon, J.-M.; Bae, D. J.; Lim, S. C.; Lee, Y. S.; Lee, Y. H., Electrochemical properties of high-power supercapacitors using single-walled carbon nanotube electrodes. *Advanced Functional Materials* **2001,** *11* (5), 387-392.

97. Tans, S. J.; Verschueren, A. R. M.; Dekker, C., Room-temperature transistor based on a single carbon nanotube. *Nature* **1998,** *393* (6680), 49-52.

98. Srivastava, N.; Banerjee, K., Performance analysis of carbon nanotube interconnects for VLSI applications, Computer-Aided Design, 2005. ICCAD-2005. *IEEE/ACM International Conference* 6-10 Nov. **2005**, 383-390.

99. Britto, P. J.; Santhanam, K. S.; Rubio, A.; Alonso, J. A.; Ajayan, P. M., Improved charge transfer at carbon nanotube electrodes. *Advanced Materials* **1999,** *11* (2), 154-157.

100. Bachilo, S. M.; Strano, M. S.; Kittrell, C.; Hauge, R. H.; Smalley, R. E.; Weisman, R. B., Structure-assigned optical spectra of single-walled carbon nanotubes. *Science* **2002,** *298* (5602), 2361-2366.

101. Treacy, M. M. J.; Ebbesen, T. W.; Gibson, J. M., Exceptionally high Young's modulus observed for individual carbon nanotubes. *Nature* **1996,** *381* (6584), 678-680.

102. Prasek, J.; Drbohlavova, J.; Chomoucka, J.; Hubalek, J.; Jasek, O.; Adam, V.; Kizek, R., Methods for carbon nanotubes synthesis-review. *Journal of Materials Chemistry* **2011,** *21* (40), 15872-15884.

103. Dresselhaus, M. S.; Dresselhaus, G.; Eklund, P. C., Science of fullerenes and carbon nanotubes: their properties and applications. *Academic Press*: **1996**.

104. Arnold, M. S.; Green, A. A.; Hulvat, J. F.; Stupp, S. I.; Hersam, M. C., Sorting carbon nanotubes by electronic structure using density differentiation. *Nature Nano* **2006,** *1* (1), 60-65.

105. Liu, H.; Nishide, D.; Tanaka, T.; Kataura, H., Large-scale single-chirality separation of single-wall carbon nanotubes by simple gel chromatography. *Nature Communications* **2011,** *2*, 309.

106. Chng, E. L. K.; Poh, H. L.; Sofer, Z.; Pumera, M., Purification of carbon nanotubes by high temperature chlorine gas treatment. *Physical Chemistry Chemical Physics* **2013,** *15* (15), 5615-5619.

107. Kong, J.; Cassell, A. M.; Dai, H., Chemical vapor deposition of methane for single-walled carbon nanotubes. *Chemical Physics Letters* **1998,** *292* (4–6), 567-574.

108. Alvarez, W. E.; Pompeo, F.; Herrera, J. E.; Balzano, L.; Resasco, D. E., Characterization of Single-Walled Carbon Nanotubes (SWNTs) Produced by CO Disproportionation on Co−Mo Catalysts. *Chemistry of Materials* **2002,** *14* (4), 1853-1858.

109. Li, Y.; Kim, W.; Zhang, Y.; Rolandi, M.; Wang, D.; Dai, H., Growth of single-walled carbon nanotubes from discrete catalytic nanoparticles of various sizes. *The Journal of Physical Chemistry B* **2001,** *105* (46), 11424-11431.

110. Huang, S.; Woodson, M.; Smalley, R.; Liu, J., Growth mechanism of oriented long single walled carbon nanotubes using "fast-heating" chemical vapor deposition process. *Nano Letters* **2004,** *4* (6), 1025-1028.

111. Page, A. J.; Ohta, Y.; Irle, S.; Morokuma, K., Mechanisms of single-walled carbon nanotube nucleation, growth, and healing determined using QM/MD methods. *Accounts of Chemical Research* **2010,** *43* (10), 1375-1385.

112. Amara, H.; Bichara, C.; Ducastelle, F., Understanding the nucleation mechanisms of carbon nanotubes in catalytic chemical vapor deposition. *Physical Review Letters* **2008,** *100* (5), 056105.

113. Zhu, H.; Suenaga, K.; Wei, J.; Wang, K.; Wu, D., A strategy to control the chirality of single-walled carbon nanotubes. *Journal of Crystal Growth* **2008,** *310* (24), 5473-5476.

114. Oberlin, A.; Endo, M.; Koyama, T., Filamentous growth of carbon through benzene decomposition. *Journal of Crystal Growth* **1976,** *32* (3), 335-349.

115. Audier, M.; Oberlin, A.; Coulon, M., Crystallographic orientations of catalytic particles in filamentous carbon; Case of simple conical particles. *Journal of Crystal Growth* **1981,** *55* (3), 549-556.

116. Koziol, K. K.; Ducati, C.; Windle, A. H., Carbon nanotubes with catalyst controlled chiral angle. *Chemistry of Materials* **2010,** *22* (17), 4904-4911.

117. Gómez-Gualdrón, D. A.; Zhao, J.; Balbuena, P. B., Nanocatalyst structure as a template to define chirality of nascent single-walled carbon nanotubes. *The Journal of Chemical Physics* **2011,** *134* (1), -.

118. Cheng, H. M.; Li, F.; Su, G.; Pan, H. Y.; He, L. L.; Sun, X.; Dresselhaus, M. S., Large-scale and low-cost synthesis of single-walled carbon nanotubes by the catalytic pyrolysis of hydrocarbons. *Applied Physics Letters* **1998,** *72* (25), 3282-3284.

119. Ci, L.; Wei, J.; Wei, B.; Liang, J.; Xu, C.; Wu, D., Carbon nanofibers and single-walled carbon nanotubes prepared by the floating catalyst method. *Carbon* **2001,** *39* (3), 329-335.

120. Fan, Y.-Y.; Kaufmann, A.; Mukasyan, A.; Varma, A., Single- and multi-wall carbon nanotubes produced using the floating catalyst method: Synthesis, purification and hydrogen up-take. *Carbon* **2006,** *44* (11), 2160-2170.

121. Picher, M.; Lin, P. A.; Gomez-Ballesteros, J. L.; Balbuena, P. B.; Sharma, R., Nucleation of Graphene and Its Conversion to Single-Walled Carbon Nanotubes. *Nano Letters* **2014,** *14* (11), 6104-6108.

122. Börjesson, A.; Bolton, K., First principles studies of the effect of nickel carbide catalyst composition on carbon nanotube growth. *The Journal of Physical Chemistry C* **2010,** *114* (42), 18045-18050.

123. Wang, Q.; Yang, S.-W.; Yang, Y.; Chan-Park, M. B.; Chen, Y., Charge transfer between metal clusters and growing carbon structures in chirality-controlled single-walled carbon nanotube growth. *The Journal of Physical Chemistry Letters* **2011,** *2* (9), 1009-1014.

124. Kresse, G.; Furthmüller, J., Efficient iterative schemes for *ab initio* total-energy calculations using a plane-wave basis set. *Physical Review B* **1996,** *54* (16), 11169.

125. Kresse, G.; Furthmüller, J., Efficiency of *ab initio* total energy calculations for metals and semiconductors using a plane-wave basis set. *Computational Materials Science* **1996,** *6* (1), 15-50.

126. Kresse, G.; Hafner, J., *Ab initio* molecular dynamics for liquid metals. *Physical Review B* **1993,** *47* (1), 558.

127. Kresse, G.; Hafner, J., *Ab initio* molecular dynamics for open-shell transition metals. *Physical Review B* **1993,** *48* (17), 13115.

128. Kresse, G.; Hafner, J., *Ab initio* molecular-dynamics simulation of the liquid-metal–amorphous-semiconductor transition in germanium. *Physical Review B* **1994,** *49* (20), 14251.

129. Kresse, G.; Joubert, D., From ultrasoft pseudopotentials to the projector augmented-wave method. *Physical Review B* **1999,** *59* (3), 1758.

130. Henkelman, G.; Arnaldsson, A.; Jónsson, H., A fast and robust algorithm for Bader decomposition of charge density. *Computational Materials Science* **2006,** *36* (3), 354-360.

131. Tang, W.; Sanville, E.; Henkelman, G., A grid-based Bader analysis algorithm without lattice bias. *Journal of Physics: Condensed Matter* **2009,** *21* (8), 084204.

132. Materials Studio Modeling Environment 6.0, *Accelrys Software Inc.* **2013**.

133. Brinkmann, G.; Friedrichs, O. D.; Lisken, S.; Peeters, A.; Van Cleemput, N., CaGe—a virtual environment for studying some special classes of plane graphs—an update. *MATCH Communications in Mathematical and in Computer Chemistry* **2010,** *63* (3), 533-552.

134. Reich, S.; Li, L.; Robertson, J., Structure and formation energy of carbon nanotube caps. *Physical Review B* **2005,** *72* (16), 165423.

135. Diarra, M.; Amara, H.; Ducastelle, F.; Bichara, C., Carbon solubility in nickel nanoparticles: A grand canonical Monte Carlo study. P*hysica Status Solidi (b)* **2012,** *249* (12), 2629-2634.

136. Diarra, M.; Zappelli, A.; Amara, H.; Ducastelle, F.; Bichara, C., Importance of carbon solubility and wetting properties of nickel nanoparticles for single wall nanotube growth. *Physical Review Letters* **2012,** *109* (18), 185501.

137. Ding, F.; Bolton, K.; Rosén, A., Iron-carbide cluster thermal dynamics for catalyzed carbon nanotube growth. *Journal of Vacuum Science & Technology A* **2004,** *22* (4), 1471-1476.

138. Ni, L.; Kuroda, K.; Zhou, L.-P.; Ohta, K.; Matsuishi, K.; Nakamura, J., Decomposition of metal carbides as an elementary step of carbon nanotube synthesis. *Carbon* **2009,** *47* (13), 3054-3062.

139. Nagakura, S., Study of metallic carbides by electron diffraction part I. Formation and decomposition of nickel carbide. *Journal of the Physical Society of Japan* **1957,** *12* (5), 482-494.

140. Nagakura, S., Study of metallic carbides by electron diffraction part II. Crystal structure analysis of nickel carbide. *Journal of the Physical Society of Japan* **1958,** *13* (9), 1005-1014.

141. Gómez-Gualdrón, D. A.; Balbuena, P. B., Characterization of carbon atomistic pathways during single-walled carbon nanotube growth on supported metal nanoparticles. *Carbon* **2013,** *57* (0), 298-309.

142. Jiang, A.; Awasthi, N.; Kolmogorov, A. N.; Setyawan, W.; Börjesson, A.; Bolton, K.; Harutyunyan, A. R.; Curtarolo, S., Theoretical study of the thermal behavior of free and alumina-supported Fe-C nanoparticles. *Physical Review B* **2007,** *75* (20), 205426.

143. Moseler, M.; Cervantes-Sodi, F.; Hofmann, S.; Csányi, G.; Ferrari, A. C., Dynamic Catalyst Restructuring during Carbon Nanotube Growth. *ACS Nano* **2010,** *4* (12), 7587-7595.

144. Kokalj, A., Computer graphics and graphical user interfaces as tools in simulations of matter at the atomic scale. *Computational Materials Science* **2003,** *28* (2), 155-168.

145. Gomez-Gualdron, D. A.; Balbuena, P. B., Effect of the metal cluster-cap interaction on the catalyzed growth of single-wall carbon nanotubes. *Journal of Physical Chemistry C* **2009,** *113*, 698-709.

146. Gomez-Gualdron, D. A.; Balbuena, P. B., Growth of chiral single-walled nanotube caps in the presence of a cobalt cluster. *Nanotechnology* **2009,** *20*, 215601.

147. Burgos, J. C.; Jones, E.; Balbuena, P. B., Dynamics of Topological Defects in Single-Walled Carbon Nanotubes during Catalytic Growth. *The Journal of Physical Chemistry C* **2014,** *118* (9), 4808-4817.

148. Martínez de la Hoz, J. M.; Balbuena, P. B., Geometric and electronic confinement effects on catalysis. *The Journal of Physical Chemistry C* **2011,** *115* (43), 21324-21333.

149. Takagi, D.; Homma, Y.; Hibino, H.; Suzuki, S.; Kobayashi, Y., Single-Walled Carbon Nanotube Growth from Highly Activated Metal Nanoparticles. *Nano Letters* **2006,** *6* (12), 2642-2645.

150. Bhaviripudi, S.; Mile, E.; Steiner, S. A.; Zare, A. T.; Dresselhaus, M. S.; Belcher, A. M.; Kong, J., CVD synthesis of single-walled carbon nanotubes from gold nanoparticle catalysts. *Journal of the American Chemical Society* **2007,** *129* (6), 1516-1517.

151. Esconjauregui, S.; Whelan, C. M.; Maex, K., The reasons why metals catalyze the nucleation and growth of carbon nanotubes and other carbon nanomorphologies. *Carbon* **2009,** *47* (3), 659-669.

152. Maruyama, T.; Kondo, H.; Ghosh, R.; Kozawa, A.; Naritsuka, S.; Iizumi, Y.; Okazaki, T.; Iijima, S., Single-walled carbon nanotube synthesis using Pt catalysts under low ethanol pressure *via* cold-wall chemical vapor deposition in high vacuum. *Carbon* **2016,** *96*, 6-13.

153. He, M.; Jiang, H.; Lehtonen, J.; Kauppinen, E. I., Growth of single-walled carbon nanotubes with large chiral angles on rhodium nanoparticles. *Nanoscale* **2013,** *5* (21), 10200-10202.

154. Kozawa, A.; Kiribayashi, H.; Ogawa, S.; Saida, T.; Naritsuka, S.; Maruyama, T., Single-walled carbon nanotube growth on SiO2/Si using Rh catalysts by alcohol gas source chemical vapor deposition. *Diamond and Related Materials* **2016,** *63*, 159-164.

155. Wu, Z.; Chen, Z.; Du, X.; Logan, J. M.; Sippel, J.; Nikolou, M.; Kamaras, K.; Reynolds, J. R.; Tanner, D. B.; Hebard, A. F., Transparent, conductive carbon nanotube films. *Science* **2004,** *305* (5688), 1273-1276.

156. López-Lorente, A.; Simonet, B.; Valcárcel, M., The potential of carbon nanotube membranes for analytical separations. *ACS Publications*: **2010,** 5399-5407.

157. Li, P.; Zhang, X.; Liu, J., Aligned Single-Walled Carbon Nanotube Arrays from Rhodium Catalysts with Unexpected Diameter Uniformity Independent of the Catalyst Size and Growth Temperature. *Chemistry of Materials* **2016,** *28* (3), 870-875.

158. Goldschmidt, H. J., Carbides. *Interstitial Alloys*. *Springer* **1967**, 88-213.

159. Bannikov, V.; Shein, I.; Ivanovskii, A., *Ab initio* predictions of stability and electronic properties of cubic rhodium carbides RhCx as dependent on carbon content. P*hysica Status Solidi (RRL)-Rapid Research Letters* **2009,** *3* (7-8), 218-220.

160. Wang, L.; Ge, Q., Studies of rhodium nanoparticles using the first principles density functional theory calculations. *Chemical Physics Letters* **2002,** *366* (3), 368-376.

161. Wales, D. J.; Doye, J. P., Global optimization by basin-hopping and the lowest energy structures of Lennard-Jones clusters containing up to 110 atoms. *The Journal of Physical Chemistry A* **1997,** *101* (28), 5111-5116.

162. Serp, P.; Hierso, J.-C.; Kalck, P., Surface reactivity of transition metal CVD precursors: towards the control of the nucleation step. *Precursor Chemistry of Advanced Materials*, *Springer* **2005**, 147-171.

163. Fu, Q.; Wagner, T., Interaction of nanostructured metal overlayers with oxide surfaces. *Surface Science Reports* **2007,** *62* (11), 431-498.

164. Sanville, E.; Kenny, S. D.; Smith, R.; Henkelman, G., Improved grid-based algorithm for Bader charge allocation. *Journal of Computational Chemistry* **2007,** *28* (5), 899-908.

165. Materials Studio 8.0. *Accelrys Software Inc.* **2016**.

166. Weller, A. S.; Chadwick, F. M.; McKay, A. I., Chapter Five - Transition Metal Alkane-Sigma Complexes: Synthesis, Characterization, and Reactivity. *Advances in Organometallic Chemistry*, Academic Press: 2016, *66*, 223-276.

167. Kokalj, A., XCrySDen—a new program for displaying crystalline structures and electron densities. *Journal of Molecular Graphics and Modelling* **1999,** *17* (3-4), 176-179.

168. Momma, K.; Izumi, F., VESTA 3 for three-dimensional visualization of crystal, volumetric and morphology data. *Journal of Applied Crystallography* **2011,** *44* (6), 1272-1276.

169. Dong, G.; Frenken, J. W. M., Kinetics of Graphene Formation on Rh(111) Investigated by *In Situ* Scanning Tunneling Microscopy. *ACS Nano* **2013,** *7* (8), 7028-7033.

170. Gibson, K.; Sibener, S., Helium atom scattering from graphene grown on Rh (111). *The Journal of Physical Chemistry C* **2014,** *118* (50), 29077-29083.

171. Gibson, K. D.; Sibener, S. J., Growth, Structure, and Vibrational Properties of Few Layer Graphene Grown on Rh(111). *The Journal of Physical Chemistry C* **2016,** *120* (42), 24158-24164.

172. Dong, G. C.; Baarle, D. W. v.; Rost, M. J.; Frenken, J. W. M., Graphene formation on metal surfaces investigated by *in-situ* scanning tunneling microscopy. *New Journal of Physics* **2012,** *14* (5), 053033.

173. Schmid, G.; Giebel, U.; Huster, W.; Schwenk, A., Large transition metal clusters, 2. Synthesis and properties of Rh55[P(tert-Bu)3]12Cl20. *Inorganica Chimica Acta* **1984,** *85* (1), 97-102.

174. Hoare, M.; Pal, P., Geometry and stability of “spherical” fcc microcrystallites. *Nature* **1972,** *236* (64), 35-37.

175. Rahmani, B.; Balbuena, P. B., Growth of Carbon Nanostructures on Cu Nanocatalyst. *The Journal of Physical Chemistry* **2017,** *(Under Review)*.

176. Tan, H.; Liao, M.; Balasubramanian, K., Electronic states and potential energy surfaces of rhodium carbide (RhC). *Chemical Physics Letters* **1997,** *280* (5–6), 423-429.

177. Gomez-Ballesteros, J. L.; Burgos, J. C.; Lin, P. A.; Sharma, R.; Balbuena, P. B., Nanocatalyst shape and composition during nucleation of single-walled carbon nanotubes. *RSC Advances* **2015,** *5* (129), 106377-106386.

178. Gomez-Ballesteros, J. L.; Balbuena, P. B., Structure and dynamics of metallic and carburized catalytic Ni nanoparticles: effects on growth of single-walled carbon nanotubes. *Physical Chemistry Chemical Physics* **2015,** *17* (22), 15056-15064.

179. Wei, B. Q.; Vajtai, R.; Ajayan, P. M., Reliability and current carrying capacity of carbon nanotubes. *Applied Physics Letters* **2001,** *79* (8), 1172-1174.

180. Durkop, T.; Getty, S. A.; Cobas, E.; Fuhrer, M. S., Extraordinary mobility in semiconducting carbon nanotubes. *Nano Letters* **2004,** *4* (1), 35-39.

181. Moors, M.; Amara, H.; Visart de Bocarmé, T.; Bichara, C.; Ducastelle, F.; Kruse, N.; Charlier, J.-C., Early stages in the nucleation process of carbon nanotubes. *ACS Nano* **2009,** *3* (3), 511-516.

182. Shibuta, Y.; Maruyama, S., Molecular dynamics simulation of formation process of single-walled carbon nanotubes by CCVD method. *Chemical Physics Letters* **2003,** *382* (3), 381-386.

183. Yao, Y.; Dai, X.; Liu, R.; Zhang, J.; Liu, Z., Tuning the diameter of single-walled carbon nanotubes by temperature-mediated chemical vapor deposition. *The Journal of Physical Chemistry C* **2009,** *113* (30), 13051-13059.

184. Arenal, R.; Lothman, P.; Picher, M.; Than, T.; Paillet, M.; Jourdain, V., Direct evidence of atomic structure conservation along ultra-long carbon nanotubes. *The Journal of Physical Chemistry C* **2012,** *116* (26), 14103-14107.

185. Ohta, Y.; Okamoto, Y.; Page, A. J.; Irle, S.; Morokuma, K., Quantum Chemical Molecular Dynamics Simulation of Single-Walled Carbon Nanotube Cap Nucleation on an Iron Particle. *ACS Nano* **2009,** *3* (11), 3413-3420.

186. Elliott, J. A.; Shibuta, Y.; Amara, H.; Bichara, C.; Neyts, E. C., Atomistic modelling of CVD synthesis of carbon nanotubes and graphene. *Nanoscale* **2013,** *5* (15), 6662-6676.

187. Tefera, A. G.; Mochena, M. D., Nucleation and anomalous cap formation on icosahedral Fe-13 nanocatalyst: A first step towards chirality-controlled single-walled nanotube growth. *Carbon* **2014,** *67,* 198-202.

188. Helveg, S., Lopez-Cartes, C., Sehested, J., Hansen, P.L.,Clausen, B.S., Rostrup-Nielsen, J.R., Abild-Pedersen, F., and Norskov J., Atomic-scale imaging of carbon nanofibre growth. *Nature* **2004,** *427*, 426

189. Sharma, R., Zafar, Iqbal *In situ* observations of carbon nanotube formation using environmental electron microscopy (ETEM). *Applied Physics Letters* **2004,** *84*, 990-992.

190. Sharma, R., Moore, E.S., Rez, P, Treacy M.M.J., Site-specific fabrication of Fe particles for carbon nanotube growth. *Nano Letters* **2009,** *9* (2), 689-694.

191. Goyal, A.; Wiegand, D. A.; Owens, F. J.; Iqbal, Z., Synthesis of carbide-free, high strength iron–carbon nanotube composite by *in situ* nanotube growth. *Chemical Physics Letters* **2007,** *442* (4), 365-371.

192. Nagakura, S., Study of metallic carbides by electron diffraction IV. Cobalt carbides. *Journal of the Physical Society of Japan* **1961,** *16,* 1213-1219.

193. Diehm, P. M.; Ágoston, P.; Albe, K., Size-Dependent Lattice Expansion in Nanoparticles: Reality or Anomaly? *ChemPhysChem* **2012,** *13* (10), 2443-2454.

194. Sharma, R., Crozier, Peter A., Environmental Transmission Electron Microscopy in Nanotechnology. *Transmission Electron Microscopy for Nanotechnology, Springer-Verlag and Tsinghua University Press* **2005**, 531-565.

195. Ribas, M. A.; Ding, F.; Balbuena, P. B.; Yakobson, B. I., Nanotube nucleation *versus* carbon-catalyst adhesion--probed by molecular dynamics simulations. *The Journal of Chemical Physics* **2009,** *131* (22), 224501.

196. Zhao, Y.-H.; Su, H.-Y.; Sun, K.; Liu, J.; Li, W.-X., Structural and electronic properties of cobalt carbide Co2C and its surface stability: Density functional theory study. *Surface Science* **2012,** *606* (5–6), 598-604.

197. Yamada, T.; Maigne, A.; Yudasaka, M.; Mizuno, K.; Futaba, D. N.; Yumura, M.; Iijima, S.; Hata, K., Revealing the Secret of Water-Assisted Carbon Nanotube Synthesis by Microscopic Observation of the Interaction of Water on the Catalysts. *Nano Letters* **2008,** *8* (12), 4288-4292.

198. Picher, M.; Anglaret, E.; Arenal, R.; Jourdain, V., Self-deactivation of single-walled carbon nanotube growth studied by *in situ* Raman measurements. *Nano Letters* **2009,** *9* (2), 542-547.

199. Puretzky, A. A.; Geohegan, D. B.; Jesse, S.; Ivanov, I. N.; Eres, G., *In situ* measurements and modeling of carbon nanotube array growth kinetics during chemical vapor deposition. *Applied Physics A* **2005,** *81* (2), 223-240.

200. Tulevski, G. S.; Franklin, A. D.; Frank, D.; Lobez, J. M.; Cao, Q.; Park, H.; Afzali, A.; Han, S.-J.; Hannon, J. B.; Haensch, W., Toward High-Performance Digital Logic Technology with Carbon Nanotubes. *ACS Nano* **2014,** *8* (9), 8730-8745.

201. Cao, Q.; Han, S.-j., Single-walled carbon nanotubes for high-performance electronics. *Nanoscale* **2013,** *5* (19), 8852-8863.

202. Franklin, A. D.; Chen, Z., Length scaling of carbon nanotube transistors. *Nature Nano* **2010,** *5* (12), 858-862.

203. Liu, Z.; Jiao, L.; Yao, Y.; Xian, X.; Zhang, J., Aligned, Ultralong Single-Walled Carbon Nanotubes: From Synthesis, Sorting, to Electronic Devices. *Advanced Materials* **2010,** *22* (21), 2285-2310.

204. Zheng, M.; Jagota, A.; Semke, E. D.; Diner, B. A.; McLean, R. S.; Lustig, S. R.; Richardson, R. E.; Tassi, N. G., DNA-assisted dispersion and separation of carbon nanotubes. *Nature Materials* **2003,** *2* (5), 338-342.

205. Krupke, R.; Hennrich, F.; Löhneysen, H. v.; Kappes, M. M., Separation of Metallic from Semiconducting Single-Walled Carbon Nanotubes. *Science* **2003,** *301* (5631), 344-347.

206. Li, X.; Tu, X.; Zaric, S.; Welsher, K.; Seo, W. S.; Zhao, W.; Dai, H., Selective Synthesis Combined with Chemical Separation of Single-Walled Carbon Nanotubes for Chirality Selection. *Journal of the American Chemical Society* **2007,** *129* (51), 15770-15771.

207. Bonaccorso, F.; Hasan, T.; Tan, P. H.; Sciascia, C.; Privitera, G.; Di Marco, G.; Gucciardi, P. G.; Ferrari, A. C., Density Gradient Ultracentrifugation of Nanotubes: Interplay of Bundling and Surfactants Encapsulation. *The Journal of Physical Chemistry C* **2010,** *114* (41), 17267-17285.

208. Wirth, C. T.; Bayer, B. C.; Gamalski, A. D.; Esconjauregui, S.; Weatherup, R. S.; Ducati, C.; Baehtz, C.; Robertson, J.; Hofmann, S., The Phase of Iron Catalyst Nanoparticles during Carbon Nanotube Growth. *Chemistry of Materials* **2012,** *24* (24), 4633-4640.

209. Gavillet, J.; Loiseau, A.; Journet, C.; Willaime, F.; Ducastelle, F.; Charlier, J.-C., Root-growth mechanism for single-wall carbon nanotubes. *Physical Review Letters* **2001,** *87* (27), 275504.

210. Qi, W., Size effect on melting temperature of nanosolids. *Physica B: Condensed Matter* **2005,** *368* (1), 46-50.

211. Burgos, J. C.; Jones, E.; Balbuena, P. B., Effect of the Metal−Substrate Interaction Strength on the Growth of Single-Walled Carbon Nanotubes. *The Journal of Physical Chemistry C* **2011,** *115* (15), 7668-7675.

212. Rümmeli, M. H.; Schäffel, F.; Kramberger, C.; Gemming, T.; Bachmatiuk, A.; Kalenczuk, R. J.; Rellinghaus, B.; Büchner, B.; Pichler, T., Oxide-Driven Carbon Nanotube Growth in Supported Catalyst CVD. *Journal of the American Chemical Society* **2007,** *129* (51), 15772-15773.

213. Ding, F.; Bolton, K., The importance of supersaturated carbon concentration and its distribution in catalytic particles for single-walled carbon nanotube nucleation. *Nanotechnology* **2006,** *17* (2), 543.

214. Yang, Z.; Wang, Q.; Shan, X.; Yang, S.-W.; Zhu, H., Theoretical investigation on carbon nucleation on nickel carbides at initial stages of single-walled carbon nanotube formation. *Physical Chemistry Chemical Physics* **2014,** *16* (36), 19654-19660.

215. Donald, W. B.; Olga, A. S.; Judith, A. H.; Steven, J. S.; Boris, N.; Susan, B. S., A second-generation reactive empirical bond order (REBO) potential energy expression for hydrocarbons. *Journal of Physics: Condensed Matter* **2002,** *14* (4), 783.

216. Tersoff, J., Modeling solid-state chemistry: Interatomic potentials for multicomponent systems. *Physical Review B* **1989,** *39* (8), 5566-5568.

217. Nayak, S. K.; Khanna, S. N.; Rao, B. K.; Jena, P., Physics of Nickel Clusters:‚Äâ Energetics and Equilibrium Geometries. *The Journal of Physical Chemistry A* **1997,** *101* (6), 1072-1080.

218. Saroj, K. N.; Khanna, S. N.; Rao, B. K.; Jena, P., Thermodynamics of small nickel clusters. *Journal of Physics: Condensed Matter* **1998,** *10* (48), 10853.

219. Huang, S.-P.; Balbuena, P. B., Melting of Bimetallic Cu−Ni Nanoclusters. *The Journal of Physical Chemistry B* **2002,** *106* (29), 7225-7236.

220. Heifets, E.; Zhukovskii, Y. F.; Kotomin, E. A.; Causá, M., The adhesion nature of the Ag/MgO(100) interface: an *ab initio* study. *Chemical Physics Letters* **1998,** *283* (5–6), 395-401.

221. Campbell, C. T.; Starr, D. E., Metal adsorption and adhesion energies on MgO (100). *Journal of the American Chemical Society* **2002,** *124* (31), 9212-9218.

222. Matsunaka, D.; Shibutani, Y., Electronic states and adhesion properties at metal/MgO incoherent interfaces: First-principles calculations. *Physical Review B* **2008,** *77* (16), 165435.

223. Barcaro, G.; Fortunelli, A., The interaction of coinage metal clusters with the MgO (100) surface. *Journal of Chemical Theory and Computation* **2005,** *1* (5), 972-985.

224. Rao, R.; Sharma, R.; Abild-Pedersen, F.; Norskov, J. K.; Harutyunyan, A. R., Insights into carbon nanotube nucleation: Cap formation governed by catalyst interfacial step flow. *Scientific Reports* **2014,** *4*.

225. Benayad, A.; Li, X.-S., Carbon free nickel subsurface layer tessellating graphene on Ni (111) surface. *The Journal of Physical Chemistry C* **2013,** *117* (9), 4727-4733.

226. Baker, H., Introduction to alloy phase diagrams. *Materials Park, OH: ASM International, 1992.*

227. Ducati, C.; Alexandrou, I.; Chhowalla, M.; Robertson, J.; Amaratunga, G. A. J., The role of the catalytic particle in the growth of carbon nanotubes by plasma enhanced chemical vapor deposition. *Journal of Applied Physics* **2004,** *95* (11), 6387-6391.

228. Charlier, J.-C., Iijima, Sumio, Growth Mechanisms of Carbon Nanotubes. *Springer*: Germany, **2001**, 447.

229. Dai, H., Rinzler, A.G., Nikolaev, P. Thessm A., Colbert, D.T., Smalley, R.E., Single-wall nanotubes produced by metal-catalyzed disproportionation of carbon monoxide *Chemical Physics Letters* **1996,** *260*, 471-475.

230. Baker, R. T. K., Chludzinski, Jr., J.J., Dudash N.S., and Simoens A.J., The formation of filamentous carbon from decomposition of acetylene over vanadium and molybdenum. *Carbon* **1983,** *21* 463

231. Wagner, R. S., Ellis, W.C., Vapor-liquid-solid mechanism of single crystal growth. *Applied Physics Letters* **1964,** *4*, 89-90.

232. He, M.; Jiang, H.; Liu, B.; Fedotov, P. V.; Chernov, A. I.; Obraztsova, E. D.; Cavalca, F.; Wagner, J. B.; Hansen, T. W.; Anoshkin, I. V.; Obraztsova, E. A.; Belkin, A. V.; Sairanen, E.; Nasibulin, A. G.; Lehtonen, J.; Kauppinen, E. I., Chiral-selective growth of single-walled carbon nanotubes on lattice-mismatched epitaxial cobalt nanoparticles. *Scientific Reports* **2013,** *3*, 1460.

233. Hofmann, S.; Blume, R.; Wirth, C. T.; Cantoro, M.; Sharma, R.; Ducati, C.; Havecker, M.; Zafeiratos, S.; Schnoerch, P.; Oestereich, A.; Teschner, D.; Albrecht, M.; Knop-Gericke, A.; Schlogl, R.; Robertson, J., State of Transition Metal Catalysts During Carbon Nanotube Growth. *Journal of Physical Chemistry C* **2009,** *113* (5), 1648-1656.

234. Mazzucco, S.; Wang, Y.; Tanase, M.; Picher, M.; Li, K.; Wu, Z. J.; Irle, S.; Sharma, R., Direct evidence of active and inactive phases of Fe catalyst nanoparticles for carbon nanotube formation. *Journal of Catalysis* **2014,** *319*, 54-60.

235. Kohigashi, Y.; Yoshida, H.; Homma, Y.; Takeda, S., Structurally inhomogeneous nanoparticulate catalysts in cobalt-catalyzed carbon nanotube growth. *Applied Physics Letters* **2014,** *105* (7).

236. Yoshida, H., Takeda, Seiji, Uchiyama,Tetsuya, Kohno, Hideo,Homma, Yoshikazu, Atomic-Scale *In-situ* Observation of Carbon Nanotube Growth from Solid State Iron Carbide Nanoparticles. *Nano Letters* **2008,** *9* (11), 3810-3815.

237. Gomez-Gualdron, D. A.; Beetge, J. M.; Burgos, J. C.; Balbuena, P. B., Effects of Precursor Type on the CVD Growth of Single-Walled Carbon Nanotubes. *Journal of Physical Chemistry C* **2013,** *117* (20), 10397-10409.

238. Amara, H.; Roussel, J.-M.; Bichara, C.; Gaspard, J.-P.; Ducastelle, F., Tight-binding potential for atomistic simulations of carbon interacting with transition metals: Application to the Ni-C system. *Physical Review B* **2009,** *79* (1), 014109.

239. Khalilov, U.; Bogaerts, A.; Neyts, E. C., Microscopic mechanisms of vertical graphene and carbon nanotube cap nucleation from hydrocarbon growth precursors. *Nanoscale* **2014,** *6* (15), 9206-9214.

240. Zhang, B.; Cao, B. B.; Chen, C.; Zhang, J.; Duan, H. M., Density-Functional Theory Study on Neutral and Charged MnC2 (M = Fe, Co, Ni, Cu; n=1-5) Clusters. *Journal of Cluster Science* **2013,** *24* (1), 197-207.

241. Khodakov, A. Y., Chu, Wei, Fongarland, Pascal Advances in the Development of Novel Cobalt Fischer-Tropsch Catalysts for Synthesis of Long-Chain Hydrocarbons and Clean Fuels. *Chemical Reviews* **2007,** *107* (5), 1692-1744.

242. Brenner, D. W., Empirical potential for hydrocarbons for use in simulating the chemical vapor deposition of diamond films. *Physical Review B* **1990,** *42* (15), 9458.

243. Hussaini, Zahra ,Lin, Pin Ann,, Zhu, Wenhui Natarajan, Bharath, and Sharma, Renu., *In situ* Automated Image Processing Scheme to Measure Atomic-Scale Structural Fluctuations, *Microscopy & Microanalysis* 2016, Columbus OH, Microscopy Society of America: Columbus OH, **2016**, 718-719.

244. Sharma, R., Rez, Peter, Treacy, M.M.J. and Stuart, Steven J. , *In-situ* observation of the growth mechanisms of carbon nanotubes under diverse reaction conditions. *Journal of Electron Microscopy* **2005,** *54*, 231-237.

245. Sharma, R., Rez, P., and Treacy, M.M.J. , Direct observations of the growth of carbon nanotubes using *in situ* transmission electron microscopy. *e-Journal of Surface Science and Nano Technology* **2006,** *4*, 460-463.

246. Bal, K. M.; Neyts, E. C., Merging Metadynamics into Hyperdynamics: Accelerated Molecular Simulations Reaching Time Scales from Microseconds to Seconds. *Journal of Chemical Theory and Computation* **2015,** *11* (10), 4545-4554.

247. Khalilov, U.; Bogaerts, A.; Neyts, E. C., Atomic scale simulation of carbon nanotube nucleation from hydrocarbon precursors. *Nature Communications* **2015,** *6*.

248. Anton, R., On the reaction kinetics of Ni with amorphous carbon. *Carbon* **2008,** *46* (4), 656-662.

249. Deruijter, W. J.; Sharma, R.; McCartney, M. R.; Smith, D. J., Measurement of Lattice-Fringe Vectors from Digital Hrem Images - Experimental Precision. *Ultramicroscopy* **1995,** *57* (4), 409-422.

250. Picher, M.; Mazzucco, S.; Blankenship, S.; Sharma, R., Vibrational and optical spectroscopies integrated with environmental transmission electron microscopy. *Ultramicroscopy* **2015,** *150*, 10-15.

APPENDIX A

A.1 Pair Radial Distribution Function

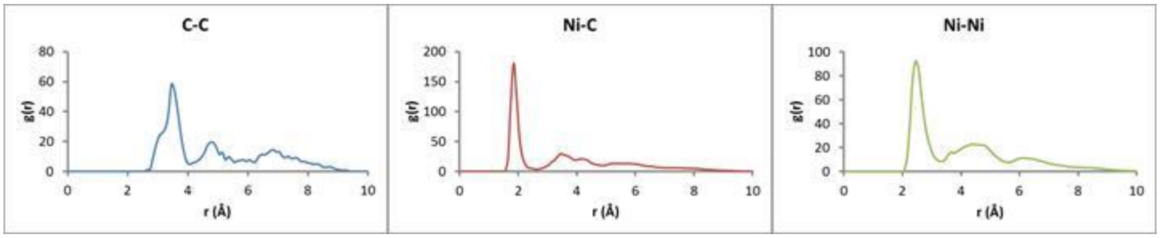

Figure A.1 Pair radial distribution functions (RDF) for C-C (blue), Ni-C(red) and Ni-Ni(green) for atoms in the $Ni_{44}C_{14}$ nanoparticle at 1000 K.

RDF functions help describe the average structure of the system throughout the simulation time. The peaks indicate the most likely location of neighboring atoms of a certain type with respect to a reference atom. Sharp peaks are indicative of a well-defined structure and wider peaks reflect some degree of flexibility of the structure. Both Ni-Ni and Ni-C show a sharp peak located at 2.45 Å and 1.85 Å respectively, showing structural ordering between first nearest-neighbors and a longer range structure that is not very well defined due to fluctuations in the structure at the temperature of the system. A sharp, wider peak is observed for C-C at 3.45 Å as some of the C atoms migrate to the nanoparticle subsurface while maintaining a relative order.

Table A.1 Diffusion coefficient of C atoms in the carburized Ni nanoparticle calculated for two different compositions and temperatures.

Diffusion Coefficients of C Atoms

D(·10^9 m^2/s)	Temperature (K)	
	750	1000
$Ni_{55}C_{10}$	0.098333	0.448333
$Ni_{55}C_{14}$	0.208333	1.698333

The self-diffusion coefficient of C atoms dissolved into the Ni_{55} nanoparticle for two different compositions ($Ni_{55}C_{10}$ and $Ni_{55}C_{14}$) at 750 K and 1000K were obtained by calculating the mean square displacement and applying Einstein's diffusivity equation shown below.

$$D_s = \lim_{t\to\infty} \frac{1}{6t}\left\langle \frac{1}{N}\sum_{j=1}^{N}\left\| r_j(t) - r_j(t_0)\right\|^2 \right\rangle \tag{A.1}$$

The terms in brackets represent the ensemble average of squared displacements of the species of interest, calculated over multiple time origins (t_0) for a time (t) sufficiently long to assume that the system is equilibrated. The calculated self-diffusivities are shown in Table A.1. Higher diffusivities are found at higher temperatures due to the faster dynamics effect on the mobility of C atoms. At higher carbon content, diffusivities are higher as C atoms move faster motivated by a greater overall repulsion inside the nanoparticle due to an increase in the charge magnitudes as mentioned in the charge analysis.

A.2 Energy of Adhesion Nanotube Cap-Nanoparticle

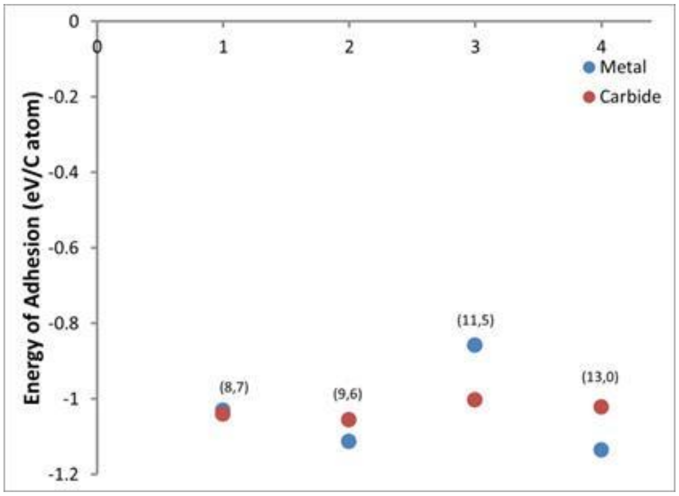

Figure A.2 Energy of adhesion of nanotube caps to pure metal (blue) and carbide (red) nanoparticles.

A.3 Electron Density of States

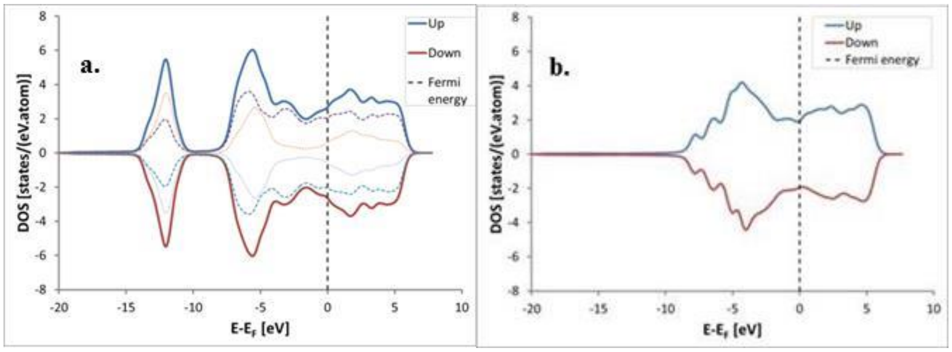

Figure A.3 Electronic density of states for the carburized a. $Ni_{55}C_{14}$ nanoparticle and the metallic b. Ni_{55} nanoparticle. Continuous blue and red lines represents total up and down density of states, dashed purple and light blue lines represent up and down contributions from C atoms, and orange and purple represent contributions from Ni atoms.

The density of states of Ni_{55} exhibits a population of electronic states concentrated in a smaller range of energies than $Ni_{55}C_{14}$, and a lower density of unoccupied states above the Fermi level, which is considered an indicator of a higher reactivity of the latter and supports the reasoning presented in the results and discussion section with respect to electron accumulation and depletion. The density of states shows a continuous population for the metal nanoparticle whereas the presence of a new set of inner orbitals is located below the Fermi level for the carburized nanoparticle as a consequence of adding C atoms into the nanoparticle. Equivalent trends are observed for the other nanotube caps.

APPENDIX B

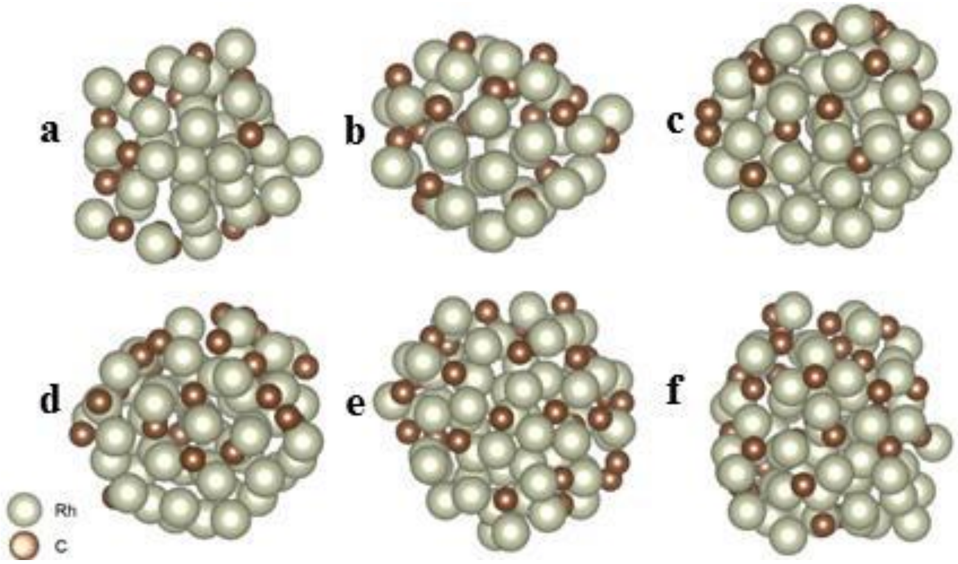

Figure B.1 Carburized unsupported $RhC_{0.5}$ nanoparticles with C added in the subsurface after structural relaxation. (a) $Rh_{38}C_{19}$-O_h1, (b) $Rh_{38}C_{19}$-O_h2, (c) $Rh_{55}C_{28}$-O_h, (d) $Rh_{55}C_{28}$-I_h, (e) $Rh_{68}C_{34}$-$C3_V$, and (f) $Rh_{64}C_{34}$-O_h.

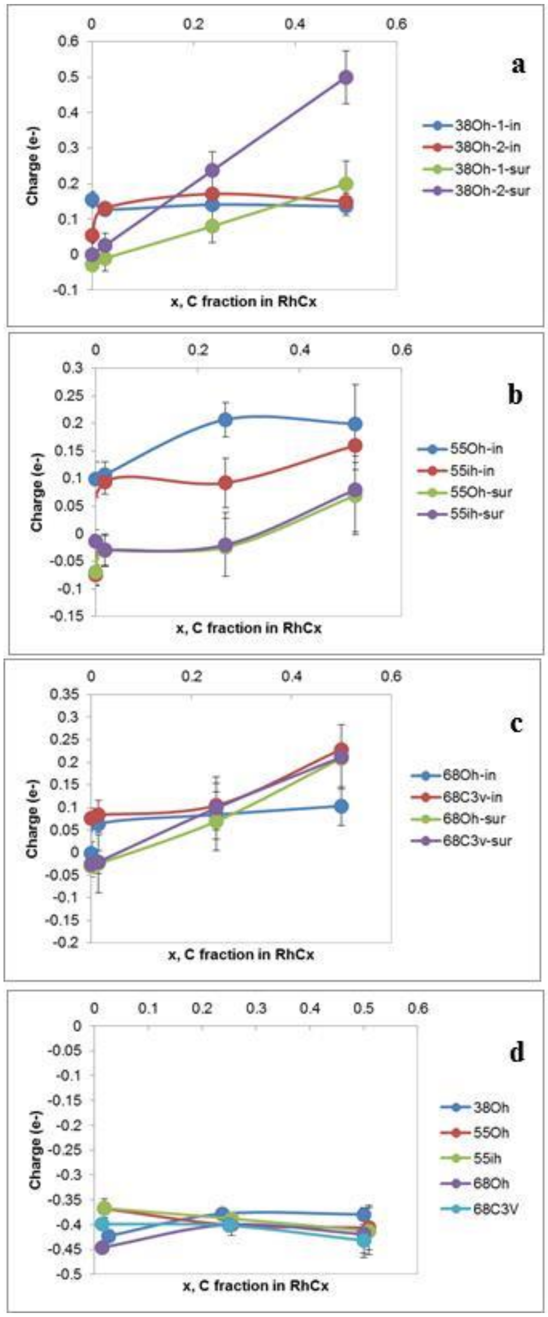

Figure B.2 Average atomic charges of Rh atoms (a-c) and C (d) atoms as a function of carbon content in the nanoparticle. Three particle sizes are considered: (a) 38, (b) 55 and (c) 68 atoms. Distinction between particles with various symmetries (O_h, i_h, and $C3_V$) as well as location of Rh atoms inside the particle (-in) or at the surface (-sur) is made. (d) The atomic charge of carbon is also shown for all the cases studied.

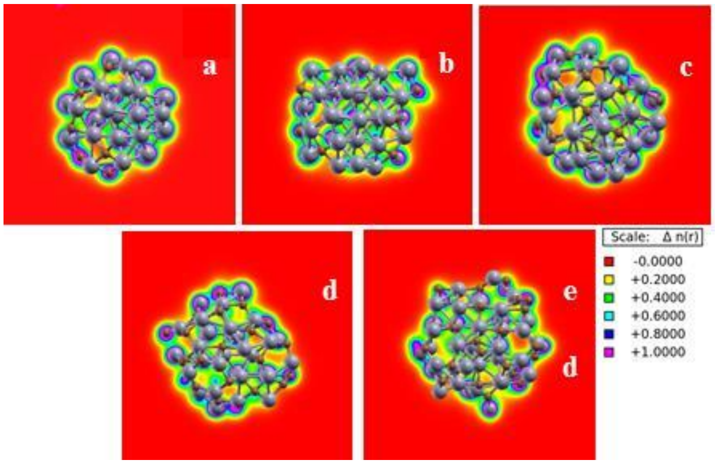

Figure B.3 Electron density maps of unsupported Rh nanoparticles of Rh_2C overall composition and with different sizes and structures: (a) $Rh_{38}C_{19}$-Oh, (b) $Rh_{55}C_{28}$-O_h, (c) $Rh_{55}C_{28}$-I_h, (d) $Rh_{68}C_{34}$-$C3_v$, and (e) $Rh_{68}C_{34}$-O_h. Rh atoms are shown in grey and C atoms are shown in brown.

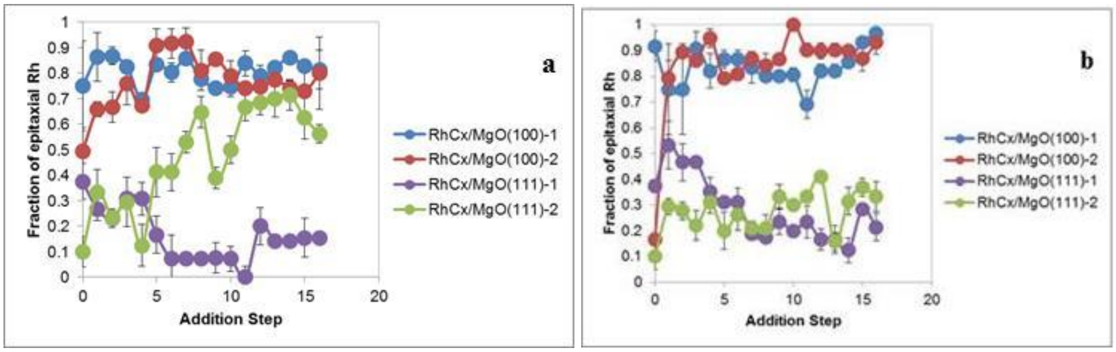

Figure B.4 Fraction of Rh atoms located epitaxially on the MgO substrate interface for supported Rh nanoparticles with C atoms initially placed (a) at the particle surface and (b) in the particle subsurface. Two relative configurations of the nanoparticle with respect to the support with a high (or intermediate) and a low degree of lattice match labeled as '1' and '2', respectively.

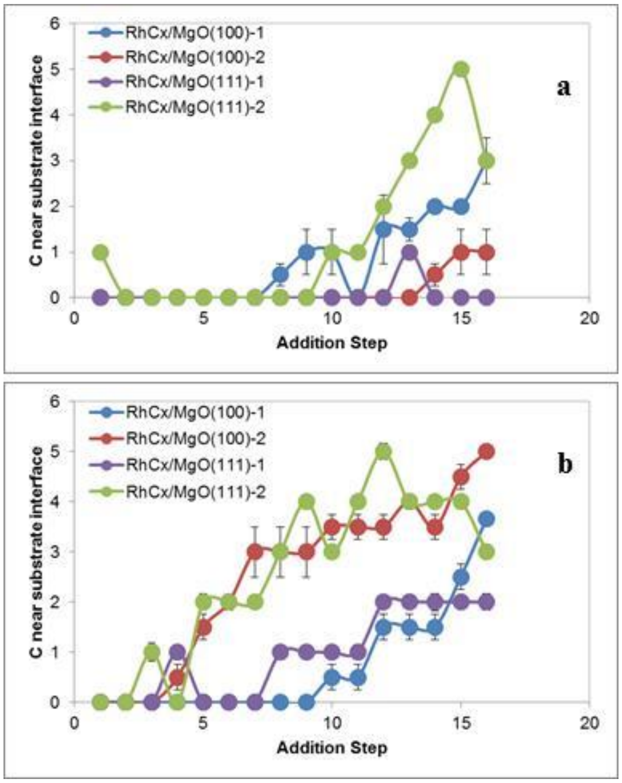

Figure B.5 Number of C atoms located near the particle-substrate interface for supported Rh nanoparticles with C atoms initially placed (a) at the particle surface and (b) in the particle subsurface.

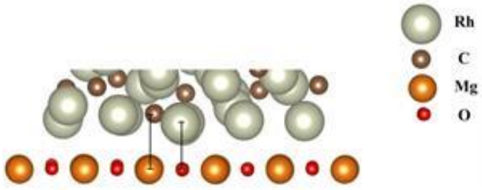

Figure B.6 Illustration of the particle-support interface and the distance measured between them. Distances are reported in Table 4.1.

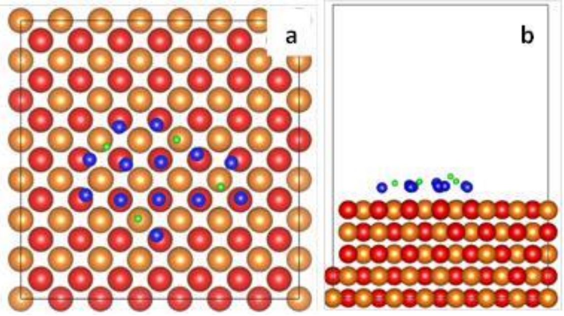

Figure B.7 (a) Top view and (b) side view of the bottom layer of the $Rh_{32}C_{16}$ supported on MgO(100) with epitaxial matching of the Rh atoms located atop O atoms and dissolved C atoms located atop Mg. The color and size of the atoms are changed for emphasis. Mg – orange, O – red, Rh – blue, and C – green.

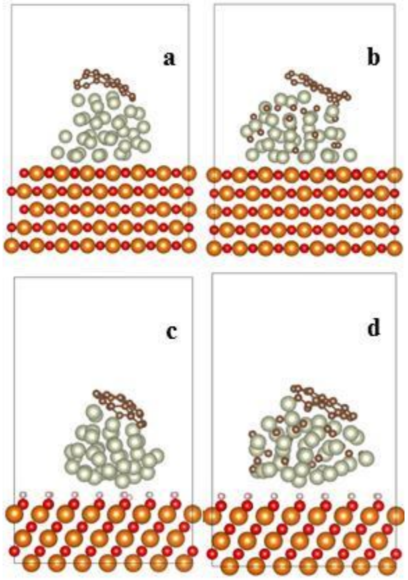

Figure B.8 Supported Rh nanoparticles with a graphene seed adhered on the surface after structural relaxation. (a) Rh/MgO(100) + graphene, (b) Rh_2C/MgO(100) + graphene, (a) Rh/MgO(111) + graphene, and (d) Rh_2C/MgO(111) + graphene.

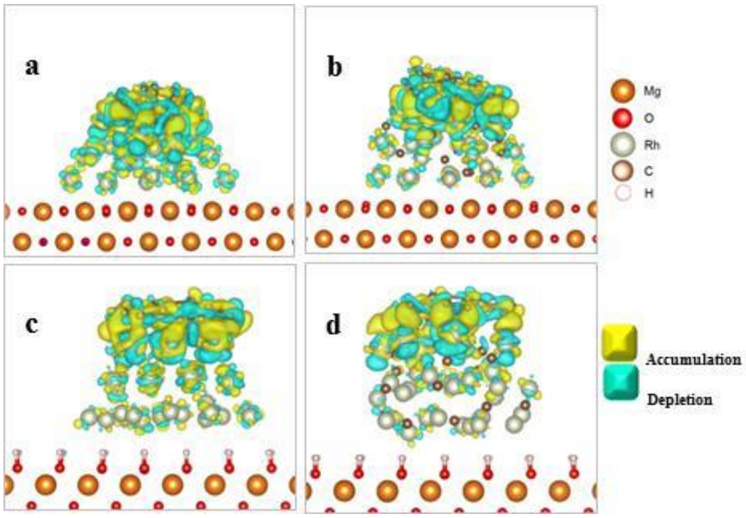

Figure B.9 Regions of electron accumulation and depletion at the particle-graphene interface of (a) Rh/MgO(100), (b) $RhC_{0.5}$/Mg(100), (c) Rh/MgO(111), and (d) $RhC_{0.5}$/MgO(111).

APPENDIX C

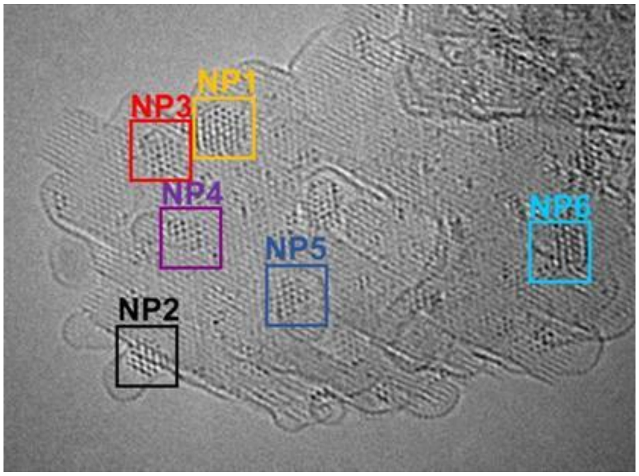

Figure C.1 Structure identification (contd). (D). For the different labelled nanoparticles, the measured d-spacings and angles between crystal planes from the FFT with the values from JCPDS data source can be found in Table C.2.

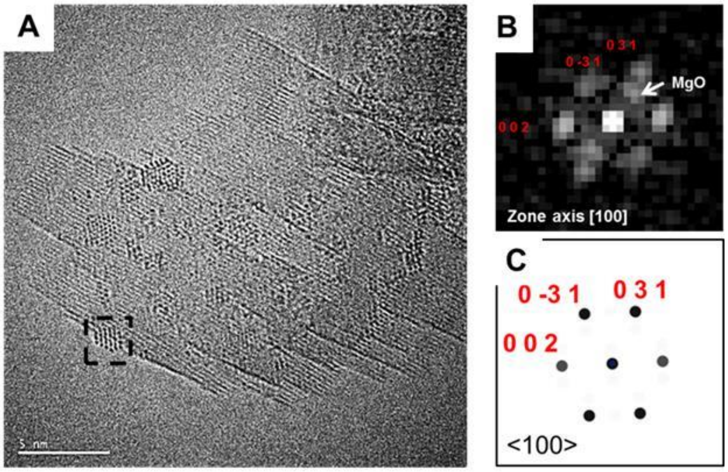

Figure C.2 Structure identification. (A) An image extracted from a digital video recorded with a boxed region containing the particle. Scale bar is 5 nm. (B) The FFT of the box area. Measured d-spacing and angle between (031) and (002) of the nanoparticle matched with Co_3C structure oriented along [100] zone axis. Faint spots from MgO (support) are pointed out by an arrow. (C) Calculated diffraction pattern of Co_3C in [100] zone axis.

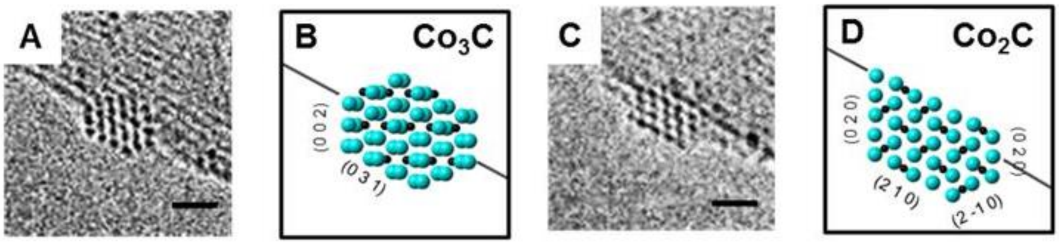

Figure C.3 Crystal structure models (A) High resolution TEM image of Co_3C and corresponding structure model showing the indices of the surface planes (B). (C) High resolution TEM image of Co_2C with corresponding structure model showing the indices of the surface planes (D).

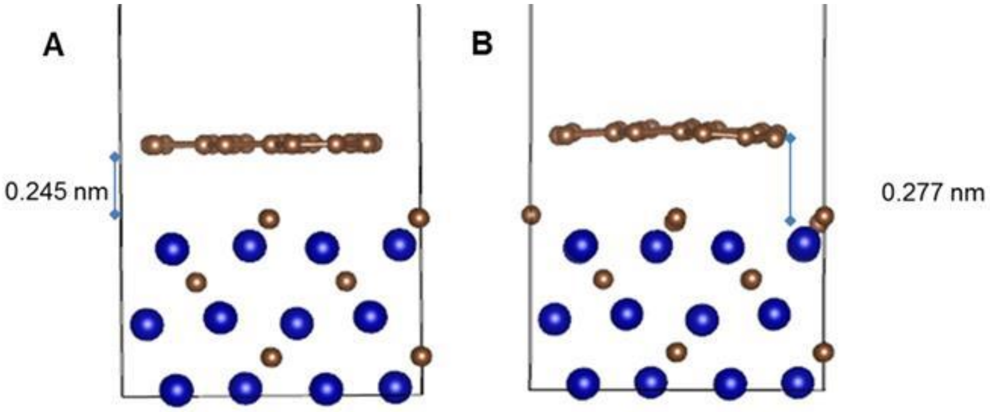

Figure C.4 The distances of graphene to C-terminated Co_2C (020) surface before and after relaxation are 0.245 (A) nm and 0.277 nm (B), respectively.

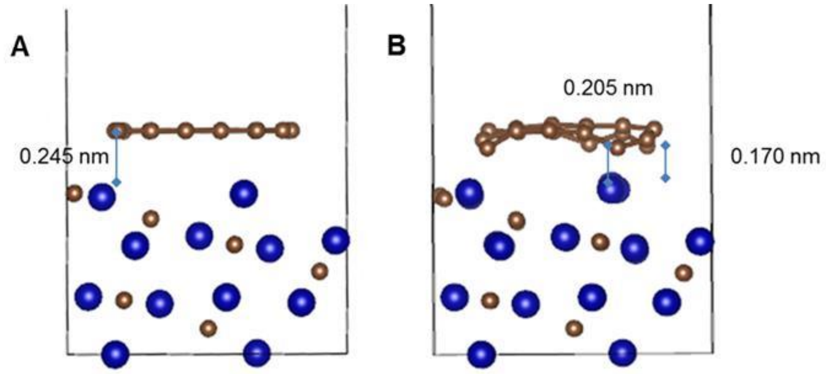

Figure C.5 The distances of graphene and Co-terminated Co_2C (210) surface before and after relaxation are 0.245 nm (A) and 0.170 nm - 0.205 nm (B), respectively.

Table C.1 Comparison of measured d-spacings and angles between crystal planes from the FFT with the values from JCPDS data source (noted as “reference d-spacing” and “reference angles”).

Matching Structure	Measured d-spacing (nm)	Reference d-spacing (nm)	Error* (%)	Miller plane	Angle between planes	Reference Angle (°)	Error (°)	Zone axis
Co_3C	0.191	0.201	-4.88	(0 3 1)	0	0		[100]
	0.231	0.223	2.26	(0 0 2)	125	117	8	
Co_2C	0.212	0.199	6.32	(2 1 0)	0	0		[001]
	0.236	0.221	6.64	(0 2 0)	56.43	63	-6.57	

* All measurements are given as (mean ± one standard deviation), standard deviations are determined from multiple measurements.

Table C.2 Structure determination of different particles during the growth. Comparison of measured d-spacings and angles between crystal planes from the FFT with the values from JCPDS data source (noted as "reference d-spacing" and "reference angles") for the nanoparticles marked P1, P3, P4, P5 and P6 in Figure S2.

NP / Reference	Measured d-spacing (A)	Reference d-spacing (A)	Error* (%)	Miller plane	Angle between planes	Reference Angle (°)	Error (°)	Zone axis
NP1 / Co_2C (no match with Co_3C)	2.355	2.439	-3.4	a: (1 0 1)	a/b 52.44	a/b 56.93	-4.5	[0 1 0]
	2.232	2.235	-0.1	b: (2 0 0)	b/c 56.09	b/c 56.93	-0.9	
	2.402	2.439	-1.5	c: (1 0 -1)	a/c 108.53	a/c 113.86	-5.3	
NP3 / Co_2C (no match with Co_3C)	2.453	2.432	0.9	a: (0 1 1)	a/b 49.23	a/b 56.68	-7.5	[1 0 0]
	2.151	2.213	-2.8	b: (0 2 0)	b/c 58.50	b/c 56.68	1.8	
	2.538	2.432	4.4	c: (0 1 -1)	a/c 107.73	a/c 113.35	-5.6	
NP4 / Co_2C (no match with Co_3C)	2.444	2.439	0.2	a: (1 0 1)	a/b 53.18	a/b 56.93	-3.8	[0 1 0]
	2.229	2.235	-0.2	b: (2 0 0)				
NP5 / Co_2C	2.450	2.432	0.8	a: (0 1 1)	a/b 54.51	a/b 56.68	-2.2	[1 0 0]
	2.256	2.213	1.9	b: (0 2 0)	b/c 54.71	b/c 56.68	-2.0	
	2.374	2.432	-2.4	c: (0 1 -1)	a/c 109.22	a/c 113.35	-4.1	
NP5 / Co_3C	2.450	2.382	2.8	a: (1 -2 1)	a/b 54.51	a/b 58.16	-3.7	[2 1 0]
	2.256	2.258	-0.1	b: (0 0 2)	b/c 54.71	b/c 58.16	-3.5	
	2.374	2.382	-0.3	c: (-1 2 1)	a/c 109.22	a/c 116.33	-7.1	
NP6 / Co_2C	2.354	2.432	-3.2	a: (0 1 1)	a/b 50.78	a/b 56.68	-5.9	[1 0 0]
	2.236	2.213	0.1	b: (0 2 0)				
NP6 / Co_3C	2.354	2.213	6.4	a: (2 0 1)	a/b 50.78	a/b 58.68	-7.9	[0 1 0]
	2.256	2.213	1.0	b: (2 0 -1)				

Table C.3 Results obtained from DFT calculations for the work of adhesion between graphene and Co-terminated (020) and Co-C terminated (210). Four different initial positions of the graphene sheet on the two carbide surface have been tested. Both adhesion processes are favorable, since the combined system (graphene on Co_2C) has lower energy than the individual systems. However, the (020) surface presents a stronger interaction than the (210) surface in all cases. The average work of adhesion values are -26.496 eV nm^{-2} and -14.386 eV nm^{-2} for the (020) and (210) surfaces, respectively.

Energy (eV)	Surface (test 1)		Surface (test 2)		Surface (test 3)		Surface (test 4)	
	(020)	(210)	(020)	(210)	(020)	(210)	(020)	(210)
Co_2C	-359.472	-361.605	-359.472	-361.60	-718.94	-482.15	-718.94	-482.19
graphene	-145.916	-145.916	-145.916	-145.92	-145.92	-145.92	-145.92	-145.92
Combined	-516.268	-512.367	-516.150	-513.90	-876.20	-633.72	-875.04	-634.62
W_{adh} (eV nm^{-2})	-26.737	-11.898	-26.423	-15.65	-27.84	-13.90	-24.99	-16.10

APPENDIX D

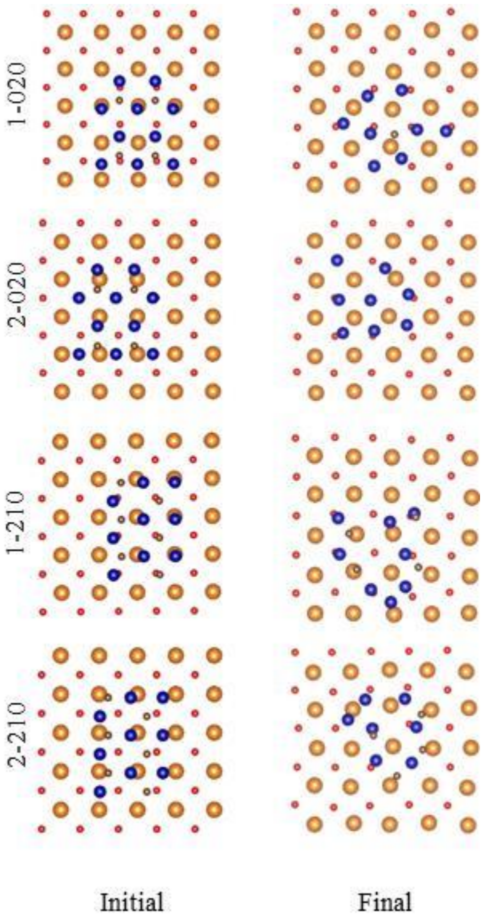

Figure D.1 Top view of the first layer of atoms in Co_2C placed in contact with the MgO substrate in the initial configuration (left) and final configuration after 3 ps of *ab initio* molecular dynamics simulations (right). Each of the surface facets ((020) and (210)) considered for the Co_2C nanoparticle model was initially placed on the MgO surface to either maximize (cases labelled as 1-020 and 1-210) or minimize (cases labelled as 2-020 and 2-210) the number of Co atoms directly on top of Mg atoms. Co atoms in final configuration prefer to be located atop O atoms.

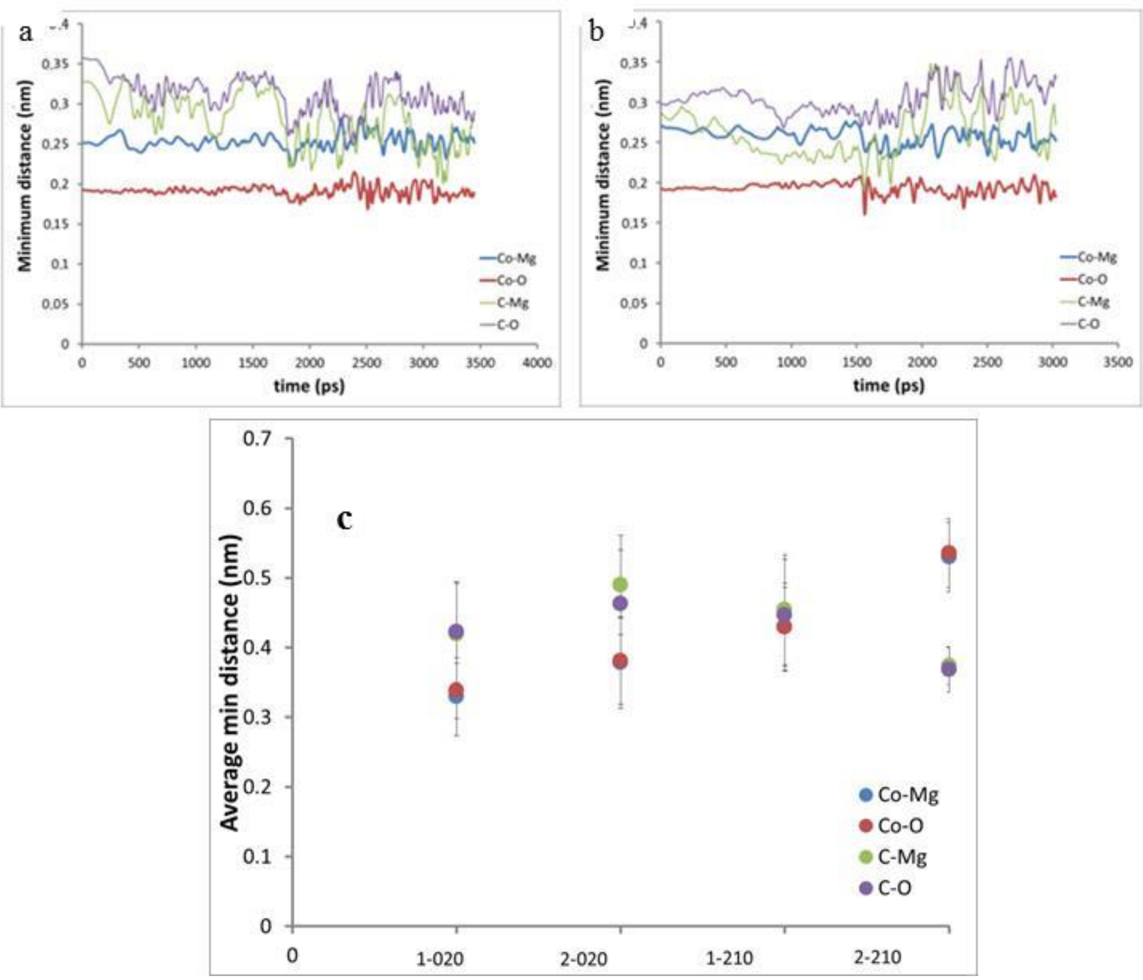

Figure D.2 Minimum distances between atom pairs in the nanoparticle and substrate (Co-Mg, Co-O, C-Mg and C-O). Two cases are shown for illustration: a. 1-020 and b. 1-210. The average closest distance between atom pairs is shown in numeral c. A greater separation between the Co and C distances relative to the substrate in a. compared to b. reflects features of the initial configuration with the nanoparticle bottom layer containing Co atoms only in the former case and both Co and C atoms present in the bottom layer of the latter. The preference of Co atoms to remain closer to O atoms is estimated from the average minimum distance between atom pairs shown in numeral c. C-Mg and Co-Mg minimum distances are almost identical and C-O distances are slightly bigger and uniform across configurations, however C atoms relative arrangement seem not to be influenced by the substrate. Thus, inference about the evolution of the composition of the nanoparticle layer in contact with the substrate indicates that almost only Co atoms atop O atoms tend to be located at the interface and subsequent layers contain both C and Co atoms (Figure D.1).

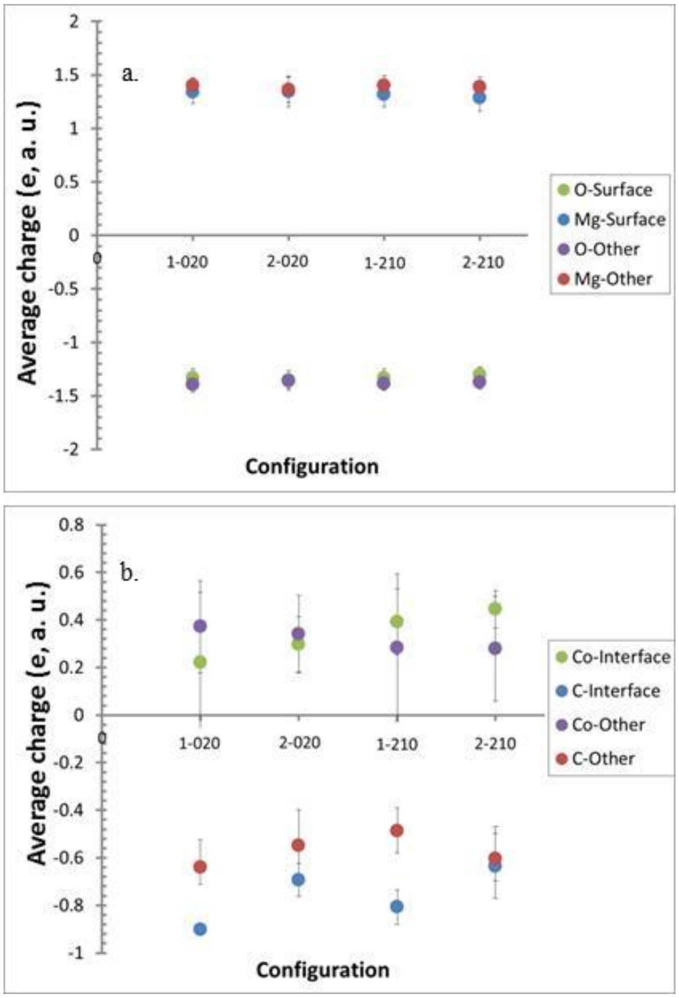

Figure D.3 Average atomic charges calculated using the Bader analysis of charges. Atomic charges for the substrate atoms are shown in the top panel and nanoparticle atoms in the bottom panel. A distinction between atoms located near the interface and those located elsewhere is made. Charge magnitudes of Mg and O are symmetrical and uniform across model systems. No significant difference is found between surface and inner-layer atoms in the substrate. C atoms located closer to the interface tend to be slightly more polarized than Co atoms and other C atoms in all cases; on the other hand interfacial Co atoms are more weakly charged than other Co atoms for the (020) cases, whereas the opposite is observed for the (210) cases.

APPENDIX E

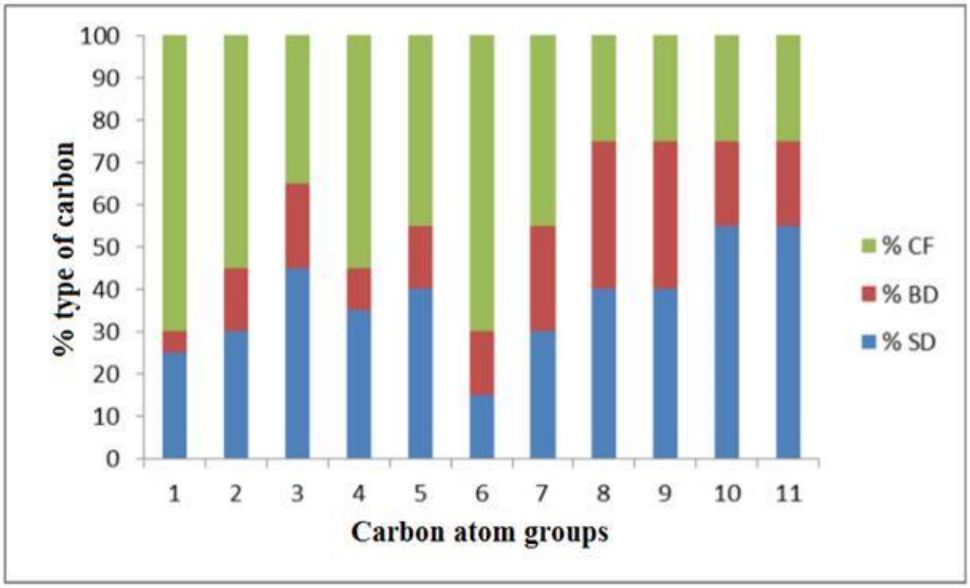

Figure E.1 Percentage of carbon atoms participating in surface diffusion (SD), bulk diffusion (BD) and potential carbide formation (CF) during simulated growth of SWCNTs. Carbon atoms are grouped in sets of 20 atoms in the sequential order that they were catalyzed. Thus each bar represents the percentage of carbon atoms out of 20 classified into one of the three categories.

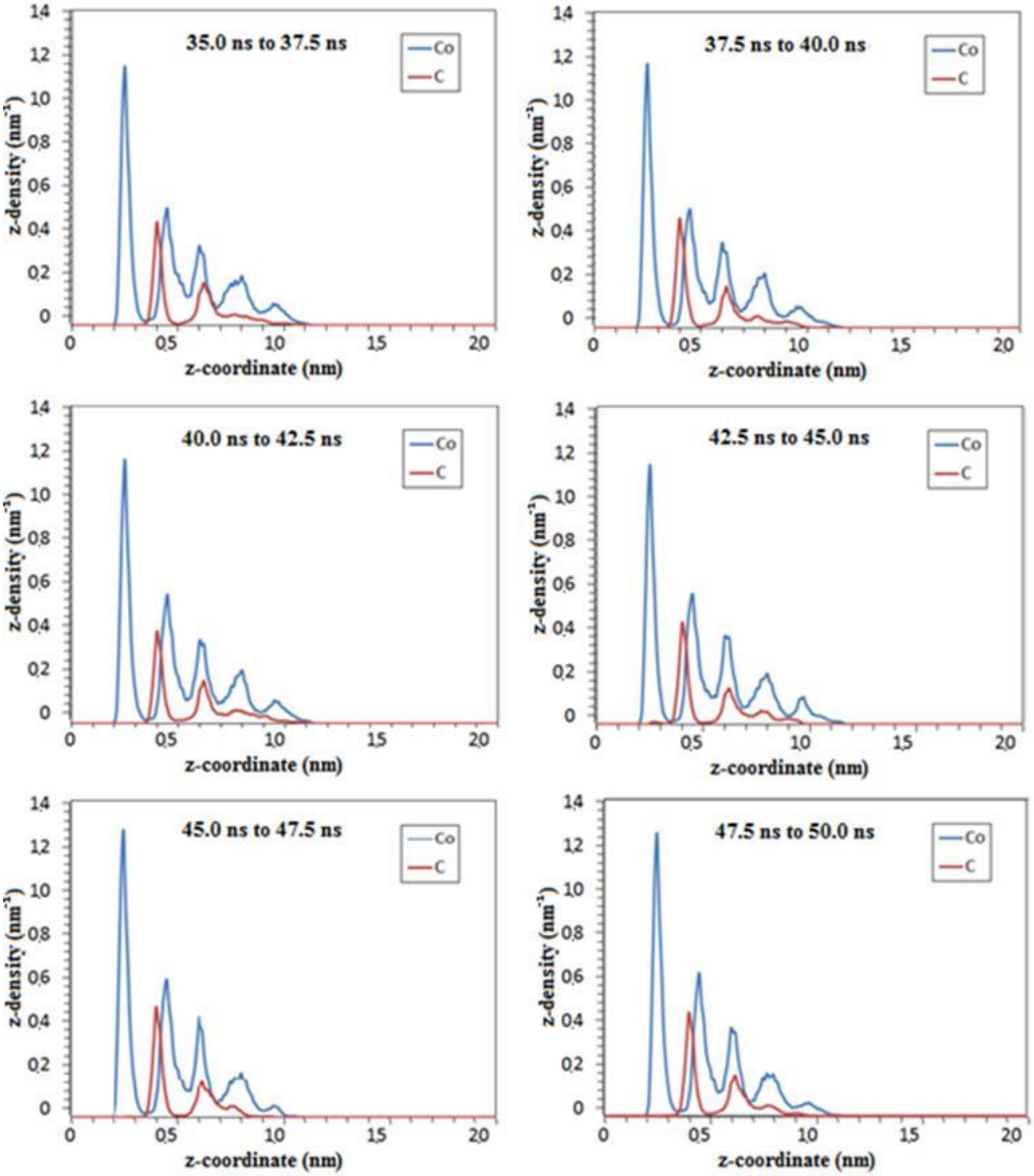

Figure E.2 Z-density profiles for cobalt and carbon atoms at different time intervals during the growth stage. Each peak indicates the relative amount of cobalt and carbon located at a certain layer of the particle. These values are used to estimate the composition ratios shown in Figure 7.3b. Note that similar analysis of the composition profiles was reported in our earlier study;[177] however, such profiles corresponded to the nucleation stage (*i.e.* much shorter times where the profiles were just equilibrating.)

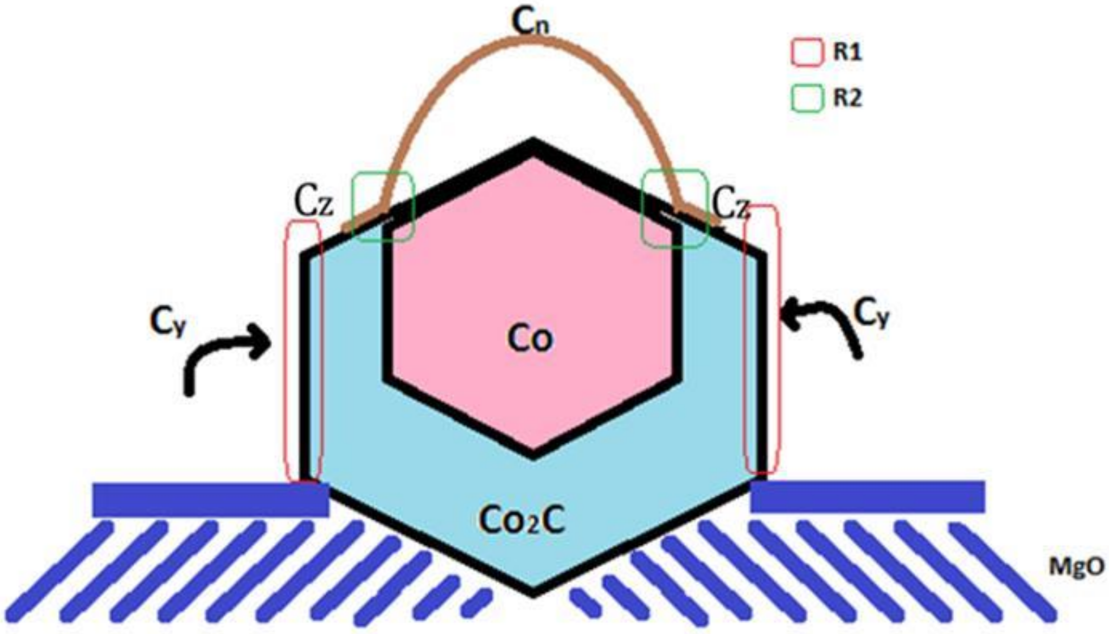

Figure E.3 Schematic illustrating the mechanisms proposed for SWCNT growth for the dynamic formation and decomposition of carbide in the catalyst particle. The dark blue lines represent the MgO support. The carbide phase (light blue) and metallic phase (pink) make up the catalytic particle in contact with the carbon precursor gas, which dissolves into the particle (C_y) at a certain rate (r_1) and can contribute to the formation of the carbide phase and later diffuses out of the particle (C_z) at a rate that varies greatly with time (r_2) to become part of the nanotube (C_n).

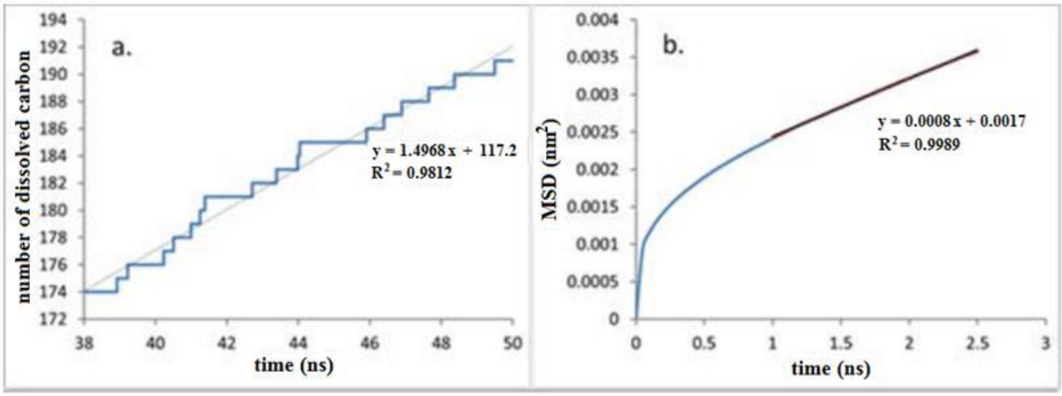

Figure E.4 Data used to estimate the growth rate from RMD simulations. a. The carbon dissolution rate is obtained from the slope of the line fitted to the curve representing the number of carbon atoms dissolved vs time. b. The self-diffusion coefficient of carbon in the particle is estimated using Einstein's method by obtaining the slope of the linear portion of the MSD vs t curve and dividing it by 6.

E.1 Einstein's Equation

$$D_s = \lim_{t\to\infty} \frac{1}{6t}\left\langle \frac{1}{N}\sum_{j=1}^{N}\left\| r_j(t)-r_j(t_0)\right\|^2 \right\rangle \tag{E.1}$$

The ensemble average represented by angular brackets < >, is calculated over multiple time origins (t0) in the trajectory (eq E.1). The number of C atoms considered for diffusion is N, their respective positions at a given time (t) are given by rj. The time length of the trajectories used to estimate D is 15 ns (35ps to 50 ps).

E.2 Structure Determination

Figure E.5a and E.5b show a section of the image extracted from the video containing a catalyst nanoparticle and MgO support, and its fast Fourier transforms (FFT), respectively. The phases present were identified by measuring d-spacing and angles from the fast FFT, where unique reflection from MgO, Co_2C and Co are enclosed by red, blue and green circles, respectively. Other four diffused broad spots can be indexed using either of these phases as respective d-spacing are too close to be resolved (Table E.1). For example, 0.243 nm d-spacing is common for Co_2C [248] and MgO (111) structures. Similarly, 0.2046 nm ($Co_{(111)}$) and 0.1995 nm ($Co_2C_{(210)}$) are too close to be distinguished. Therefore, we use FTT from individual regions marked R1, R2 in Figure 7.1 (main text, entire particle and MgO (support) as described previously).[249-250] Similarly, single d spacing can match with multiple possible phases as reported earlier. Therefore, we first measure and match d-spacing for two reflections and the angle between them with possible structures (Table E.1). Unique identification is confirmed by making sure that indices identified in the first step have a common zone axis (Table E.1). In other words, we use 3-D identification to unambiguously identify the structures in the R1 and R2 regions to be Co and Co_2C respectively. These measurements were used as guidelines for automated image analysis to follow the structural fluctuations in the particle.

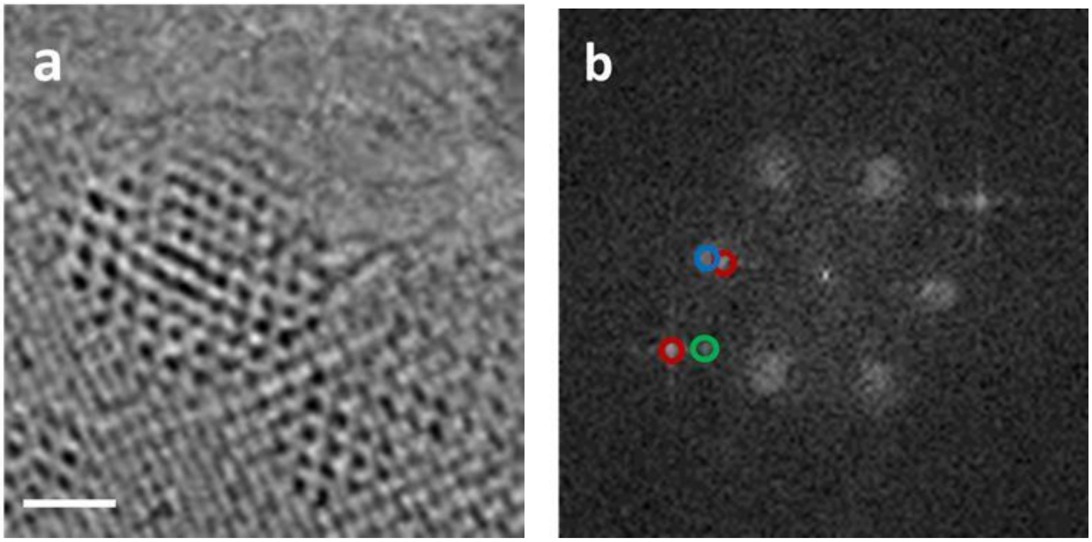

Figure E.5 (a) Part of the high resolution image extracted from a recorded video containing nanoparticle active for SWCNT growth and corresponding FFT. Red, blue and green circles enclose unique reflection from MgO, Co_2C and Co, respectively. Symmetry related reflection to circled spots are not circled for clarity. Other spots are too broad and diffuse to distinguish between the three structures. Scale bar is 1 nm.

Table E.1 Measured d-spacing compared with known values for Co, Co_2C and MgO showing that the reflections present in the FFT (Figure 7.5b) can be indexed using these phases. Note that phase assignment is based on matching d-spacings two or more with common zone axes and the angle (3 D structure).

Structure	Measured d (nm)	Ref (XRD) values d (nm)	(hkl)	Deviation (%)	Angle (°)	Deviation from Ref (°)	Zone Axis
	0.196	0.2046	(1-11)	4.2			
Co	0.195	0.2046	(11-1)	4.69	70	0.05	<011>
	0.182	0.177	(200)	2.82	55	-0.03	
	0.23	0.243	(-101)	5.35			
Co_2C	0.2276	0.214	(1-11)	-5.61	75	-5.7	<121>
	0.212	0.1995	(-210)	-6.27	52	-8.8	
	0.23	2.43	(1-11)	5.35			
MgO	0.227	2.43	(11-1)	7.0	75	-4.5	<011>
	0.212	0.21	(200)	0.95	52	-2.8	

E.3 Composition Calculation

E.3.1 Carbon to Co Ratio (C/Co) in a Single Atomic Layer

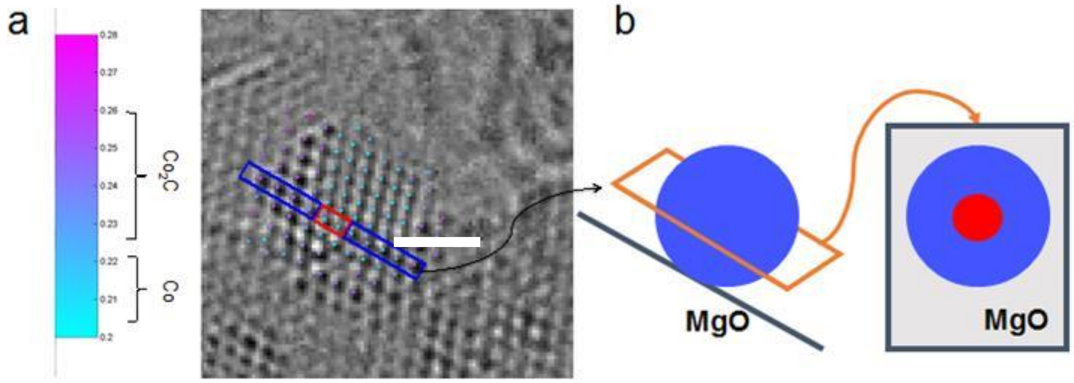

Figure E.6 (a) A single high resolution frame after applying IPS showing the location of atomic columns, where inter-atomic column distances ranging 0.20 nm to 0.22 nm or 0.23 nm to 0.26 nm correspond to Co or Co_2C, respectively. In a single layer, Co and Co_2C columns are marked by red and blue brackets, respectively. (b) Assuming the catalyst particle is a sphere, individual atomic layers as viewed direction perpendicular to the atomic layer will appear as concentric circles representing that the pure Co is sitting inside Co_2C.

Each atomic column in the catalyst particle was assigned as Co or Co_2C (Figure E.6a) depending upon the measured distances from next three nearest neighbors. In each atomic layer, if there are Co atomic columns, those atomic columns only present in the center region (red bracket, Figure E.6a), while Co_2C atomic columns present on both sides (blue brackets, Figure E.6a). By assuming the particle is a sphere, each atomic layer is an intersection of the sphere. Viewing perpendicular to the atomic layer, the two structures can be represented as two concentric circles (Figure E.6b), from where the size of the Co_2C and Co areas can be calculated. For Co_2C area, dividing each plane area by Co_2C unit cell (0.29 nm x 0.44 nm) gives number of Co and C atoms (2 Co and 1 C in the plane area of a Co_2C unit cell). For Co area, dividing by the plane area of a Co unit cell (0.22 nm x 0.22 nm) gives number of Co atoms (1 Co in the plane area of Co unit cell). Thus in each atomic layer, the C/Co ratio is the number of carbon atoms in carbide region and total number of Co atoms from both Co and Co_2C regions.

E.3.2 Carbon Amount in Each Frame in an Individual Particle

By assigning each atomic column in the catalyst particle as Co or Co_2C, fraction of pure Co area (A_{Co}) can be obtained (eq E.2) . Assuming the particle as a sphere, A_{Co} can then be converted into volume fraction (F_{Co}) using the following equation (eq E.3), and plotted as a function of time (Figure E.6):

$$A_{Co} = \frac{\pi r_{Co}^2}{\pi R^2} = \left(\frac{r_{Co}}{R}\right)^2 \qquad \text{(E.2)}$$

$$F_{Co} = \frac{\frac{4}{3}\pi r_{Co}^3}{\frac{4}{3}\pi R^3} = \left(\frac{r_{Co}}{R}\right)^3 = A_{Co}^{1.5} \qquad \text{(E.3)}$$

where r_{Co} is the radius of pure Co region, and R is the radius of the entire particle. Since only the Co_2C region contains carbon atoms, the carbon number ($C_p(t)$) in each frame can be calculated by the following equations (eqs E.4 and E.5) :

$$V_{Co_2C} = F_{Co_2C} \times \frac{4}{3}\pi R^3 = (1 - F_{CO}) \times \frac{4}{3}\pi R^3 \qquad \text{(E.4)}$$

$$C_p(t) = 2\frac{V_{CO_2C}}{0.056} \qquad \text{(E.5)}$$

where V_{Co_2C} is the volume of Co_2C region, F_{Co_2C} is the volume fraction of Co_2C region, R is the particle radius which is measured as 1.25 nm, $C_p(t)$ is the carbon number in the particle carbide region. Note that there are 2 carbon atoms per Co_2C unit cell (0.056 nm^3).

E.3.3 Carbon Amount of SWCNT Growth Section (C_{cnt})

The arc length of the (*a*) of the SWCNT profile in each TEM projection frame is measured manually (Figure E.7). The uncertainty in a is found to be 0.202 nm from multiple tube profile measurements from a single frame and then repeating the same over multiple frames. The surface area of the SWCNT (A_{cnt}) in each frame is estimated from the arc length as (eq E.6):

$$A_{cnt} = \pi d h + \frac{\pi}{2} d^2 \qquad \text{(E.6)}$$

Where $h = \frac{a}{2} - \frac{\pi d}{4}$ and d is the SWCNT diameter (which is measured as 1.78 nm).

$$C_{cnt} = A_{cnt} \times D_{graphene} \qquad \text{(E.7)}$$

where $D_{graphene}$ is the carbon areal density in a graphene sheet (38 carbon nm^{-2}).

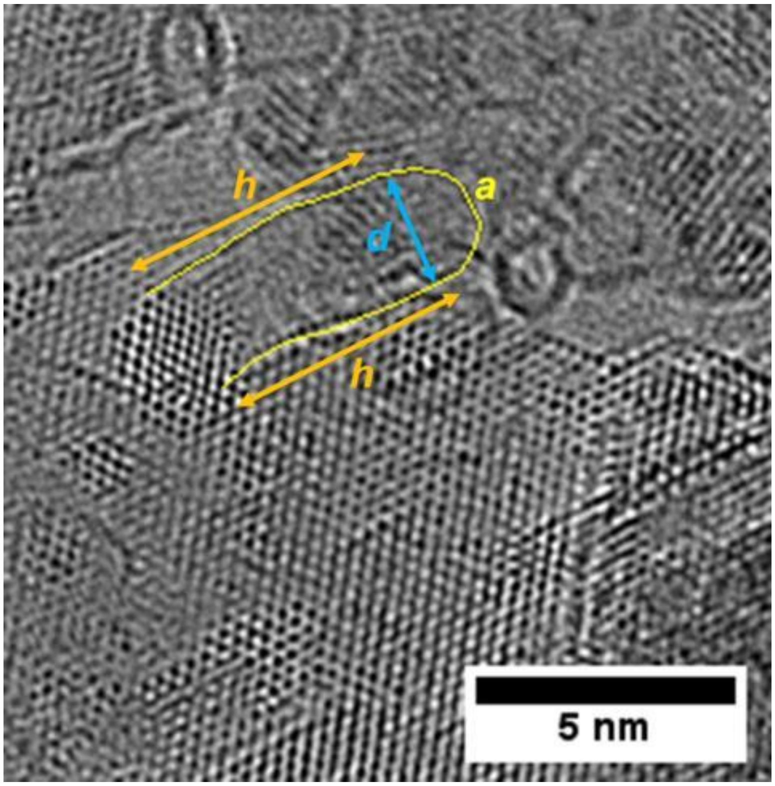

Figure E.7 A single high resolution frame of CNT growth illustrating measurement of arc length CNT profile (*a*) and diameter (*d* = 1.78 nm), which are used to calculate the height (h), the surface area (A_{cnt}) and the number of carbon atoms in the SWCNT (C_{cnt}) (eq E.7).

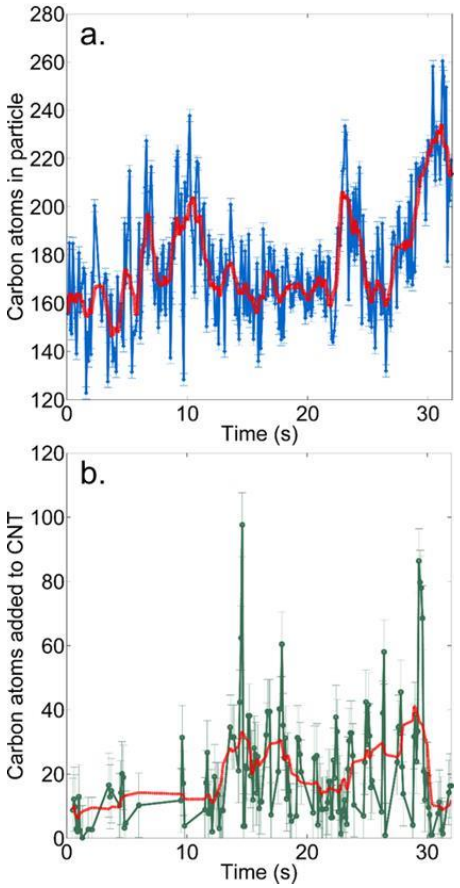

Figure E.8 (a) Number of carbon atoms in the catalyst particle $C_p(t)$; and (b) the number of carbon atoms added to growing nanotube plotted as a function of time. Uncertainties in $C_p(t)$ are derived by propagating the uncertainty in atomic position identification (0.015 nm) through equations shown above. Uncertainties in number of carbon atoms added to the CNT are derived by propagating the human error in CNT length measurement (0.202 nm) through equations shown above. A moving average of 10 frames is applied to smooth the data and is shown as the red curve in these plots. While an opposite trend of fluctuations in the amount of carbon inside the particle and used for SWCNT growth is visually observable, further statistical analysis reveals only a moderate inverse linear correlation for the data sets smoothed using a 10 point moving average scheme (correlation coefficient: -0.18). We attribute this moderate correlation coefficient to the inherently noisy nature of this data, due to various other stochastic processes, such as precursor decomposition, also occurring that effect both the carbide formation and nanotube growth. In the simulated data too, the tube growth rate fluctuations that are out of phase with the time evolution of the carbon content in the particle (Figure 3c-e). However, the calculated correlation coefficient is -0.92, which is higher than the experimental value of -0.18 as expected.

Table E.2 Measured number of carbon atoms added to the nanotube and the number atoms ejected from the decomposed carbide for 5 s time intervals shown below**.**

Time period of SWCNT growth	**11.0 s to 16.0 s**	**16.0 s to 21.0 s**	**21.0 s to 26.0 s**	**26.0 s to 31.0 s**
Carbon atoms added to SWCNT	**789**	**724**	**657**	**834**
Carbon output from decomposed carbide	**451**	**285**	**439**	**357**

E.3.4 Relationship Between Carbide Formation Rate and Carbon Dissolution Rate

Our experimental results indicate the nature of this relationship based on the following facts:

1. Two distinct regions are identified: (i) a carbide region and (ii) a pure metal region.
2. Changes in the size of the carbide region give an idea of how much carbide is forming and decomposing.
3. Any carbon atom dissolving in the particle is perceived in the experiments as an increase in the size of the carbide region (*i.e.* formation of carbide). In other words, C atoms which dissolve in the catalyst contribute to increasing the carbide region.